THE CATHOLIC UNIVERSITY OF AMERICA

Modeling High-Resolution Spectra from X-ray Illuminated Accretion Disks

A DISSERTATION

Submitted to Faculty of the

Department of Physics

School of Arts and Sciences

Of The Catholic University of America

In Partial Fulfillment of the Requirements

For the Degree

Doctor of Philosophy

By

Javier Adolfo García

Washington, D.C.

2010

Modeling High-Resolution Spectra from X-ray Illuminated Accretion Disks

Javier Adolfo García, Ph.D.

Director: Steven B. Kraemer, Ph.D.

This work focuses on the study of X-ray illuminated accretion disks around black holes by modeling their structure and reprocessed emission. The calculation of new models for the reflected spectra consider the effects of incident X-rays on the surface of an accretion disk by solving simultaneously the equations of radiative transfer, energy balance and ionization equilibrium over a large range of column densities. Plane-parallel geometry and azimuthal symmetry are assumed, such that each calculation corresponds to a ring at a given distance from the central object. The radiation transfer equations are solved by using the Feautrier scheme. Ionization and thermal balance are solved by using the photoionization code XSTAR, including the most recent and complete atomic data for K-shell of the isonuclear sequences of iron, oxygen, and nitrogen. The redistribution of photons due to Compton scattering is included using a Gaussian approximation for the Compton kernel. The atomic data for nitrogen ions, namely, level energies, wavelengths, gf-values, radiative widths, total and partial Auger widths, and total and partial photoionization cross sections are computed with a portfolio of publicly available atomic physics codes: AUTOSTRUCTURE, HFR, and BPRM.

The shape of the Fe K-line is perhaps one of the most important features in the X-ray spectrum of accreting sources. Therefore, the effect of fluorescent Kα line emission and absorption in the emitted spectrum is explored, as well as the dependence of the

spectrum on the strength of the incident X-rays and other input parameters and the importance of Comptonization on the emitted spectrum. These calculations predict under which conditions the line is formed, providing information about the ionization stage of the emitting gas. The width of this line is often related to relativistic effects (i.e. gravitational redshift), since the emitting gas may be located in regions close to the black hole. However, these models suggest that the energy redistribution of the photons due to Compton scattering also affects the line profile and it is responsible for an important fraction of the broadening.

This dissertation by Javier Adolfo García fulfills the dissertation requirement for the doctoral degree in Physics approved by Steven B. Kraemer, Ph.D., as Director and by Timothy R. Kallman, Ph.D., and Frederick C. Bruhweiler, Ph.D. as Readers.

Steven B. Kraemer, Ph.D., Director

Timothy R. Kallman, Ph.D., Reader

Frederick C. Bruhweiler, Ph.D., Reader

To the memory of my grandfather,

Don José García Diez

Contents

List of Figures vi

List of Tables ix

Acknowledgements x

1 Introduction 1
- 1.1 Historical Background . . . 1
- 1.2 Compact Objects and Accreting Sources . . . 3
- 1.3 Early X-ray observations . . . 6
- 1.4 X-ray reflected spectra . . . 8
- 1.5 This Dissertation . . . 11

2 Theory of Accretion and Radiative Transfer 14
- 2.1 Accretion onto Black Holes . . . 14
  - 2.1.1 Sakura & Sunyaev standard model . . . 16
- 2.2 Comptonization of X-rays by cold electrons . . . 18
  - 2.2.1 Green's function method . . . 18
  - 2.2.2 Gaussian approximation . . . 20
- 2.3 Radiative Transfer . . . 24
  - 2.3.1 The interaction of radiation with matter . . . 24
  - 2.3.2 Derivation of the Transfer Equation . . . 26
  - 2.3.3 Optical Depth and the Source function . . . 28
  - 2.3.4 Moments of Transfer equation . . . 29
  - 2.3.5 Formal solution in plane parallel geometry . . . 30
  - 2.3.6 Limitng expressions for the Source function . . . 30
  - 2.3.7 Two-point boundary value problem . . . 33
  - 2.3.8 Eddington factors approach . . . 37
  - 2.3.9 The Chandrasekhar solution . . . 43
- 2.4 Summary . . . 53

3 X-ray reflected spectra from accretion disk models 55
- 3.1 Introduction . . . 55
- 3.2 Methodology . . . 58
  - 3.2.1 Radiative Transfer . . . 58
  - 3.2.2 Structure of the gas . . . 62
  - 3.2.3 Radiative equilibrium . . . 63
  - 3.2.4 Atomic data . . . 65
  - 3.2.5 Iteration procedure . . . 66

3.3 Results . . . 67
3.3.1 Temperature profiles . . . 68
3.3.2 Reflected spectra . . . 72
3.3.3 Spectral features . . . 75
3.3.4 Anisotropy: incident and viewing angles . . . 81
3.3.5 Iron abundance . . . 85
3.3.6 Comparison with previous models . . . 87
3.4 Conclusions . . . 90

4 Theory of The Atomic Structure **92**
4.1 Introduction . . . 92
4.2 AUTOSTRUCTURE . . . 93
4.2.1 Energy Levels . . . 94
4.2.2 Variational Principle in the Calculation of Energy Levels . . . 96
4.2.3 Relativistic Corrections to the Hamiltonian . . . 97
4.2.4 Photoionization Cross Sections . . . 100
4.3 X-ray Fluorescence lines . . . 100

5 Nitrogen K-shell photoabsorption **104**
5.1 Introduction . . . 104
5.2 Numerical methods . . . 106
5.3 Results . . . 109
5.3.1 Energy levels . . . 109
5.3.2 Wavelengths . . . 116
5.3.3 *A*-coefficients . . . 117
5.3.4 Radiative widths . . . 120
5.3.5 Auger widths . . . 122
5.3.6 Photoabsorption cross sections . . . 127
5.3.7 Additional Tables . . . 129
5.4 Conclusions . . . 129

6 Concluding Remarks **132**

A Tables **134**

Bibliography **157**

List of Figures

1.1 Schematic diagram of the reflection problem. The source of illuminating X-ray photons is located above the accretion disk. Both the direct power-law and the reprocessed components are detected by the observations. 9
1.2 Distribution of the Kα emission line energies for 205 spectra. Data taken from Gottwald et al. (1995). 10

2.1 Redistribution function $\psi_n(\Delta y)$ for $n = 1, 2, 3$ and 4. 20
2.2 Emergent energy spectra (solid lines) for a black body source (dashed lines) originating at depth τ_0. Note that the effect of the down-scattering in the spectrum is enhanced for larger depths. Taken from Lightman et al. (1981). 21
2.3 Emergent spectra after 50, 500 and 5000 scatterings. The black body $I_{bb}(x)$ (in red) is assumed to be the same that LLR. We also show the power law $x^{1/2}$ for low energies. 23
2.4 Element of absorbing and emitting material considered in derivation of transfer equation. 27
2.5 Plane-parallel slab with the incoming and outgoing radiation fields. . 31
2.6 Comparison between the formal solution and the Feautrier method. . 38
2.7 First moment $J(\tau)$ of the intensity calculated with the Feautrier method and the formal solution. 39
2.8 Exact solution for $u(0, \mu)$ at the surface for one angle (red), and with the Feautrier method (blue), after different number of iterations. The curves are, from the right-bottom to left-top, the corresponding for 1, 5, 10, 20 and 30 iterations. 42
2.9 Evaluation of the $H(\mu)$ function using the Simpson's rule, compared with the Chandrasekhar (1960) results and the Hapke (1981) approximation, for the conservative case ($\omega_0 = 1$). 50
2.10 Angular distribution of the intensity at $\tau = 0$ calculated with Chandrasekhar solution (in red), and with Feautrier's method (in blue). The blue curves correspond to iterations 1, 5, 25, 50 and 100, from bottom to top, with $\tau_{max} = 10$. The incidence angle is $\mu_0 = 0.5$. 52
2.11 Percentual average difference between Chandrasekhar and Feautrier solutions as a function of the maximum optical depth. 54

3.1 Temperature profiles for different illumination fluxes using constant density models ($n = 10^{15}$ cm^{-3}). The value of $\log \xi$ is shown next to each corresponding curve (models 1-10). 70

3.2 *Solid curves:* Reflected spectra for the models presented in Figure 3.1. The value of log ξ is shown next to each corresponding curve (models 1-10). The curves are shifted by arbitrary factors for clarity. These are, from bottom to top: 1, 10, 100,...,10^9. *Dashed curve:* incident ionizing spectrum (power law), corresponding to the lowest ionization case (log $\xi = 0.8$). *Dotted curve:* intrinsic disk flux (black body), common to all the models. 74
3.3 Reflected spectra as shown in Figure 3.2 in the 2-10 keV region. The value of log ξ is shown next to each corresponding curve (models 1-10). The curves are shifted by arbitrary factors for clarity. These are, from bottom to top in each panel: 1, 10, 100, $10^4, 10^5$. 76
3.4 Reflected spectra for log $\xi = 1.5$ while using a resolving power of $\mathcal{R} \sim 3500$ (model 11). All the other input parameters are the same used before (as in Figures 3.1 and 3.2), although no rescaling is applied. The strongest emission lines are labeled. 77
3.5 Reflected spectra for log $\xi = 2.5$ while using a resolving power of $\mathcal{R} \sim 3500$ (model 12). All the other input parameters are the same used before (as in Figures 3.1 and 3.2), although no rescaling is applied. The strongest emission lines are labeled. 79
3.6 Reflected spectra for log $\xi = 3.5$ while using a resolving power of $\mathcal{R} \sim 3500$ (model 13). All the other input parameters are the same used before (as in Figures 3.1 and 3.2), although no rescaling is applied. The strongest emission lines are labeled. 80
3.7 Temperature profiles (upper panel) and reflected spectra (lower panel), resulting from a constant density model with log $\xi = 2.8$ for three different incidence angles (models 14-16). In the two panels, the *red* curves corresponds to $\mu_0 = 0.95$ ($\theta \approx 0^o$, normal incidence); the *green* curves to $\mu_0 = 0.5$ (or $\theta = 60^o$); and the *blue* to $\mu_0 = 0.05$ ($\theta \approx 90^o$, grazing incidence). 82
3.8 Outgoing intensities in the 2-10 keV energy range for constant density models from 3 different ionization parameters (models 2, 5 and 8), as viewed at three different angles with respect to the normal. In all cases, the red curves corresponds to $\mu = 0.95$, the green curves to $\mu = 0.5$, and the blue curves to $\mu = 0.05$. 83

3.9 *Upper panel*: temperature profiles from a constant density model with log $\xi = 2.5$ and different iron abundances with respect to the solar values. From right to left, each curve corresponds to: A_{Fe}=0.2, 1, 2, 5 and 10 (models 17, 6 and 18-20, respectively). *Lower panel*: reflected spectra for the same models. The curves are shifted by arbitrary factors for clarity. These factors are, from bottom to top: $10^{-2}, 10^{0}, 10^{2}, 10^{4}$, and 10^{6}. The values of the iron abundance with respect to the solar value are shown at the top of each curve. 86
3.10 Reflected spectra from constant density models for three different ionization parameters (models 11-13), plotted in the 2-10 keV energy range. The red curves are the models from REFLION (Ross & Fabian, 2005), for the same input parameters. 88

4.1 Schematic view of atomic processes involved in the production of iron K-spectra. 102

5.1 Average level energy differences with respect to approximation AS1 for ions of the nitrogen isonuclear sequence with electron number $3 \leq N \leq 7$. Filled circles: valence level energies computed with AS2. Open circles: valence level energies computed with AS3. Filled squares: K-vacancy level energies computed with AS2. Open squares: K-vacancy level energies computed with AS3. 111
5.2 Average level energy differences with respect to approximation HF1 for ions of the nitrogen isonuclear sequence with electron number $3 \leq N \leq 7$. Open circles: valence level energies computed with HF2. Open squares: K-vacancy level energies computed with HF2. 112
5.3 Wavelength differences between MCDF (Chen & Crasemann, 1987) and HF2 for N IV. An average difference of 155 ± 45 mÅ is observed. 118
5.4 Wavelength differences between MCDF (Chen et al., 1997) and HF2 for N II. Differences as large as 800 mÅ are observed. 119
5.5 A-coefficient differences (s^{-1}) between MCDF (Chen et al., 1997) and HF2 for N II. It is found that MCDF is on average higher by a factor of 4. 121
5.6 Average percentage difference between Auger widths ($\log A_a \geq 12$) computed with the AS2 and AS1 approximations (filled squares) and with AS3 and AS1 (open squares). 124
5.7 Average percentage difference between Auger widths ($\log A_a \geq 12$) computed with the HF2 and HF1. 125
5.8 High-energy photoabsorption cross sections for nitrogen ions in the K-edge region. Solid curve: BPRM. Dotted curve: HULLAC. Dashed curve: Reilman & Manson (1979). 128

List of Tables

3.1 List of reflection models with their respective input parameters . . . 69

5.1 Measured and computed K-vacancy level energies (eV) 113
5.2 Computed total energies (au) for K-vacancy terms 114
5.3 Level splittings (cm^{-1}) for the $1s2s2p^2\ ^5P$ K-vacancy term of N IV . 115
5.4 Experimental and theoretical wavelengths (Å) for nitrogen ions . . . 117
5.5 Core relaxation effects on K radiative decay 120
5.6 Radiative decay routes of $1s2s^22p^3\ ^5S^o_2$ in N II 123
5.7 Discrepant Auger rates (s^{-1}) 126
5.8 Auger energy widths (au) for 1s2s2p levels in N V 127
5.9 Auger widths (meV) for K-vacancy terms in N IV 131

A.1 Valence and Auger levels for nitrogen ions 134
A.2 Radiative K-transition data nitrogen ions 139

Acknowledgements

I would like to thank my advisor Dr. Timothy Kallman for suggesting the main topic of this dissertation and for his constant guidance along its development. He has taught me a lot about high energy astrophysics, but mostly he has shown me how to be a good scientist. It has been a privilege to follow his directions. I also would like to express my gratitude to my academic advisor Dr. Steven Kraemer, and to Dr. Frederick Bruhweiler, for the help and support they have provided me since I started as a graduate student to this date.

I want to thank Dr. Michael Witthoeft for all his support, in particular for his help on the photoionization calculations of nitrogen with the code *R*-Matrix. Thanks to Drs. Claudio Mendoza and Manuel Bautista for their support on the atomic structure calculations. Also, thanks to Drs. Patrick Palmeri and Pascal Quinet who provided the HFR calculations for nitrogen ions. The HULLAC photoionization calculations were carried out by Drs. Ehud Behar and Marcel Klapisch. Many thanks to Professor Randy Ross who carefully reviewed the results concerning the reflection models (Chapter 3), and for his valuable comments. I would like to thank Dr. Richard Mutshotzky for many insightful discussions about the results of this project.

I have been lucky to find the best friends during my time as a grad student. Thanks to Marcio, John and Ciprian for many memorable lunch-time conversations. Thanks to my office mate at the old building 2, Keigo Fukumura, for being such a good friend, and to Demos Kazanas for his many recommendations and advice that help me to understand the basic theory of accreting sources. Thanks to Pamela Level who has help me countless times with my paperwork at GSFC-NASA. Special thanks to the staff at the physics department of Catholic University of America, in particular to Gail Hershey, who truly is the "center of our galaxy". Also to Lee Riley for processing the paperwork concerning all my travels.

I cannot thank enough to my family for their support. To my wife Sahar, I owe most of my accomplishments, including this dissertation. With infinite patience she has help me listening my talks, reading and correcting all my papers, posters and figures. Mostly, she is responsible for all the beautiful things in this manuscript, and in my life. *Shoukran hayati*.

This research was funded in part by the NASA Astronomy and Physics Research and Analysis Program and by a grant from the NASA Astrophysics Theory Program 05-ATP05-18. This research has made use of NASA's Astrophysics Data System.

The most exciting phrase to hear in science, the one that heralds new discoveries, is not 'Eureka!' (I found it!) but 'That's funny ...'

Isaac Asimov (1920 - 1992)

1 Introduction

1.1 Historical Background

The beginning of the 20th century was marked with the development of two of the greatest achievements in modern physics, the relativity theory and the quantum mechanics. Interestingly, German physicist Albert Einstein played a fundamental role in both fields, being the author of the former and a major contributor to the latter. In the spring of 1905, Einstein submitted a paper entitled "On a Heuristic View concerning the Production and Transformation of Light" (Einstein, 1905a), where he suggested that light should be considered as a collection of independent particles of energy, using Max Planck's postulate of the quantum as the fundamental unit of light. He explained the photoelectric effect, which holds that for each electron emitted a specific amount of energy is absorbed. This theory formed the basis for the quantum mechanics. In a second paper entitled "On the Electrodynamics of Moving Bodies" (Einstein, 1905b), he presented a theoretical essay that came to be known as the special theory of relativity, radically changing our understanding of energy, mass and time. Ten years later, his general theory of relativity (Einstein, 1915) changed our understanding of space and time and how gravity affects the universe.

Among the many extraordinary predictions of the general relativity theory is the possibility that stars could collapse under their own gravity, and that the space, or in

fact the *spacetime* around them became so curved that they would be disconnected from the rest of the Universe. Shortly after the theory of general relativity was published, Karl Schwarzschild used Einstein's field equations to predict that under such situations the gravitational force in the region around the collapsed star will be so great that no particle will be able to escape from it, not even a photon. These dead stars known as *black holes*, are probably the most mysterious objects in the Universe, and they constitute one of the few cases in which a great prediction was made solely on the basis of thought, decades before any observational evidence could be found.

The detection of a black hole is not trivial a matter. One could imagine looking at the sky for a moving dark spot which occults the light of the stars behind it. However, black holes are compact objects located at very large distances. For instance, the apparent size of a black hole with 50 kilometers diameter located at 4 light-years distance (the distance to the closest of all stars, Alpha Centauri), will be equivalent to the apparent size of a human hair located at the moon. This would require telescopes millions of times more powerful than the current ones to detect it. Thus, black holes can only be observed indirectly through the influence they exert on their environment. This was understood by Yakov Zel'dovich at the beginning of the 1960's (Thorne, 1994), who started working on finding a way to indirectly detect black holes. He, together with Edwin Salpeter and Igor Novikov, realized the following scenario: some stars are known for blowing strong winds of gas off their surfaces. If a black hole and one of these stars happened to be orbiting each other (a binary system), then the black hole will capture some of the wind material (mostly hydrogen and helium), heat it in a shock front, and produce radiation. They estimated that the temperature of the shocked gas should be of the order of several millions of degrees. Thus, instead of emitting visible light, this gas should shine bright with X-rays. The problem is that the earth's atmosphere is opaque to X-rays, and for the decade of the 1960's X-ray telescopes were extremely primitive (Thorne, 1994).

During the same decade, the cold war was the driving force for many scientific experiments. Both the Soviet Union and the United States were testing nuclear weapons, and the U.S. Air Force was interested in developing flying X-ray detectors

to monitor future Soviet bomb tests. A team lead by Riccardo Giacconi started designing, building and testing a variety of weapons-blast monitoring instruments. However, in June of 1962 the team took its first astronomical step, flying an X-ray detector on an Aerobee rocket above the atmosphere in search of X-rays from the moon. Instead, they found a signal 5000 times brighter than expected that was coming from the Scorpius constellation. After months of reviewing the data, they announced the discovery of the first X-ray star detected (Giacconi et al., 1962), with the name Sco X-1 (Sco for the Scorpius constellation, X for X-ray source, and 1 for being the brightest). This and other teams continued in the improvement of the detectors. In 1970 the Giacconi team launched *Uhuru*, the first X-ray satellite, which discovered and cataloged 339 X-ray sources (Giacconi et al., 1974), marking the beginning of X-ray astronomy on a large scale.

1.2 Compact Objects and Accreting Sources

Compact objects are the end products of stellar evolution; they are born when normal stars die. There are three types of compact objects, white dwarfs, neutron stars and black holes. The primary factor determining whether a star ends up as any of these three objects is its mass. White dwarfs originate from small stars with masses $M \lesssim 4M_{\odot}$ (where $M_{\odot} \sim 2 \times 10^{30}$ Kg is the mass of the Sun). According to numerical calculations, white dwarfs cannot exceed $1.4M_{\odot}$ (Chandrasekhar, 1931). The progenitor star of a white dwarf probably undergoes a relatively gentle mass ejection at the end of its evolutionary lifetime, perhaps forming a planetary nebula. Neutron stars and black holes originate from more massive stars, although the lines that separate stars that become black holes or neutron stars is uncertain since the final stages of the evolution of massive stars is poorly understood. Neutron stars have a maximum mass which ranges $1.4 - 3M_{\odot}$ (Bombaci, 1996).

These three types of compact objects differ from a normal star in two fundamental properties. First, they do not burn nuclear fuel in their interior, and therefore they are not able to sustain themselves against gravitational collapse by means of internally

generated energy. Instead, white dwarfs and neutron stars are supported by the pressure exerted by degenerate electrons and degenerate neutrons, respectively. On the other hand, black holes are completely collapsed objects, meaning that there is no other force to balance gravity and they have collapsed into a *singularity*. The second fundamental difference between compact objects and normal stars is their size. Although they can have comparable mass, compact objects have much smaller radii and thus, much stronger surface gravity.

White dwarfs are very dense stars with a mass comparable to that of the Sun, but with a volume comparable to that of the earth. They radiate away the thermal energy left over from their collapse, which is characterized by a effective temperature of around 7000-10000 Kelvin, and thus a radiation that looks white to the naked eye. Neutron stars are almost exclusively made of neutrons (hence their name), due to the elimination of electrons and protons via inverse β-decay. No light, or anything else for that matter, can escape from a black hole.

There are alternative scenarios under which a black hole can be formed other than the total gravitational collapse. For instance, either a white dwarf or a neutron star can increase its mass if it is bound to a normal star on a binary system, by accreting material. Because there is a maximum mass that they can have, this process can eventually lead to the formation of a black hole. Contrary to white dwarfs and neutron stars, there is not restriction in the total mass of a black hole, it can range from the *stellar* regime with masses of $M \sim 10 M_{\odot}$, up to *supermassive black holes* with masses of $M \sim 10^6 - 10^9 M_{\odot}$. Supermassive black holes are believed to exist in the nuclei of galaxies (including our own Milky Way), which has been confirmed by measurements of the orbital speeds of the stars close to the nucleus (Kormendy & Richstone, 1995; Genzel & Eckart, 1998; Ghez et al., 2008). The luminosities of the accreting compact objects, such as X-ray binaries, that populate the Milky Way are known to be as high as $\sim 10^5 L_{\odot}$, while in many galaxies harboring a supermassive black hole in their center the luminosity can exceed that by seven to even nine orders of magnitude. These are usually referred to as *active galactic nuclei* (AGN). Supermassive black holes are also proposed to explain the violent activity observed in the most luminous

time-steady objects in the universe, quasars.

Following the Salpeter-Zel'dovich idea that gas streams falling to a black hole should collide and produce radiation, Donald Lynden-Bell devised a more complete and realistic description of how supermassive black holes might power quasars and galactic nuclei (Lynden-Bell, 1969). He argued that after the gas streams collide, they will join together, and the centrifugal forces will make them spiral around the black hole many times before reaching it. In order to obey conservation of angular momentum, the falling gas should form a disk, similar to the rings around Saturn. He called this an *accretion disk*, since the gas is continuously accreting towards the black hole. In the accretion disk, adjacent gas streams will run against each other, and the friction produced will heat the disk to high temperatures.

We now know that the extraction of gravitational potential energy from material through accretion is likely the most efficient and powerful mechanism for the production of high-energy radiation. This can be shown by simple order-of-magnitude estimates. For a body of M and radius R, the gravitational potential energy released by accretion of a particle of mass m onto its surface is

$$\Delta E_{acc} = GMm/R, \tag{1.1}$$

where G is the gravitation constant. In the case of nuclear fusion reactions, which occur at the interior of a star (the burning of hydrogen), no more than 1% of the rest mass will be emitted as energy, or

$$\Delta E_{nuc} = 0.01mc^2, \tag{1.2}$$

where c is the speed of light. Assuming that the compact object has a radius of $R \sim 10$ km and a mass $M \sim M_{\odot}$, which are typical values of a neutron star, one obtains $\Delta E_{acc}/\Delta E_{nuc} \sim 20$. In fact, more detailed estimates predict that up to 40% of the rest mass of the accreted material can be emitted as radiation (McClintock & Remillard, 2006).

1.3 Early X-ray observations

The first observations of X-ray sources using rockets and balloon type detectors flown during the 1960's discovered not only sources within the Milky Way but also much farther away, such as the extra-galactic sources, 3C 273 and Centaurus A (Bowyer et al., 1970). The *Uhuru* satellite confirmed the detection of several sources previously identified as active galactic nuclei (AGN) (Giacconi et al., 1974). The *Ariel-V* observatory later showed that X-ray emission is a common property of AGN and found sources in which the X-ray flux varied significantly on time scales shorter than one day (Elvis et al., 1978). The *Ariel V* data, in combination with *Uhuru, OSO-8* and *HEAO-1* established that in the 2-10 keV regime AGN spectra could be parametrized by power-law continua $E^{-\Gamma}$ with a mean slope (photon index) for the sample of $\Gamma \sim 1.7$ (e.g. Tucker et al., 1973; Mushotzky, 1976, 1984).

In 1978 the *Einstein* observatory was launched. It provided focusing X-ray optics and high sensitivity which increased the number of AGN detections by an order of magnitude. It revealed a soft-band (0.1-2 keV) complexity (Wilkes & Elvis, 1987), that led to suggestions that the gas only covers a fraction of the line-of-sight. *Einstein* observations of variations in absorption for the quasar MR 2251-178 led Halpern (1984) to the first suggested detection of a partially ionized absorber in AGN, dubbed warm absorber.

The European X-ray Observing satellite *EXOSAT* had a 3 year mission (1983-1986), providing great contributions such as the detailed study of rapid variability in AGN (Green et al., 1993). Its broad bandpass was also key in the detection of an excess of soft-band X-ray flux (the so called *soft excess*), seen in about 50% of AGN (Turner & Pounds, 1989). Additionally, *EXOSAT* also detected iron emission in some of the brightest sources (Leighly et al., 1989; Ghosh et al., 1992), also confirmed by *OSO-8* data (Mushotzky et al., 1978), and the Japanese satellite *Tenma* (Miyoshi et al., 1986). Holt et al. (1980) suggested that Fe emission lines found in *Einstein* spectra originate from the same gas resposable for the partial covering absorption.

Japan launched *Ginga* in 1987, which provided a large area proportional counter

yielding good spectra over the 2-30 keV energy band, whose data established Fe Kα fluorescence emission to be a common property of many Seyfert galaxies (Pounds et al., 1989, 1990; Matsuoka et al., 1990; Nandra & Pounds, 1994) The detection of a deep Fe K edge was consistent with originating in a neutral gas and supported the picture of a strong contribution from a reprocessed X-ray component. *Ginga* spectra also showed absorption edges from ionized species of iron (Fe XXIV-XXVI), in about 50% of Seyfert spectra (Nandra & Pounds, 1994), indicating a significant column density ($N_H \sim 10^{23}$ cm^{-2}) of highly ionized material exist in these nuclei.

The German satellite *ROSAT* was launched in 1990 carrying instruments to cover the soft X-ray band. Individual absorption features were found in several objects in the 0.1-2 keV energy range, including the detection of an absorption feature at 0.8 keV in MCG–6-30-15 (Nandra & Pounds, 1992). Several other bright Seyfert galaxies had sufficiently strong individual features that distinct zones of ionized gas could be isolated (Nandra et al., 1993; Turner et al., 1993a,b; Pounds et al., 1994). Further AGN *ROSAT* observations confirmed the relevance of ionized gas in Seyfert galaxies (Mihara et al., 1994; Ptak et al., 1994; Weaver et al., 1994; Yaqoob et al., 1994; Guainazzi et al., 1994).

The launch of the Japanese *Advanced Satellite for Cosmology and Astrophysics, ASCA* (Tanaka et al., 1994) in 1993 offered a significant improvement in spectral resolution with the first flight of CCDs on an X-ray observatory. Of particular interest was the possibility of measuring strong distortions (blurring) of the Fe K emission line contributions produced in regions very close to the black hole, provided the line was strong and not confused with other spectral signatures. Indeed, a strong spectral curvature around 6 keV was observed in many Seyfert galaxies and an interpretation made as an Fe K emission line, heavily broadened and redshifted by relativistic effects close to the event horizon (Tanaka et al., 1995; Nandra et al., 1997; Fabian et al., 2000).

1.4 X-ray reflected spectra

All accreting black holes emit a significant fraction of their bolometric luminosity as X-rays. For example, it is thought that AGN radiate about $10 - 20\%$ of the total energy output above 2 keV. Because X-rays are only produced in very hot environments, it is likely that they originate from the inner regions of the accretion disc. Thus, X-ray observations are needed to fully understand the physics of these systems. The X-ray continuum spectra vary from source to source, and can vary in time as well, but for our purposes it is adequate to think of accreting black holes as exhibiting power-law continua that extend up to hard X-ray energies ($\sim 10^5$ eV). The first spectral observations of AGN had poor energy resolution, but determined that the continuum is characterized by a power-law with photon-index Γ that in most cases is about ~ 2.

If an optically thick accretion disc surrounds the compact object, and if the X-ray continuum flux irradiates the disc, then the spectral signatures of the interaction of the continuum and the disc are expected to imprint themselves on the overall spectrum (Basko, 1978; Guilbert & Rees, 1988). This impression is known as *reflection*. In both AGN and X-ray binaries, it is thought that the material responsible for the reflection is the accretion disk and that the source of X-rays lies above it in a hot corona. The Figure 1.1 shows a cartoon picture of this situation. Photons from the disk with ultraviolet (UV) energies interact with the hot electrons via inverse Compton scattering and gain energy, producing the observed power-law X-ray continuum emission. However, this power-law spectrum also illuminates the accretion disk, which reprocesses the radiation, emitting a reflection spectrum. This is a new observable component which carries information about the state of the material in the accretion disk, such as elemental abundances, temperature and density structure, velocity and ionization state of the gas.

When an X-ray photon enters the relatively cold gas of the accretion disk, it is subject to a number of possible interactions. An incident photon is either absorbed by photoionizing an ion in the disk or scattered back by Compton scattering. Ioniza-

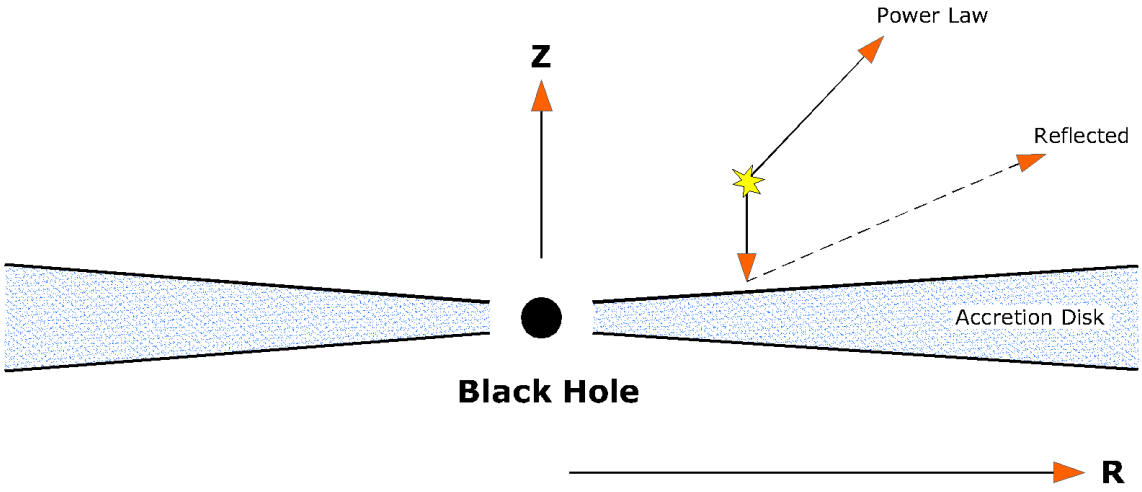

Figure 1.1 Schematic diagram of the reflection problem. The source of illuminating X-ray photons is located above the accretion disk. Both the direct power-law and the reprocessed components are detected by the observations.

tion can be followed by Auger de-excitation (emission of electrons), or by radiative decay with the emission of a fluorescent line photon which eventually escapes the slab. Therefore, in addition to the power-law continuum, the reflection component is responsible for several atomic emission and absorption features. The *Ginga* observatory discovered that almost all Seyfert galaxies have a strong iron Kα emission line at 6.4 keV (Pounds et al., 1990; Nandra & Pounds, 1994). Gottwald et al. (1995) also stressed the ubiquity of iron lines from compact sources, analyzing more than 430 EXOSAT X-ray binary spectra. In Figure (1.2) we show an histogram for the distribution of the iron line energies contained in Table 2 of Gottwald et al. (1995). Most of the line energies are between 6.4 - 6.8 keV.

The fluorescent iron line is produced when one of the two K-shell ($n = 1$) electrons of an iron atom is ejected following the photoelectric absorption of an X-ray. Following the photoelectric event, the resulting ion in the excited state can decay in one of the two ways. One of the electrons in the L-shell ($n = 2$) needs to fill the hole left in the

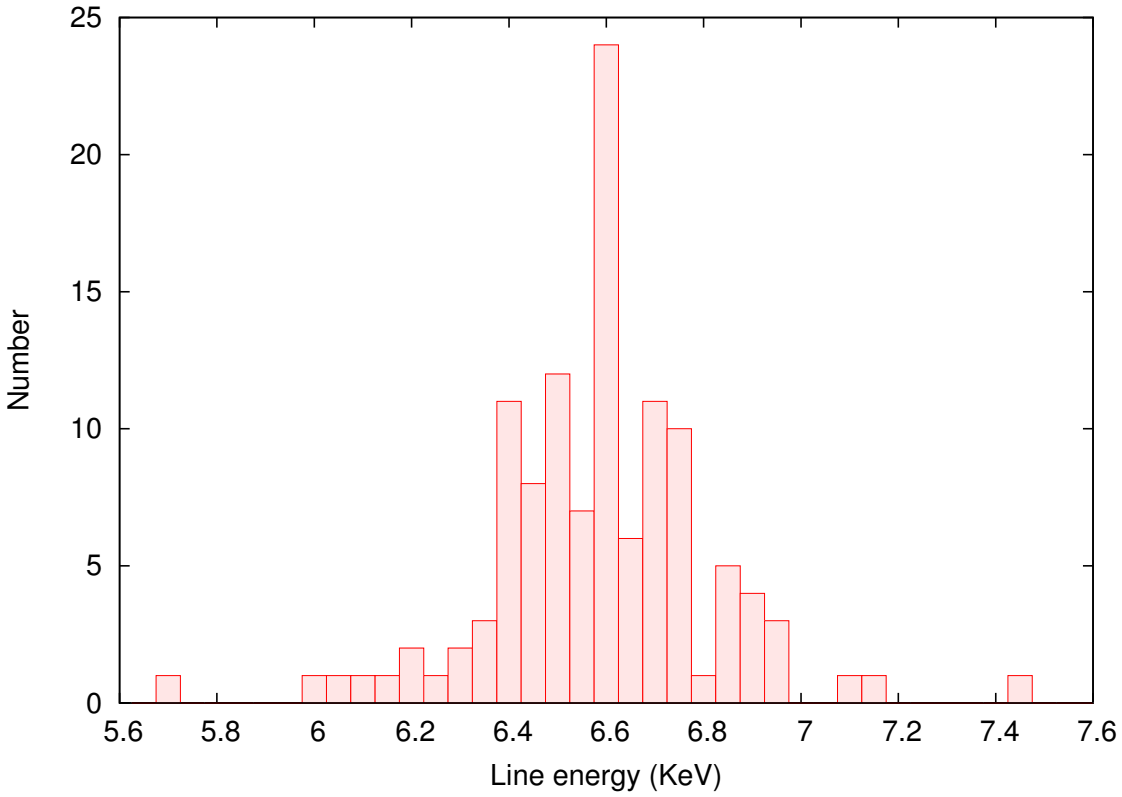

Figure 1.2 Distribution of the Kα emission line energies for 205 spectra. Data taken from Gottwald et al. (1995).

K-shell, for which it needs to lose a certain amount of energy, specifically 6.4 keV. The ion can either emit a photon (34% of probability), or it can release an Auger electron (66% probability).

The hard X-ray spectrum of an accretion disc also shows deviations from a power-law due to the *Compton scattering* of photons by cold electrons in the gas, which hardens the spectrum between 8 and 20 keV (Rybicki & Lightman, 1979). Since the material in the accretion disc moves toward the center losing energy and angular momentum as a consequence of the viscosity, the excess of energy increases the temperature of the gas and produces black body radiation. The peak of the Planckian is detectable at energies typically below ~ 1 keV.

These are the main processes that affect the shape and profile of the reflected spectra from accretion discs around black holes. Each one must be treated carefully, and many theoretical and numerical problems arise if one hopes to work from first principles. Such calculations are non-trivial since they involve the calculation of both the thermal and ionization balance in a relatively large column of irradiated gas. Additionally, the material in an accretion disk is optically thick and full of electrons, and thus Compton scattering, which redistributes photon energies, will play an important role in the radiation transfer. Finally, the added atomic physics complexities in predicting spectral lines and other atomic features results in very detailed calculations.

Much theoretical effort has gone into studies of X-ray illuminated disks over the past few decades. Most of such models commonly assumed that the gas density is constant with depth (Lightman & White, 1988; George & Fabian, 1991; Matt et al., 1993; Zycki et al., 1994). Although constant density models may be appropriate for radiation-pressure dominated disks, recent studies have shown significant differences when the gas density is properly solved via hydrostatic equilibrium (Nayakshin et al., 2000; Nayakshin & Kallman, 2001; Ballantyne et al., 2001). However, all past models have included only primitive treatments of the atomic processes affecting the excitation and emission from different elements, namely nitrogen, oxygen, calcium, and iron.

1.5 This Dissertation

This thesis focuses on the study of X-ray illuminated accretion disks around black holes by modeling their structure and reprocessed spectra. Implementation of a self-consistent approach combined with the most updated atomic data provides a significant improvement in the understanding of X-ray observations of these systems. Comparison of observations and theoretical models present the opportunity to learn about the accretion disk structure. This can be done by analyzing atomic lines, absorption edges, recombination continua and the Compton bump, among other features

in the spectrum.

The effects of incident X-rays on the surface of an accretion disk are studied by solving simultaneously the equations of radiative transfer, pressure balance and ionization equilibrium over a large range of column densities. Plane-parallel geometry and azimuthal symmetry can be assumed, such that each calculation corresponds to an annular ring at a given distance from the black hole. The radiation transfer equations are solved by using the Feautrier scheme (Mihalas, 1978). Ionization and thermal balance are solved by using the photoionization code XSTAR (Kallman & Bautista, 2001), including the most recent and complete atomic data for the K-shell of the isonuclear sequences of iron (Kallman et al., 2004), oxygen (García et al., 2005), and the recently published sequences for Ne, Mg, Si, S, Ar, Ca (Palmeri et al., 2008a), and Ni (Palmeri et al., 2008b). Redistribution of photons due to Compton scattering is included using a Gaussian approximation for the Compton kernel.

Other relevant ions are also included in the models, since new atomic data have recently become available. However, there are no reliable atomic data for X-ray transitions from nitrogen ions. Therefore, this thesis also includes the calculation of the atomic structure and inner-shell photoabsorption cross sections for the nitrogen iso-nuclear sequence (i.e., N, N^{+}, N^{2+},...,N^{6+}).

For the calculation of the atomic data for nitrogen ions, namely, level energies, wavelengths, gf-values, radiative widths, total and partial Auger widths, and total and partial photoionization cross sections; we have used a portfolio of publicly available atomic physics codes: AUTOSTRUCTURE (Badnell, 1997), HFR (Cowan, 1981), and BPRM (Seaton, 1987). The inclusion of these data in the accretion disk models provide insight into the physical conditions of the systems where nitrogen lines can be observed.

This dissertation is presented in the following way. In Chapter 2 the basic theory concerning reflection of X-ray from accretion disks is discussed. In particular, Section (2.1) briefly describes the basic concepts regarding the accretion power onto black holes, the Shakura & Sunyaev standard model, and the equations of hydrostatic equilibrium required to determine the temperature and pressure profiles in the ver-

tical direction, perpendicular to the disc plane. Section (2.2) contains the discussion on the Comptonization of hard X-rays by a cold media, comparing the Gaussian approximation with the Green's function method. Perhaps the most important part of Chapter 2 is the radiation transfer section, in particular the discussion of the accuracy of the Feautrier method versus the formal solution and the Chandrasekhar approach, which are outlined in Section (2.3).

In Chapter 3 the main results of this dissertation are presented. Section 3.2 describes the theory and numerical methods concerning the radiation transfer, ionization and energy equilibrium, and the atomic data used in the calculation of the models of the X-ray reflected spectra from accretion disks. In Section 3.3 a set of models for constant density atmospheres is presented, covering different degrees of ionization, viewing and incidence angles, as well as the effect of the abundance on the reflected spectrum. The main conclusions of these results are summarized in Section 3.4.

Chapter 4 is a short review of the theory of the atomic structure, and describes the general aspects of the codes used in the calculation of both atomic structure and the photoionization problem (Section 4.2). A few concepts associated with the emission of the iron K-lines are mentioned in Section (4.3).

Chapter 5 contains a report on calculations of energy level structure and bound-bound and bound-free transition probabilities for the K-shell of nitrogen ions. The numerical methods are briefly described in Section 5.2 while an analysis of the results based on comparisons with previous experimental and theoretical values is carried out in Section 5.3. Some conclusions for this Chapter are discussed in Section 5.4.

2

Theory of Accretion and Radiative Transfer

2.1 Accretion onto Black Holes

Before discussing the models for the origins of the observed X-ray spectral features in compact objects, it will be useful to review some of the basic results from accretion disc theory. A complete treatment of the theory of accretion discs can be found in Shakura & Sunyaev (1973), hereafter SS73, and Novikov & Thorne (1973).

The two most important quantities to describe an accretion disk around a black hole are the mass M of the black hole, and the rate at which mass from the accretion disk is falling into the black hole, $\dot{M}$. The total mass determines the size scale of the system trough the *Schwarzschild radius*, the radius of the event horizon in a non-spinning black hole:

$$R_s = \frac{2GM}{c^2} \tag{2.1}$$

where G is the Newtonian gravitation constant and c is the speed of light, or the *gravitational radius*,

$$R_g = \frac{GM}{c^2} = \frac{R_s}{2} \tag{2.2}$$

This radius can be really small compared with other stellar objects. For example, for a black hole of 10^8 solar masses ($M = 10^8 M_\odot$), and with $M_\odot \sim 2 \times 10^{30}$ Kg, $G \simeq 6.67 \times 10^{-11}$ m^3 Kg^{-1} s^{-2}, $c \sim 3 \times 10^8$ m s^{-1}; we obtain $R_s \simeq 2.6$ Km, and $R_g \simeq 1.3$ Km, much smaller than the radius of the moon!.

On the other hand, the accretion rate defines the total luminosity of the system

$$L = \eta \dot{M} c^2 \tag{2.3}$$

Here η is the efficiency of converting the rest mass energy of the infalling material into radiation. This equation shows that one observer will see the system brighter if a larger amount of material is accreted into the black hole. The outgoing radiation would scatter off the gas at larger radii and exert an outward force in the radial direction. It is clear then that there exist some critical accretion rate at which the radiation pressure stops the accretion of material. This situation is known as the *Eddington limit*. Assuming spherical accretion of a hydrogen gas onto a compact object of mass M, if the gravitational attraction at a radius r is balanced with the radiation pressure:

$$\frac{GMm_p}{R^2} = \frac{L\sigma_T}{4\pi R^2 c} \tag{2.4}$$

where m_p is the mass of the proton (much larger than the electron mass), and $\sigma_T = 8\pi e^4/3m_e^2c^4$ is the Thomson cross section for electron scattering, then the *Eddington Luminosity* is

$$L_{Edd} = \frac{4\pi GMm_p c}{\sigma_T} \simeq 1.26 \times 10^{46} \left(\frac{M}{10^8 M_\odot}\right) \text{erg s}^{-1} \tag{2.5}$$

This luminosity also implies a critical accretion rate given by

$$\dot{M}_{Edd} = \frac{L_{Edd}}{\eta c^2} \simeq 2.78 \left(\frac{M}{10^8 M_\odot}\right) \left(\frac{0.08}{\eta}\right) M_\odot \text{ yr}^{-1} \tag{2.6}$$

The efficiency of accretion can be estimated by comparing the binding energy of a particle at the innermost stable orbit with its rest mass energy $E = mc^2$. For a non-spinning black hole the minimum radius in the disc at which stable circular orbits are possible is called *radius of marginal stability*, $R_{ms} = 3R_s = 6R_g$ (Kaplan, 1949). From (2.2) we see that $R_{ms} = 6GM/c^2$, and using the Newtonian expression for the binding energy

$$E_b = \frac{GMm}{2R_{ms}} = \frac{mc^2}{12} \tag{2.7}$$

then

$$\eta = \frac{1}{12} = 0.08 \tag{2.8}$$

A more detailed calculation taking into account the space curvature close to the black hole reduces the binding energy and gives a different value, $\eta = 0.057$ (Salpeter, 1964).

2.1.1 Sakura & Sunyaev standard model

The standard theory developed by SS73 considers a geometrically thin accretion disc (i.e. $H \ll R$, where H is the scale height at R), such that the gas particles follow Keplerian orbits at each radius and the inward radial speed is much smaller than the rotation velocity. The internal viscosity of the gas produces a loss of energy and angular momentum of the particles. The excess of energy will be used to heat the gas and is ultimately radiated away. The emerging flux at each radius, assuming the same accretion rate over the disc, is given by

$$F_d(R) = \frac{3GM\dot{M}}{8\pi R^3}\left[1 - \left(\frac{R_{ms}}{R}\right)^{1/2}\right] \tag{2.9}$$

or

$$F_d(R) = \frac{3GM\dot{M}}{8\pi R^3}\left[1 - \left(\frac{3R_s}{R}\right)^{1/2}\right] \tag{2.10}$$

Using the *Stefan-Boltzmann* relation $F = \sigma T^4$; then the effective temperature at that radius is

$$T_{eff}(R) = \left[\frac{F_d(R)}{\sigma}\right]^{1/4} \tag{2.11}$$

or

$$T_{eff}(R) = \left\{\frac{3GM\dot{M}}{8\pi\sigma R^3}\left[1 - \left(\frac{3R_s}{R}\right)^{1/2}\right]\right\}^{1/4} \tag{2.12}$$

where $\sigma \simeq 5.67 \times 10^{-5}$ erg cm^{-2} s^{-1} K^{-4}, is Stefan's constant. Therefore, we see that R, M and $\dot{M}$ determines the structure of the disc in the standard model. Also, SS73 found that for fixed values of M and $\dot{M}$, the disc can be divided into three regions depending on R: the *outer region* at a large R, in which gas pressure dominates radiation pressure and the opacity is controlled by free-free absorption; the *middle region*

at smaller R, in which gas pressure is dominated by radiation pressure but opacity is mainly due to electron scattering; and the *inner region* at very small R, where radiation pressure dominates over the gas pressure, but still scattering dominates the absorption opacity. For some values of the accretion rate, the middle region may not exist.

Since we are interested in the *inner region*, we only summarize the important equations of SS73 for the radiation dominated case. Those are:

the half-thickness

$$z_0 = \frac{3}{8\pi}\frac{\sigma_T \dot{M}}{c}\left(1 - r^{-1/2}\right) \tag{2.13}$$

the temperature

$$T = 2.3 \times 10^7 \left(\alpha m\right)^{-1/4} r^{-3/8} \tag{2.14}$$

the optical depth

$$\tau = 8.4 \times 10^{-5} \alpha^{-17/16} m^{-1/16} \dot{m}^{-2} r^{-93/32} \tag{2.15}$$

Where we used the dimensionless parameters definitions

$$m \equiv \frac{M}{M_\odot} \quad \dot{m} \equiv \frac{\dot{M}}{\dot{M}_{Edd}} \quad r \equiv \frac{R}{3R_s} \tag{2.16}$$

Then we also can calculate the scale height $H = z_0/r$, and the density with

$$n = \frac{u_0}{2m_p z_0}, \qquad \text{with} \;\; u_0 : \text{surface} \;\; \text{density} \tag{2.17}$$

So we also can have an estimate of the pressure of the gas. The α-parameter that appears in Equations (2.14) and (2.15) comes from the prescription that the viscosity ν in the gas is given by

$$\nu = \alpha c_s H, \tag{2.18}$$

where c_s is the sound speed.

2.2 Comptonization of X-rays by cold electrons

Comptonization is the process by which photons can gain or lose energy by scattering off thermal electrons. The process has proven to be significant for the generation of X-rays emitted from gas accreting onto compact objects, because hot electrons ($\sim 10^9$ K) are cooled by giving some of their energy to UV photons which are then scattered to X-ray energies (Shapiro et al., 1976).

The opposite situation occurs when the temperature of the electrons is small compared with the energy of the photons ($kT \ll h\nu$), especially when the incident photons are in the X-ray band ($0.1 \leq h\nu \leq 10^6$ eV). In this case each photon delivers part of its energy to the electrons in the gas, after each scattering (Shapiro & Teukolsky, 1986).

2.2.1 Green's function method

In order to solve the problem of Comptonization of X-rays, Lightman et al. (1981) (hereafter LLR) derive the Green's functions for scattering of photons by cold electrons in plane-parallel, semi-infinite geometry, with the photon source located at an arbitrary depth in the medium.

In a non-relativistic approximation, LLR adopted a formalism for computing the emergent photon number spectrum $G(y)$, from an initial monochromatic spectrum at wavelength y_0, using the expression

$$G(y, y_0) = \sum_{n=0}^{\infty} P_n \psi_n(y, y_0) \tag{2.19}$$

where $y \equiv \lambda/\lambda_c$, and $\lambda_c = h/m_e c$ is the Compton wavelength. In this equation, P_n is the probability of photon escape from a finite medium after n scatterings, and ψ_n is the wavelength distribution of photons scattered n times in a infinite medium. Lightman & Rybicki (1980) developed a technique to calculate directly the probability P_n without solving the time-dependent problem. In particular at the surface

$$P_n = \frac{(2n)!}{(2n-1)(2^n n!)^2} \quad (\tau = 0) \tag{2.20}$$

and for many scatterings ($n \gg 1$); $P_n \sim 2n^{-3/2}$. On the other hand, Illarionov et al. (1979) calculated the exact spectral distribution of photons ψ_n after n scatterings. This work both corrects the error of the Kompaneets equation (Kompaneets, 1957) in the limit of low temperature, and allows the scattering to be treated as a discrete process, which is important for small numbers of scatterings. In the non-relativistic limit, they found

$$\psi_n(\Delta y) = \int d\xi \psi_{n-1}(\xi)\Theta(1 - |\Delta y - \xi - 1|)\frac{3}{8}\left[1 + (\Delta y - \xi - 1)^2\right] \tag{2.21}$$

where $\Delta y \equiv y - y_0$, and $\Theta(x)$ is the Heaviside function (i.e. $\Theta(x) = 1$ for $x > 0$, and zero otherwise). For n larger than 3 or 4, ψ_n is well approximated by a Gaussian

$$\psi_n(\Delta y) \simeq \left(\frac{5}{4\pi n}\right)^{1/2} \exp\left[\frac{-5(\Delta y - n)^2}{4n}\right] \tag{2.22}$$

We show the results for the first four scatterings in Figure (2.1), using the integral (2.21) for $n = 1, 2$; and the Gaussian approximation (2.22) for $n = 3, 4$.

For an input spectrum $I(y)$, the emergent radiation is the convolution

$$S(y) = \int_0^y G(y - \xi)I(\xi)d\xi \tag{2.23}$$

Integration over all y gives

$$\int_0^\infty S(y)dy = \int_0^\infty dy \int_0^y G(y - \xi)I(\xi)d\xi = \int_0^y I(\xi)d\xi \int_0^\infty G(y - \xi)dy \tag{2.24}$$

but G satisfies the normalization

$$\int_0^\infty G(y, y_0)dy = 1 \tag{2.25}$$

so

$$\int_0^\infty S(y)dy = \int_0^\infty I(y)dy \tag{2.26}$$

Therefore the normalization of G yields conservation of the number of photons. As an example, LLR solve the case where the source spectrum is a black body,

$$I_{bb}(x) = x^3\left[\exp\left(x\frac{mc^2}{kT}\right) - 1\right]^{-1} \tag{2.27}$$

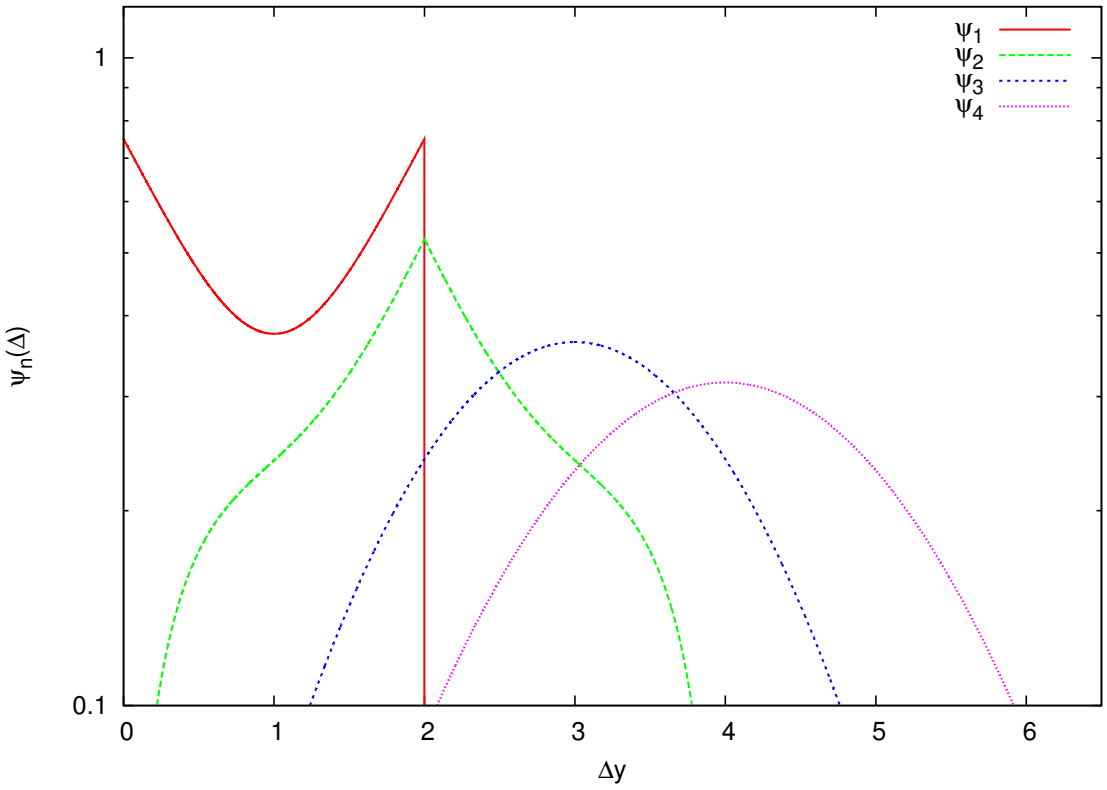

Figure 2.1 Redistribution function $\psi_n(\Delta y)$ for $n = 1, 2, 3$ and 4.

where $x \equiv E/m_e c^2 = 1/y$. The temperature of the black body was set to $kT/mc^2 = 0.02$, and the results for two different optical depths are shown in the Figure (2.2). The LLR results show the shape of the emergent spectra after many scatterings, and how the low-energy shape follows the $x^{1/2}$ power law in both cases, as the result of the asymptotic $n^{-3/2}$ law for the probability of a photon to emerge from the semi-infinite medium.

2.2.2 Gaussian approximation

The Compton scattering can be also treated as an approximation similar to (2.22), in which the scattered photons are assumed to be distributed according to a Gaussian

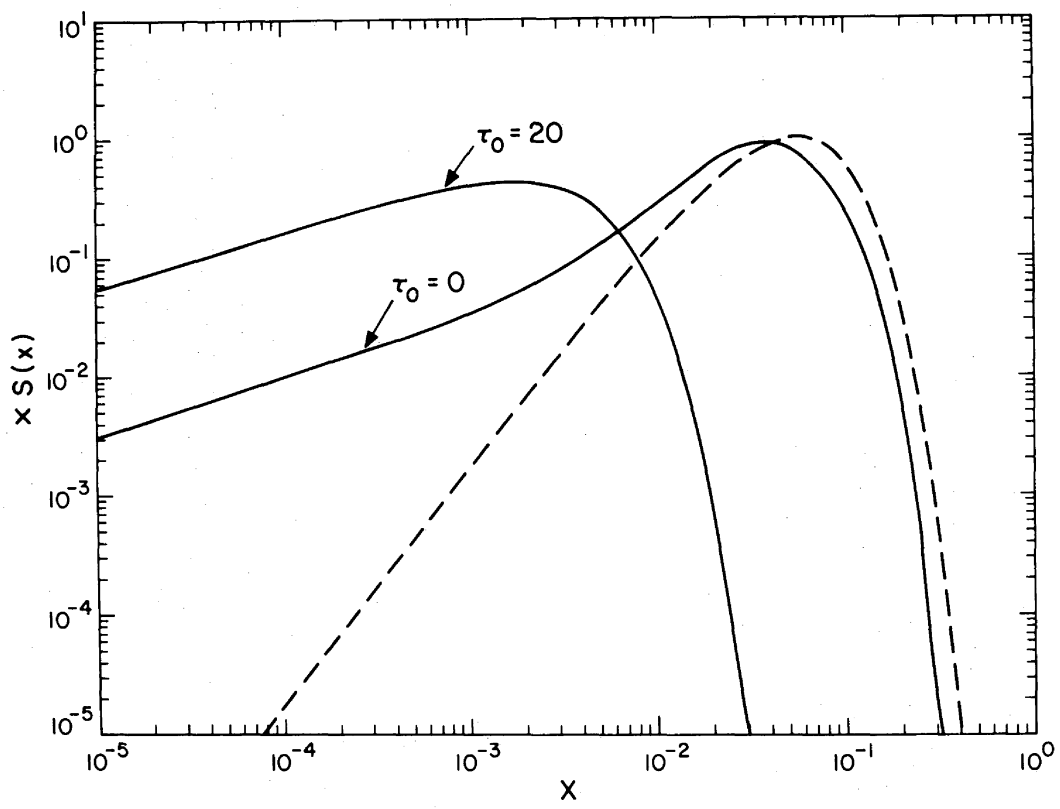

Figure 2.2 Emergent energy spectra (solid lines) for a black body source (dashed lines) originating at depth τ_0. Note that the effect of the down-scattering in the spectrum is enhanced for larger depths. Taken from Lightman et al. (1981).

profile normalized to unity (Nayakshin et al., 2000; Ross & Fabian, 1993),

$$P(E_c, E_s) = \frac{1}{\sigma\pi^{1/2}} \exp\left[\frac{-(E_s - E_c)^2}{\sigma^2}\right] \tag{2.28}$$

centered at

$$E_c = E_0\,(1 + 4\theta - \epsilon_0) \tag{2.29}$$

where $\theta \equiv kT/m_e c^2$ is the dimensionless electron temperature, E_0 is the initial photon energy, E_s is the scattered photon energy and $\epsilon_0 \equiv E_0/m_e c^2$. The energy dispersion

of this Gaussian is given by

$$\sigma = \epsilon_0 \left[2\theta + \frac{2}{5}\epsilon_0^2 \right]^{1/2} \tag{2.30}$$

As shown by Ross & Fabian (1993), this treatment describes adequately the down-scattering of photons of energy less than $\sim$ 200 keV. This approximation is also discussed by Ross et al. (1978).

Therefore, the mean intensity after one scattering is found with the convolution of the unscattered intensity $J(E')$

$$J'(E) = \frac{1}{\sigma_{kn}(E)} \int dE' J(E') P(E', E) \tag{2.31}$$

where

$$\sigma_{kn}(E) = \sigma_T \frac{3}{4} \left[\frac{1+x}{x^3} \left\{ \frac{2x(1+x)}{1+2x} - \ln(1+2x) \right\} + \frac{1}{2x} \ln(1+2x) - \frac{1+3x}{(1+2x)^2} \right] \tag{2.32}$$

(with $x \equiv E/m_e c^2$), is the *Klein-Nishina* cross-section, which represents the reduction of the classical value (Thomson), as the photon energy becomes large (Rybicki & Lightman, 1979).

We compute the Comptonized spectrum following this approximation, taking the same black body source function used in LLR (at $\theta = 0.02$), in order to compare the behavior of both solutions. In Figure (2.3) we plot the emergent spectrum after 50, 500 and 5000 scatterings, compared with the original spectrum $I_{bb}(x)$. We can see that the photons at large x (high energies) are scattered in a similar way to the LLR result. However, using the Gaussian approximation it is very difficult to reproduce the power law $x^{1/2}$ at low energies. Only after 5000 iterations (scatterings), does this part of the resulting spectrum show Comptonization. It is clear that many iterations are necessary to reproduce the LLR results with the Gaussian approximation. This is expected, because the fractional energy change after n scatterings, for $\theta \ll 1$, is about

$$\frac{E}{E_0} \simeq (1 - \epsilon_0)^n \tag{2.33}$$

and therefore $n \simeq \ln(\Delta E/E)/\epsilon_0$. If $\ln(\Delta E/E)$ is of the order of unity, then the number of scatterings is of the order of the inverse of energy, i.e., $n \sim \epsilon_0^{-1}$ (note $\epsilon_0 = x$). Then we see that for $x \simeq 1$, the number of scatterings is of the order of 1; but for low energies, if $x \simeq 0.001$ then $n \sim 10^3$, as can be observed in Figure (2.3). However, since we are interested in the effect of the Comptonization at high energies, especially in the region close to the Kα iron lines ($\simeq 6.4$ keV), we see that for about ~ 50 scatterings this technique provides a reasonably accurate solution.

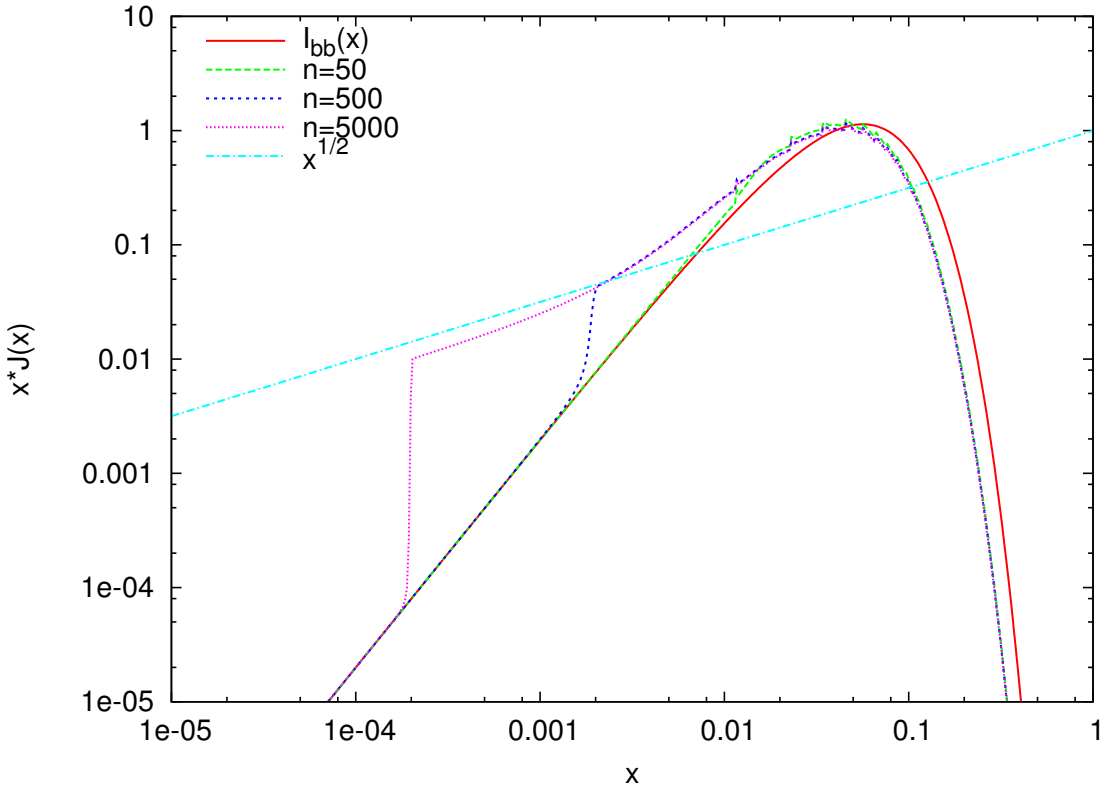

Figure 2.3 Emergent spectra after 50, 500 and 5000 scatterings. The black body $I_{bb}(x)$ (in red) is assumed to be the same that LLR. We also show the power law $x^{1/2}$ for low energies.

2.3 Radiative Transfer

In this section we discuss some of the basic ideas regarding the transport of radiation in a gaseous medium. In particular, we will follow the formalism known as the Feautrier method, described in Mihalas (1978), which describes how the equations must be discretized to perform numerical solutions and the application of boundary conditions to describe the physics of a particular problem. We also discuss the treatment developed by Chandrasekhar (1960) for isotropic scattering in the conservative case, which emphasizes the formal nature and solution of the transport equations. We also show comparisons of numerical and analytic solutions in some special cases.

2.3.1 The interaction of radiation with matter

If a beam of radiation passes through matter, energy may be added or subtracted from it by emission or absorption, and the intensity will not, in general, remain constant. Scattering of photons into and out of the beam can also affect the intensity. Therefore, if we are interested studying the interaction of radiation with matter, we need to distinguish between scattering and *true* absorption-emission processes.

Scattering processes

The scattering processes occur when a photon interacts with a scattering center (perhaps with a change in the internal excitation state), and emerges from the interaction with a slightly altered energy. This process depends mostly on the radiation field and has a weak connection with the local physics of the material.

Examples of scattering of photons by a free electron are: Thomson scattering, which is the result of a free charge oscillating in the electromagnetic field of the radiation; and the Compton scattering, given by a collision of the photon with the free particle (electron). Similarly, atoms are centers of the Rayleigh scattering, which can be viewed as a resonance of a permitted oscillation of the bound system with the field.

Absorption-Emission processes

The absorption processes occur when the photon is destroyed by conversion of its energy into thermal energy of the gas, i.e., the photon is thermalized. Since the photon energy goes directly into the thermal kinetic energy of the gas, absorption is coupled with the local thermodynamics of the material.

Conversely, the thermal emission transfers energy from the thermal pool of the gas directly to the radiation field. Therefore, combination of thermal absorption and emission produces a local equilibrium between the radiation and the material, while the scattering processes allow photons to move from one part to another in the atmosphere independently of the local conditions, introducing alterations to the equilibrium gas-radiation.

Thermal absorption and emission are inverse processes, for which corresponding examples are: Bound-free absorption or photoionization (electron escapes), with radiative recombination (electron is captured); free-free absorption (electron kinetic energy is altered), with the emission of a photon (bremsstrahlung); bound-bound absorption or photoexcitation (electron goes to a higher state), with spontaneous decay or stimulated de-excitation; collisional excitation, with collisional de-excitation; and collisional ionization (of the excited atom into the continuum), with the inverse given by three-body collisional recombination.

Extinction coefficient

An element of material, of cross-section dS and length ds, removes from a beam of radiation with specific intensity $I(\mathbf{r}, \mathbf{n}, \nu, t)$, incident in the normal $\mathbf{n}$ to dS, at a position $\mathbf{r}$, and propagating into a solid angle $d\omega$, an amount of energy

$$\delta E = \chi(\mathbf{r}, \mathbf{n}, \nu, t) I(\mathbf{r}, \mathbf{n}, \nu, t) dS ds d\omega d\nu dt \tag{2.34}$$

within a frequency band $d\nu$ in a time t. The quantity $\chi(\mathbf{r}, \mathbf{n}, \nu, t)$ is called the extinction coefficient, or opacity, and has units of inverse length. Its inverse gives a measure of the distance that the photon can propagate before being removed from the beam

(photon mean-free path).

In local thermodynamic equilibrium (LTE) and static atmospheres, the total extinction is assumed to be linear in the form

$$\chi(\mathbf{r},\nu,t) = \kappa(\mathbf{r},\nu,t) + \sigma(\mathbf{r},\nu,t) \tag{2.35}$$

where the two volume coefficients $\kappa(\mathbf{r},\nu,t)$ and $\sigma(\mathbf{r},\nu,t)$ describe the rate at which energy is removed from the beam by true absorption and scattering, respectively.

Emission coefficient

The amount of energy released from an element of material of cross-section dS and length ds, into a solid angle $d\omega$, within a frequency band $d\nu$, in a normal direction $\mathbf{n}$ in a time interval dt, is

$$\delta E = \eta(\mathbf{r},\mathbf{n},\nu,t) dS ds d\omega d\nu dt \tag{2.36}$$

where $\eta(\mathbf{r},\mathbf{n},\nu,t)$ is called the emission coefficient, in units of erg cm^{-3} sr^{-1} Hz^{-1} s^{-1}. In a steady-state and thermal equilibrium, the material is at constant temperature and the radiation field is homogeneous and isotropic. Therefore there is no net gain or loss of energy by the matter, and the emission coefficient is given by

$$\eta(\nu) = \kappa(\nu) I(\mathbf{n},\nu) \tag{2.37}$$

which is known as the *Kirchhoff's law*. For a gas in strict thermal equilibrium at a temperature T, the intensity I is given by the Planck function, so we get the *Planck-Kirchhoff* relation:

$$\eta^*(\nu) = \kappa(\nu) B_\nu(T) \tag{2.38}$$

2.3.2 Derivation of the Transfer Equation

Consider a parcel of gas located at $\mathbf{r}$ with size $\Delta\mathbf{r}$ and its effect on incident radiation. The difference between the amount of energy that emerges at a position $\mathbf{r} + \Delta\mathbf{r}$ at

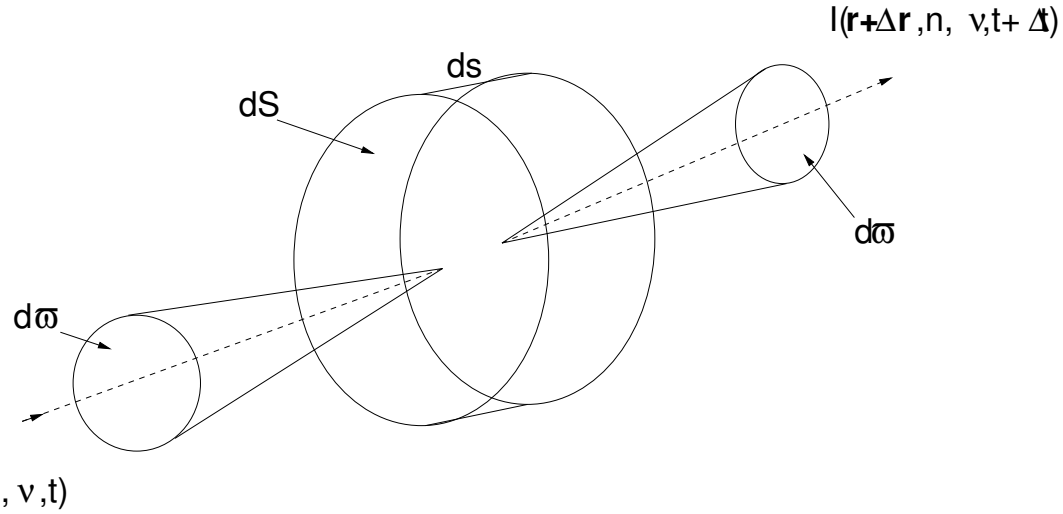

Figure 2.4 Element of absorbing and emitting material considered in derivation of transfer equation.

time $t + \Delta t$, and the incident at $\mathbf{r}$ and t; must be equal to the amount of energy created by the material in the volume minus the amount absorbed (see Figure 2.4):

$$\begin{aligned}&[I(\mathbf{r} + \boldsymbol{\Delta}\mathbf{r}, \mathbf{n}, \nu, t + \Delta t) - I(\mathbf{r}, \mathbf{n}, \nu, t)]\, dS d\omega d\nu dt \\ &\qquad = [\eta(\mathbf{r}, \mathbf{n}, \nu, t) - \chi(\mathbf{r}, \mathbf{n}, \nu, t) I(\mathbf{r}, \mathbf{n}, \nu, t)]\, ds dS d\omega d\nu dt\end{aligned} \tag{2.39}$$

Denoting s as the path-length, then $\Delta t = \Delta s/c$. Also, the final radiation field after $\boldsymbol{\Delta}\mathbf{r}$ and Δt is equal to the initial one plus its differential along the path-length

$$I(\mathbf{r} + \boldsymbol{\Delta}\mathbf{r}, \mathbf{n}, \nu, t + \Delta t) = I(\mathbf{r}, \mathbf{n}, \nu, t) + d\left[I(\mathbf{r}, \mathbf{n}, \nu, t)\right] \tag{2.40}$$

The total differential must be taken assuming that the independent variable is t, which depends on s, thus

$$d\left[I(\mathbf{r}, \mathbf{n}, \nu, t)\right] = \frac{\partial I}{\partial t}\Delta t + \frac{\partial I}{\partial s}\Delta s \tag{2.41}$$

However, $\Delta t = \frac{\Delta s}{c}$, then

$$d\left[I(\mathbf{r}, \mathbf{n}, \nu, t)\right] = \frac{\partial I}{\partial t}\frac{ds}{c} + \frac{\partial I}{\partial s}\Delta s \tag{2.42}$$

and we get,

$$I(\mathbf{r}+\boldsymbol{\Delta}\mathbf{r},\mathbf{n},\nu,t+\Delta t) = I(\mathbf{r},\mathbf{n},\nu,t) + \left[\frac{1}{c}\frac{\partial I}{\partial t} + \frac{\partial I}{\partial s}\right] ds \tag{2.43}$$

Combining equation (2.39) with (2.43), we obtain the transfer equation:

$$\left[\frac{1}{c}\frac{\partial}{\partial t} + \frac{\partial}{\partial s}\right] I(\mathbf{r},\mathbf{n},\nu,t) = \eta(\mathbf{r},\mathbf{n},\nu,t) - \chi(\mathbf{r},\mathbf{n},\nu,t) I(\mathbf{r},\mathbf{n},\nu,t) \tag{2.44}$$

Writing the derivative on s in Cartesian coordinates,

$$\frac{\partial I}{\partial s} = \left(\frac{\partial x}{\partial s}\right)\left(\frac{\partial I}{\partial x}\right) + \left(\frac{\partial y}{\partial s}\right)\left(\frac{\partial I}{\partial y}\right) + \left(\frac{\partial z}{\partial s}\right)\left(\frac{\partial I}{\partial z}\right) \tag{2.45}$$

or

$$\frac{\partial I}{\partial s} = n_x\left(\frac{\partial I}{\partial x}\right) + n_y\left(\frac{\partial I}{\partial y}\right) + n_z\left(\frac{\partial I}{\partial z}\right) \tag{2.46}$$

where n_x, n_y and n_z are the components of $\mathbf{n}$, the equation (2.44) becomes

$$\left[\frac{1}{c}\frac{\partial}{\partial t} + \mathbf{n}\cdot\nabla\right] I(\mathbf{r},\mathbf{n},\nu,t) = \eta(\mathbf{r},\mathbf{n},\nu,t) - \chi(\mathbf{r},\mathbf{n},\nu,t) I(\mathbf{r},\mathbf{n},\nu,t) \tag{2.47}$$

For the one-dimensional case, choosing the z-direction, and with $n_z = \frac{dz}{ds} = \cos\theta \equiv \mu$, the time-independent form is given by

$$\mu\frac{\partial}{\partial z} I(z,\mathbf{n},\nu) = \eta(z,\mathbf{n},\nu) - \chi(z,\mathbf{n},\nu) I(z,\mathbf{n},\nu) \tag{2.48}$$

This is the standard radiation transfer equation for *plane-parallel* atmospheres.

2.3.3 Optical Depth and the Source function

Considering the planar, time-independent transfer equation, if we introduce $d\tau \equiv -\chi(z,\nu)dz$, we can define an optical depth, which is the integrated opacity of the material along the line of sight:

$$\tau(z,\nu) = \int_z^{z_{max}} \chi(z',\nu)dz' \tag{2.49}$$

Because of the negative sign τ increases inward into the atmosphere, from $\tau = 0$ at the surface where $z = z_{max}$. Then it provides an idea of how deeply the observer can

see into the material. Further, since χ^{-1} is the photon mean-path, this implies that τ gives the number of photon mean-free-paths at a frequency ν in the line of sight, from z_{max} to z.

Finally, we define the source function $S(z,\nu)$, given by the ratio of the emissivity to the opacity of the gas,

$$S(z,\nu) = \frac{\eta(z,\nu)}{\chi(z,\nu)} \tag{2.50}$$

which we introduce in (2.48) to get

$$\mu \frac{\partial I_\nu}{\partial \tau_\nu} = I_\nu - S_\nu \tag{2.51}$$

Where we suppress the explicit dependence on z and μ, and the frequency is included as a subscript. This basic equation expresses the fact that photons do not decay spontaneously, so that the intensity of the beam does not change unless photons are added or taken out from it. Therefore, without these processes, the intensity is invariant along the rays.

2.3.4 Moments of Transfer equation

The first three moments of the intensity are defined by:

$$J \equiv \frac{1}{2}\int_{-1}^{+1} I d\mu \tag{2.52}$$

$$H \equiv \frac{1}{2}\int_{-1}^{+1} \mu I d\mu \tag{2.53}$$

$$K \equiv \frac{1}{2}\int_{-1}^{+1} \mu^2 I d\mu \tag{2.54}$$

where J is the mean intensity, since is just an average of the intensity over all angles; while H and K are proportional to the flux and radiation pressure, respectively.

2.3.5 Formal solution in plane parallel geometry

If in equation (2.51) the source function is known, we see directly that we need to solve a linear first-order differential equation with constant coefficients. It is easy to show the integration factor to be $\exp(-\tau_\nu/\mu)$, so

$$\frac{\partial}{\partial \tau_\nu}\left[I_\nu e^{-\tau_\nu/\mu}\right] = \frac{1}{\mu} S_\nu e^{-\tau_\nu/\mu} \tag{2.55}$$

Integration from τ_1 to τ_2 gives:

$$I_\nu(\tau_1) = I_\nu(\tau_2) e^{-(\tau_2-\tau_1)/\mu} + \frac{1}{\mu}\int_{\tau_1}^{\tau_2} S_\nu(t) e^{-(t-\tau_1)/\mu} dt \tag{2.56}$$

In plane-parallel geometry, defining I_ν^+ and I_ν^- as the outgoing and incoming radiation fields, respectively; we can write the solution in each case:

- For $\mu \geq 0$: set $\tau_1 = \tau_\nu$, and $\tau_2 = \tau_{max}$;

$$I_\nu^+(\tau_\nu) = I_\nu^+(\tau_{max}) e^{-(\tau_{max}-\tau_\nu)/\mu} + \frac{1}{\mu}\int_{\tau_\nu}^{\tau_{max}} S_\nu(t) e^{-(t-\tau_\nu)/\mu} dt \tag{2.57}$$

- For $\mu \leq 0$: set $\tau_1 = \tau_\nu$, and $\tau_2 = 0$;

$$I_\nu^-(\tau_\nu) = I_\nu^-(0) e^{\tau_\nu/\mu} + \frac{1}{\mu}\int_{0}^{\tau_\nu} S_\nu(t) e^{-(\tau_\nu-t)/\mu} dt \tag{2.58}$$

The first term in each one of the solutions (2.57) and (2.58) is provided by the boundary conditions. We are especially interested in the case where the atmosphere is illuminated by a source from outside, in which case $I_\nu^-(0) = I_{inc}$, i.e., the incoming radiation at the top is just the incident field. The second boundary condition is specified at τ_{max}, where the outgoing radiation can be assumed to be zero in general ($I_\nu^+ = 0$), neglecting intrinsic emission; or we set $I_\nu^+ = B_\nu(T)$, for a thermal black body field produced by the gas at a temperature T. In Figure (2.5) we show a schematic view of a plane-parallel atmosphere with the two beams of radiation, depending of the angle with respect to the normal.

2.3.6 Limitng expressions for the Source function

The transfer equation (2.51) is a standard form to be used in any problem regarding interaction of radiation with matter. The only constrain so far is the geometry, i.e.,

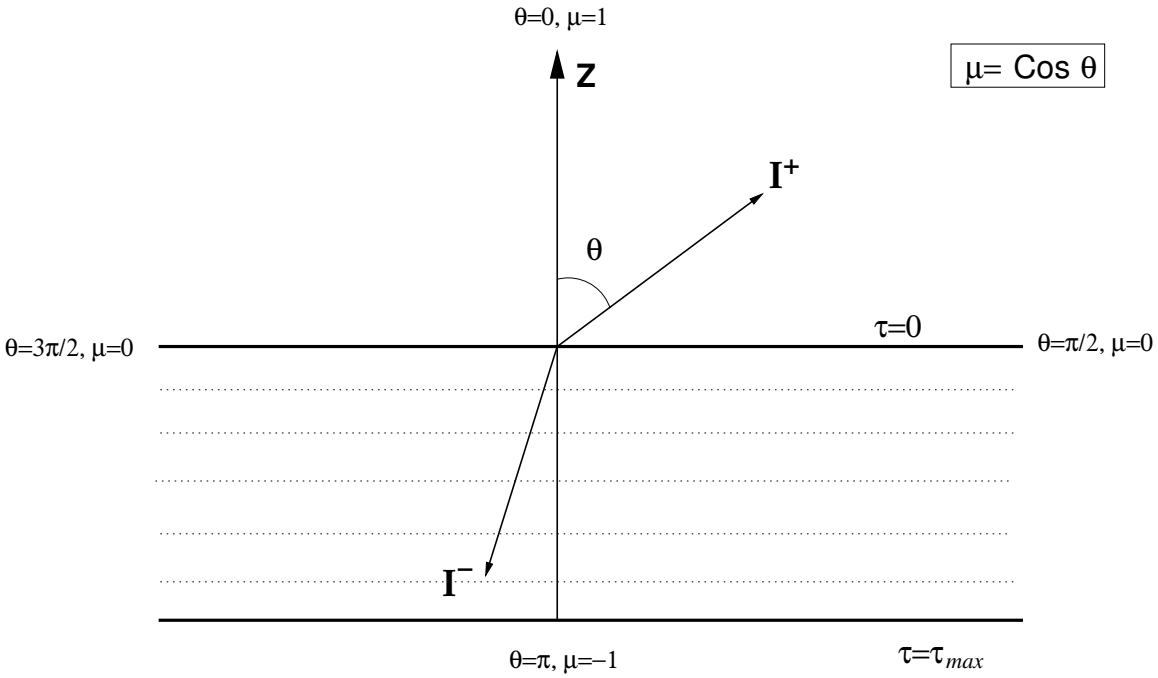

Figure 2.5 Plane-parallel slab with the incoming and outgoing radiation fields.

we write the transfer equation for the one dimensional problem in plane-parallel atmospheres, where the coordinate of importance is chosen to be in the vertical direction perpendicular to the slab.

However, the physical conditions that characterize a particular problem are introduced in two ways. First, the global properties of the desired problem are specified through the boundary conditions, in particular, to define whether the gas is illuminated from outside at the surface ($\tau = 0$), and if there is or is not emission at the inner boundary ($\tau = \tau_{max}$). This could be thermal emission due the viscosity of the gas, or radiation due a central source in the case of stellar atmospheres.

On the other hand, the physical conditions that describe the gas composing the atmosphere are introduced via the source function (2.50), and consequently by the definitions of the extinction and emission coefficients. Besides the *Planck-Kirchhoff relation* (2.38), there is an emission coefficient due to scattering in the gas. If scat-

tering is assumed coherent and isotropic, the emission coefficient can be written as

$$\eta_\nu^s = \sigma_\nu J_\nu \tag{2.59}$$

Then the total emission coefficient is $\eta_\nu = \eta_\nu^* + \eta_\nu^s$, and with (2.35) into (2.50) we obtain

$$S_\nu = \frac{\kappa_\nu B_\nu + \sigma_\nu J_\nu}{\kappa_\nu + \sigma_\nu} \tag{2.60}$$

It is customary to express the source function in this form when there is contribution from thermal absorption and emission plus a contribution from a coherent, isotropic, continuum scattering term, for example, from Thomson scattering by free electrons or from Rayleigh scattering.

If we suppose we have strict local thermodynamic equilibrium (LTE), and the scattering processes are neglected, ($\sigma_\nu = 0$), we get

$$S_\nu = B_\nu \tag{2.61}$$

Conversely, if pure isotropic scattering is assumed without intrinsic emission from the gas ($\kappa_\nu = 0$), the source function results to be

$$S_\nu = J_\nu \tag{2.62}$$

equal to the mean intensity.

It must be stressed that these forms for the source function are only *illustrative*, because they are based on very simple approximations of the physical properties of the material; nevertheless, they provide a useful way to describe the methods to solve the problem of radiation transfer under the approaches discussed in the next sections. In general, the main difficulty in the solution of real physical problems is the existence of scattering terms, which decouple the radiation field from local sources and sinks, and involve global transport of photons over large distances in the atmosphere. In particular, the expression for the emission coefficient due to scattering (2.59) is not valid in many cases since it actually depends on a *redistribution function*, which gives the joint probability that a photon will be scattered from a particular direction and

frequency. This expression is inadequate in most of the real problems where the scattering is non-isotropic and the angular dependence of η_ν^s plays an important role.

We can also see a challenge in equations (2.60) and (2.62), where the source function depends explicitly on the mean intensity J_ν, which requires the intensity to be known via (2.52). To solve this problem, we need a self-consistent approach where, starting with a guess for S_ν, one is able to calculate an estimate for the intensity and then J_ν. The result is used to recalculate a new source function and repeat the process until some accuracy is reached (typically we require that the ratio between the source function calculated in the previous iteration and the next one be equal or less than 10^{-3}). Because this requires defining the source function to describe a particular problem, the formal solution discussed in the previous sections is useless and new formalisms are required.

2.3.7 Two-point boundary value problem

Here we will derive the Feautrier approach describe in section 6.3 of Mihalas (1970). This is a very general and powerful treatment which results from writing the transfer equation as a second order differential equation plus boundary conditions at two points.

In the one-dimensional case we can separate, as before, the outgoing and incoming radiation field for $\pm\mu$, and rewrite the equation (2.48) as:

$$\mu\frac{\partial}{\partial z}I(z,+\mu,\nu) = \chi(z,\nu)\left[S(z,\nu) - I(z,+\mu,\nu)\right] \tag{2.63}$$

$$-\mu\frac{\partial}{\partial z}I(z,-\mu,\nu) = \chi(z,\nu)\left[S(z,\nu) - I(z,-\mu,\nu)\right] \tag{2.64}$$

where now the angular variable is restricted to positive values ($0 \leq \mu \leq 1$). Defining the symmetric and antisymmetric averages,

$$u(z,\mu,\nu) \equiv \frac{1}{2}\left[I(z,\mu,\nu) + I(z,-\mu,\nu)\right] \tag{2.65}$$

$$v(z,\mu,\nu) \equiv \frac{1}{2}\left[I(z,\mu,\nu) + I(z,-\mu,\nu)\right] \tag{2.66}$$

or in short form $u = \frac{1}{2}\left(I_\nu^+ + I_\nu^-\right)$ and $v = \frac{1}{2}\left(I_\nu^+ - I_\nu^-\right)$. Adding (2.63) and (2.64)

$$\mu\left[\frac{\partial I^+}{\partial z} - \frac{\partial I^-}{\partial z}\right] = \chi S - \chi I^+ + \chi S - \chi I^- \tag{2.67}$$

$$\mu\left[\frac{\partial}{\partial z}\left(I^+ - I^-\right)\right] = \chi\left[2S - \left(I^+ + I^-\right)\right] \tag{2.68}$$

$$2\mu\frac{\partial v}{\partial z} = \chi\left(2S - 2u\right) \tag{2.69}$$

Then,

$$\mu\frac{\partial}{\partial z}v(z,\mu,\nu) = \chi(z,\nu)\left[S(z,\nu) - u(z,\mu,\nu)\right] \tag{2.70}$$

Now, subtracting (2.63) and (2.64)

$$\mu\left[\frac{\partial I^+}{\partial z} + \frac{\partial I^-}{\partial z}\right] = \chi S - \chi I^+ - \chi S + \chi I^- \tag{2.71}$$

$$\mu\frac{\partial}{\partial z}\left[I^+ + I^-\right] = -\chi\left[I^+ - I^-\right] \tag{2.72}$$

Thus,

$$\mu\frac{\partial}{\partial z}u(z,\mu,\nu) = -\chi(z,\nu)v(z,\mu,\nu) \tag{2.73}$$

Now we can substitute (2.73) into (2.70) to eliminate v

$$\mu\frac{\partial}{\partial z}\left[-\frac{\mu}{\chi}\frac{\partial u}{\partial z}\right] = \chi\left[S - u\right] \tag{2.74}$$

As before, we can define $d\tau_\nu \equiv d\tau(z,\nu) = -\chi(z,\nu)dz$, and we get

$$\mu^2\frac{\partial^2 u_{\mu\nu}}{\partial\tau_\nu^2} = u_{\mu\nu} - S_\nu \tag{2.75}$$

where we suppress the explicit dependence on τ, while the frequency and angular dependence are included as subscripts.

Boundary conditions

The equation (2.75) must be solved taking into account the boundary conditions at $\tau = 0$ and $\tau = \tau_{max}$. For an illuminated atmosphere, we set at $\tau = 0$ the incoming part to the incident field, $I(0, -\mu, \nu) = I_{inc}$. With this in (2.65) and (2.66):

$$u_{\mu\nu}(0) - v_{\mu\nu}(0) = I_{inc} \tag{2.76}$$

and from (2.73)

$$v_{\mu\nu} = \mu \frac{\partial u_{\mu\nu}}{\partial \tau_\nu} \tag{2.77}$$

Therefore, at the surface,

$$\mu \left(\frac{\partial u_{\mu\nu}}{\partial \tau \nu} \right)_0 - u_{\mu\nu}(0) = I_{inc} \tag{2.78}$$

At $\tau = \tau_{max}$ we specify $I(\tau_{max}, +\mu, \nu) = I^+$, and

$$\mu \left(\frac{\partial u_{\mu\nu}}{\partial \tau \nu} \right)_{\tau_{max}} + u_{\mu\nu}(\tau_{max}) = I^+ \tag{2.79}$$

where we can choose I^+ to be a Planck function, if we consider thermal emission by the gas, or equal to zero.

Discretization of equations

We now replace integrals by sums and derivatives by differences. The equation (2.75) will be converted into a set of differential equations via the discretization of all variables.

First, the derivatives can be expressed as (Rutten, 2003),

$$d\tau_{d+1/2} = \tau_{d+1} - \tau_d \equiv d\tau_d \tag{2.80}$$

$$d\tau_{d-1/2} = \tau_d - \tau_{d-1} \equiv d\tau_{d-1} \tag{2.81}$$

Therefore,

$$\left(\frac{du}{d\tau} \right)_{d+1/2} = \frac{u_{d+1} - u_d}{\tau_{d+1} - \tau_d} = \frac{u_{d+1} - u_d}{d\tau_d} \tag{2.82}$$

and the second derivative is

$$\left(\frac{d^2u}{d\tau^2}\right)_d = \frac{(du/d\tau)_{d+1/2} - (du/d\tau)_{d-1/2}}{1/2\left(d\tau_{d+1/2} + d\tau_{d-1/2}\right)} \tag{2.83}$$

or

$$\left(\frac{d^2u}{d\tau^2}\right)_d = \frac{2}{(d\tau_d + d\tau_{d-1})}\left[\frac{u_{d+1} - u_d}{d\tau_d} - \frac{u_d - u_{d-1}}{d\tau_{d-1}}\right] \tag{2.84}$$

$$\left(\frac{d^2u}{d\tau^2}\right)_d = 2\left[\frac{u_{d+1}}{d\tau_d\left(d\tau_d + d\tau_{d-1}\right)} - \frac{u_d}{d\tau_d d\tau_{d-1}} + \frac{u_{d-1}}{d\tau_{d-1}\left(d\tau_d + d\tau_{d-1}\right)}\right] \tag{2.85}$$

With (2.82) and (2.85), the equation (2.75) can be written as

$$-\left[\frac{2\mu^2}{d\tau_{d-1}\left(d\tau_d + d\tau_{d-1}\right)}\right]u_{d-1} + \left[\frac{2\mu^2}{d\tau_d d\tau_{d-1}} + 1\right]u_d - \left[\frac{2\mu^2}{d\tau_d\left(d\tau_d + d\tau_{d-1}\right)}\right]u_{d+1} = S_d \tag{2.86}$$

or in short form:

$$-\mathbf{A}u_{d-1} + \mathbf{B}u_d - \mathbf{C}u_{d+1} = \mathbf{S} \qquad (d = 1, 2, ..., D-1) \tag{2.87}$$

Where $\mathbf{A}$, $\mathbf{B}$, $\mathbf{C}$ and $\mathbf{S}$ are $D \times D$ matrices, which elements are given by the terms inside the brackets, and D is the total number of grid points in τ. Obviously, the elements of $\mathbf{S}$ are given by the source function evaluated at each τ. At the surface $d = 1$, then we can rewrite the boundary condition (2.78), using (2.82) as

$$\mu\left(\frac{u_2 - u_1}{d\tau_1}\right) - u_1 = I_{inc} \tag{2.88}$$

Doing the same, at τ_{max} $d = D - 1$, then condition (2.79) becomes

$$\mu\left(\frac{u_D - u_{D-1}}{d\tau_{D-1}}\right) - u_D = I^+ \tag{2.89}$$

Forward-backward solution

The numerical solution in this approach proceeds by a forward elimination plus backward substitution scheme. We start using the boundary condition at the surface to express u_1 in u_2. The result is used to insert in the equation between u_1, u_2 and u_3 to

express u_2 in terms of u_3. Following in the same way we can express each u_d in terms of u_{d+1}. We finally reach the last point in the grid, and the boundary condition for τ_{max} delivers u_D. Back substitutions then produce $u_D \rightarrow u_{D-1} \rightarrow u_{D-2} \rightarrow \cdots \rightarrow u_2 \rightarrow u_1$, so all u_d are known.

In figure (2.6) we plot the numerical results for the symmetric average $u(0, \nu)$ (at the surface), using the Feautrier method (in blue), compared with the resulting from the formal solutions (2.57) and (2.58) into $u = \frac{1}{2}(I^+ + I^-)$ (in red); as a function of the energy. In both calculations we assume the source function to be constant, so we set $S = F_{inc}$, the incident flux.

The boundary conditions include the constant flux $F_{inc} \approx 10^{15}$ erg s^{-1} cm^{-2} at the surface ($\tau = 0$), and a thermal black body emission at $\tau = \tau_{max}$. The temperature of the Plack function is set at a typical value of $T = 1.21 \times 10^5$ K, or $kT = 10.4$ eV, where k is the Boltzmann's constant. This temperature corresponds to an intrinsic flux from the atmosphere of $F_{int} \approx 10^{16}$ erg s^{-1} cm^{-2}; however, both incident and intrinsic fluxes are normalized, so the units in the plot are arbitrary.

Although this example does not represent any real physical problem, we use it in order to test the algebraic development of the Feautrier method, and it is evident that both symmetric average solutions are in good agreement (with differences smaller than 0.1%), which tells us that the discretization assumed before does not reduce the accuracy of the results.

The same agreement can be seen in Figure (2.7), where we show the mean intensity $J(\tau)$, calculated from the symmetric average as

$$J(\tau) = \int_0^1 u(\tau, \mu) d\mu \tag{2.90}$$

for both Feautrier method and the formal solution.

2.3.8 Eddington factors approach

In some problems the number of frequencies can be large because we must satisfy the condition for radiative equilibrium, or statistical equilibrium in several transitions;

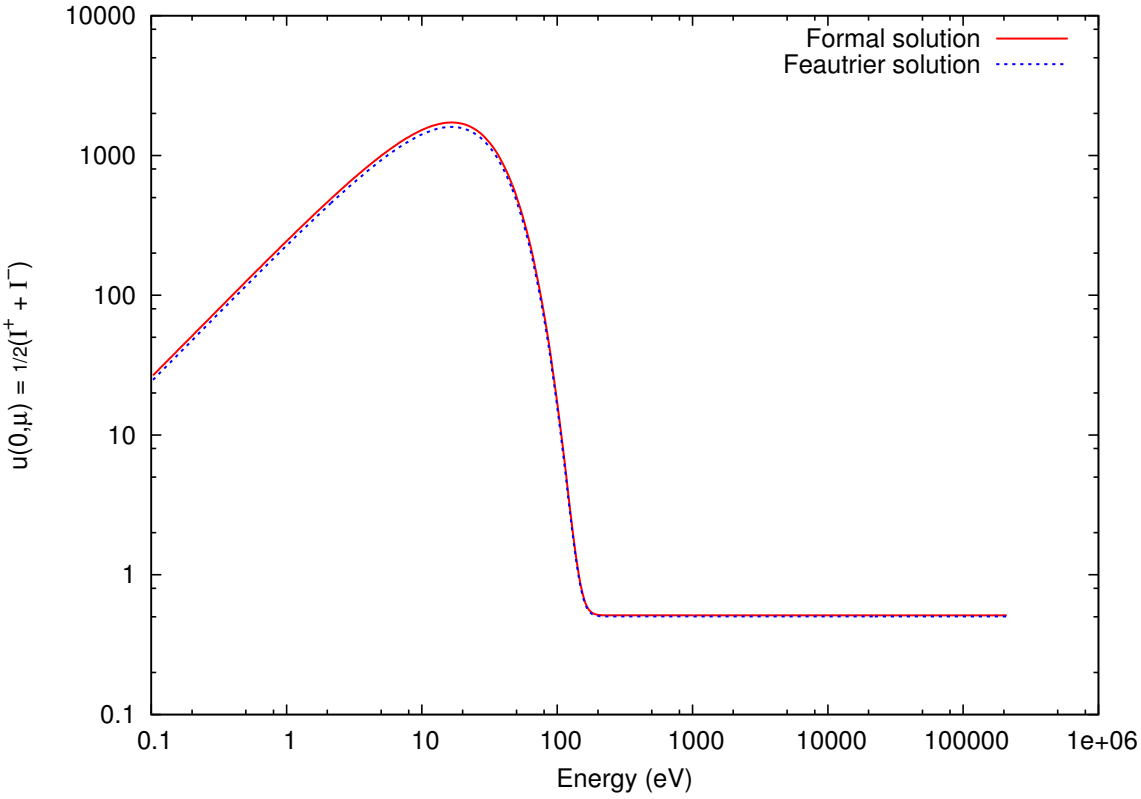

Figure 2.6 Comparison between the formal solution and the Feautrier method.

but the angular information is essentially unnecessary because only J_ν not $u_{\mu\nu}$ enters these constraints. We therefore eliminate the angular information by introducing variable Eddington factors $f_\nu = K_\nu/J_\nu$ (Auer & Mihalas, 1970).

To do this, we start by integration of the differential equation (2.75) over all angles μ,

$$\int_0^1 \mu^2 \frac{\partial^2 u_{\mu\nu}}{\partial \tau_\nu^2} d\mu = \int_0^1 u_{\mu\nu} d\mu - S_\nu \int_0^1 d\mu \qquad (2.91)$$

Since the differentiation is in τ and the integration over μ, we can interchange the order

$$\frac{\partial^2}{\partial \tau_\nu^2} \int_0^1 \mu^2 u_{\mu\nu} d\mu = \int_0^1 u_{\mu\nu} d\mu - S_\nu \int_0^1 d\mu \qquad (2.92)$$

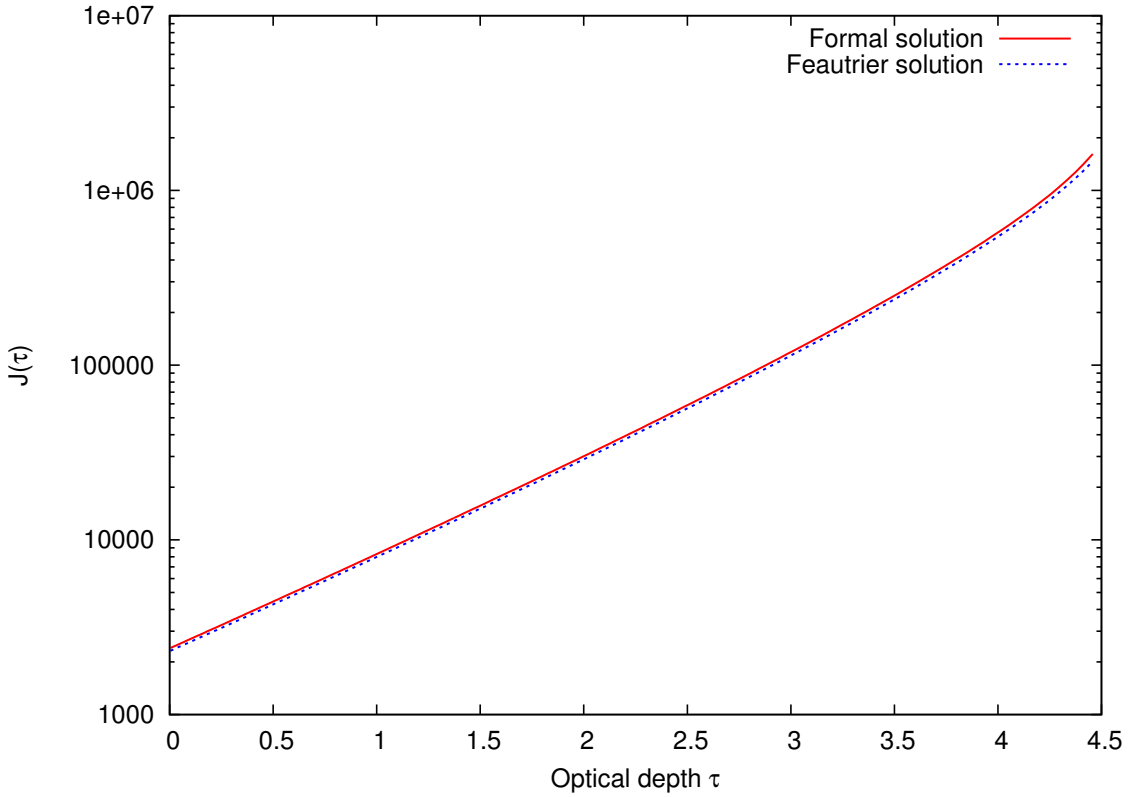

Figure 2.7 First moment $J(\tau)$ of the intensity calculated with the Feautrier method and the formal solution.

From definitions (2.52), (2.54) and (2.65) we see that

$$\frac{\partial^2 K_\nu}{\partial \tau_\nu^2} = J_\nu - S_\nu \tag{2.93}$$

or introducing the Eddington factor with $K_\nu = f_\nu J_\nu$:

$$\frac{\partial^2 \left(f_\nu J_\nu\right)}{\partial \tau_\nu^2} = J_\nu - S_\nu \tag{2.94}$$

The boundary conditions are found in a similar way. At the surface we use (2.78), multiply by μ, and integration gives:

$$\left[\frac{\partial \left(f_\nu J_\nu\right)}{\partial \tau_\nu}\right]_0 - h_\nu J_\nu(0) = I_{inc} \tag{2.95}$$

where $h_\nu = H_\nu(0)/J_\nu(0)$. Now, at τ_{max}, doing the same into (2.79)

$$\left[\frac{\partial\left(f_\nu J_\nu\right)}{\partial\tau_\nu}\right]_{\tau_{max}} + h_\nu^\dagger J_\nu(\tau_{max}) = I^+ \tag{2.96}$$

with $h_\nu^\dagger = H_\nu(\tau_{max})/J_\nu(\tau_{max})$.

Special case: one angle solution

Since the Feautrier method described in the previous sections involves the discretization of the differentials as differences, we are interested in evaluating the accuracy of the results. A possibility is to compare the results with the analytic solution, which is exact, if we assume the source function, S_ν, is known. We take the case of isotropic scattering, assuming $S_\nu = J_\nu$, in the limit of just one angle.

In this case,

$$J_\nu = \int_0^1 u_\nu d\mu \quad \rightarrow \quad J_\nu = u_\nu \tag{2.97}$$

Setting $S_\nu = J_\nu$, the transfer equation (2.75) becomes

$$\mu^2 \frac{\partial^2 u_\nu}{\partial\tau_\nu^2} = u_\nu - J_\nu \tag{2.98}$$

but because of (2.97)

$$\mu^2 \frac{\partial^2 u_\nu}{\partial\tau_\nu^2} = 0 \tag{2.99}$$

which solution is simply given by

$$u(\tau) = C_1 + C_2\tau \tag{2.100}$$

where C_1 and C_2 are the integration constants provided by the boundary conditions. First, we note that from the definitions of u and v (equations 2.65 and 2.66):

$$u - v = I^- \quad ; \quad v = \mu\frac{\partial u}{\partial\tau} \tag{2.101}$$

so

$$\rightarrow u - \mu\frac{\partial u}{\partial\tau} = I^- \tag{2.102}$$

Also,

$$u + v = I^+ \quad \rightarrow \quad u + \mu \frac{\partial u}{\partial \tau} = I^+ \tag{2.103}$$

And from the general solution (2.99)

$$\frac{\partial u}{\partial \tau} = C_2 \tag{2.104}$$

Then, applying the boundary conditions, at $\tau = 0 \rightarrow I^- = I_{inc}$, and

$$u(0) - \mu \left(\frac{\partial u}{\partial \tau} \right)_0 = I_{inc} \tag{2.105}$$

but from the solution $u(0) = C_1$; then

$$C_1 - \mu C_2 = I_{inc} \tag{2.106}$$

At $\tau = \tau_{max} \rightarrow I^+ = I_{bb}$ (black body emission) and

$$u(\tau_{max}) + \mu \left(\frac{\partial u}{\partial \tau} \right)_{\tau_{max}} = I_{bb} \tag{2.107}$$

Again from the general solution $u(\tau_{max}) = C_1 + C_2 \tau_{max}$; then

$$C_1 = I_{bb} - C_2 \left(\tau_{max} + \mu \right) \tag{2.108}$$

Therefore the constants are

$$C_2 = \frac{I_{bb} - I_{inc}}{\tau_{max} + 2\mu} \tag{2.109}$$

$$C_1 = I_{bb} - \left[\left(I_{bb} - I_{inc} \right) \left(\frac{\tau_{max} + \mu}{\tau_{max} + 2\mu} \right) \right] \tag{2.110}$$

Thus the final solution is

$$u(\tau) = \left(\frac{I_{bb} - I_{inc}}{\tau_{max} + 2\mu} \right) \left[\tau - (\tau_{max} + \mu) \right] + I_{bb} \tag{2.111}$$

In Figure (2.8) the plot in red is the solution (2.111) calculated for a constant and arbitrary incident radiation field illuminating the surface of the slab, and an intrinsic thermal emission at τ_{max} as a black body. When we perform the same calculation with the Feautrier method, we assume at the first step that $J \propto I_{inc}$, and the result (in

blue) is the right-most curve at the bottom. Next, we recalculate the mean intensity with (2.97). This new J is inserted again into the source function (simply $S = J$) to get a new u. This procedure is called *lambda iteration*. We repeat this procedure several times until about 30 iterations, where we can see from the plot both solutions converge. This simple test shows that the Feautrier method can be used in a plane-parallel problem with the right boundary conditions, and gives an idea of how many iterations we need to get accurate results.

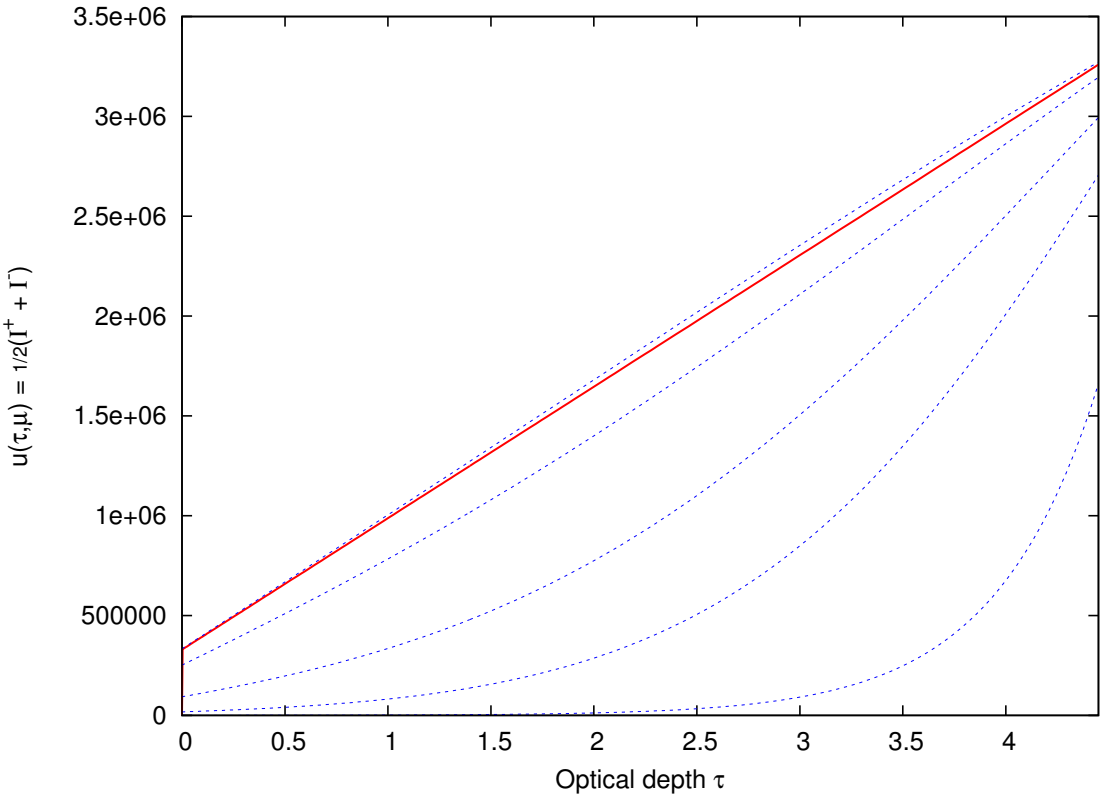

Figure 2.8 Exact solution for $u(0, \mu)$ at the surface for one angle (red), and with the Feautrier method (blue), after different number of iterations. The curves are, from the right-bottom to left-top, the corresponding for 1, 5, 10, 20 and 30 iterations.

2.3.9 The Chandrasekhar solution

This method is described in Chapter 3 of Chandrasekhar (1960), which presents in a simple context the possibility to obtain the solutions to the transfer equation, generally, in the nth approximation; expressing the angular distribution of the emergent radiation in closed form.

Isotropic scattering. Law of diffuse reflection in the conservative case

Returning to the standard form for the radiation transfer equation for a plane-parallel geometry

$$\mu \frac{dI(\tau,\mu)}{d\tau} = I(\tau,\mu) - S(\tau,\mu) \tag{2.112}$$

In the case of isotropic scattering for an illuminated atmosphere, the source function can be written as

$$S(\tau,\mu) = \frac{1}{2}\omega_0 \int_{-1}^{+1} I(\tau,\mu')d\mu' - \frac{1}{4}\omega_0 F e^{-\tau/\mu_0} \tag{2.113}$$

where F is the incident flux in the direction $-\mu_0$ and ω_0 is the fraction of radiation that is scattered (as opposed to absorbed), and is called the *single scattering albedo*. In the conservative case $\omega_0 = 1$, thus the equation of transfer is

$$\mu \frac{dI(\tau,\mu)}{d\tau} = I(\tau,\mu) - \frac{1}{2}\int_{-1}^{+1} I(\tau,\mu')d\mu' - \frac{1}{4}F e^{-\tau/\mu_0} \tag{2.114}$$

which can be expressed by a system of $2n$ linear differential equations,

$$\mu_i \frac{dI_i}{d\tau} = I_i - \frac{1}{2}\sum_j a_j I_j - \frac{1}{4}F e^{-\tau/\mu_0} \tag{2.115}$$

Here we used the fact that if any function $f(\mu)$ is a polynomial of degree $2m-1$, then

$$\int_{-1}^{+1} f(\mu)d\mu = \sum_{j=1}^{m} a_j f(\mu_j) \tag{2.116}$$

where $\mu_1, \ldots, \mu_m$ are the zeros of the Legendre polynomial P_m, and the a_j are the corresponding Gaussian weights given by

$$a_j = \frac{1}{P'_m(\mu_j)} \int_{-1}^{+1} \frac{P_m(\mu)}{\mu - \mu_j} d\mu \tag{2.117}$$

To solve the system (2.115) first we need to find the solution of the associated homogeneous equations,

$$\mu_i \frac{dI_i}{d\tau} = I_i - \frac{1}{2}\sum_j a_j I_j \tag{2.118}$$

We start with a solution of the form

$$I_i = g_i e^{-k\tau} \qquad (i = \pm 1, \ldots, \pm n) \tag{2.119}$$

where g_i and k are constants to specify. Inserting (2.119) in (2.115)

$$-\mu_i k g_i = g_i - \frac{1}{2}\sum_j a_j g_j \tag{2.120}$$

$$g_i\,(1 + \mu_i k) = \frac{1}{2}\sum_j a_j g_j \tag{2.121}$$

Then,

$$g_i = \frac{\frac{1}{2}\sum_j a_j g_j}{1 + \mu_i k} \equiv \frac{\text{constant}}{1 + \mu_i k} \tag{2.122}$$

We can see that the constant in the numerator is independent of i; then with this back into (2.121), we found the recursion relation:

$$1 = \frac{1}{2}\sum_j \frac{a_j}{1 + \mu_j k} \tag{2.123}$$

or more explicitly

$$\begin{aligned} 1 = {} & \frac{1}{2}\left[\frac{a_{-n}}{1 + \mu_{-n}k} + \frac{a_{-n+1}}{1 + \mu_{-n+1}k}\right] + \ldots \\ & + \frac{1}{2}\left[\frac{a_{-1}}{1 + \mu_{-1}k} + \frac{a_1}{1 + \mu_1 k}\right] + \ldots \\ & + \frac{1}{2}\left[\frac{a_{n-1}}{1 + \mu_{n-1}k} + \frac{a_n}{1 + \mu_n k}\right] \end{aligned} \tag{2.124}$$

However, $a_{-j} = a_j$ and $\mu_{-j} = -\mu_j$, therefore each pair of terms for $\pm n$ will result in

$$\frac{a_{-n}}{1 + \mu_{-n}k} + \frac{a_n}{1 + \mu_n k} = \frac{a_n}{1 - \mu_n k} + \frac{a_n}{1 + \mu_n k} = \frac{2a_j}{1 - \mu_j^2 k^2} \tag{2.125}$$

Then the recursion relation becomes

$$1 = \sum_{j=1}^{n} \frac{a_j}{1 - \mu_j^2 k^2} \tag{2.126}$$

This characteristic equation admits $2n$ distinct roots, which must occur in pairs as

$$\pm k_\alpha \quad (\alpha = 1, \ldots, n) \tag{2.127}$$

and because the Gaussian weights are normalized, $\sum_{j=1}^{n} a_j = 1$, then the roots for one α, say $\alpha = n$, are zero ($k_n^2 = 0$). Therefore the solution for the homogeneous system is

$$I_i = \frac{\text{constant}}{1 \pm \mu_i k_\alpha} e^{\mp k_\alpha \tau} \quad (i = \pm 1, \ldots, \pm n) \text{ and } (\alpha = 1, \ldots, \text{n}) \tag{2.128}$$

As a boundary condition, we require that none of the I_i's increase more rapidly than e^τ as $\tau \to \infty$, which implies that in the general solution (2.128) we omit the terms in $e^{+k_\alpha \tau}$. To complete the general solution of the system, we need to find the particular integral, for which we set

$$I_i = \frac{1}{4} F h_i e^{\tau/\mu_0} \tag{2.129}$$

where h_i are constants unspecified for the moment. Inserting (2.129) into (2.115)

$$-\frac{\mu}{\mu_0} h_i = h_i - \frac{1}{2} \sum_j a_j h_j - 1 \tag{2.130}$$

$$h_i \left(\frac{\mu}{\mu_0} + 1 \right) = \frac{1}{2} \sum_j a_j h_j + 1 \tag{2.131}$$

so

$$h_i = \frac{\gamma}{1 + \mu_i/\mu_0} \tag{2.132}$$

where γ is a constant independent of the index i. The recursion relation in this case will be

$$\gamma = \frac{1}{2} \gamma \sum_j \frac{a_j}{1 + \mu_j/\mu_0} + 1 \tag{2.133}$$

Hence, solving for γ and with the same conditions for the sum over the negative indices

$$\gamma = \frac{1}{1 - \sum_{j=1}^{n} a_j / \left(1 - \mu_j^2/\mu_0^2\right)} \tag{2.134}$$

Finally, the general solution to the system (2.115) can be expressed as

$$I_i = \frac{1}{4} F \left[\sum_{\alpha=1}^{n-1} \frac{L_\alpha e^{-k_\alpha \tau}}{1 + \mu_i k_\alpha} + L_n + \frac{\gamma e^{-\tau/\mu_0}}{1 + \mu_i/\mu_0} \right] \qquad (i = \pm 1, \ldots, \pm n) \tag{2.135}$$

Where the constants $L_\alpha (\alpha = 1, \ldots, n)$ are to be found from the boundary conditions. Because the form that we assumed for the source function in (2.113), the boundary condition at the top ($\tau = 0$) now must be taken as $I_{-i} = 0$, then

$$\sum_{\alpha=1}^{n-1} \frac{L_\alpha}{1 - \mu_i k_\alpha} + L_n + \frac{\gamma}{1 - \mu_i/\mu_0} = 0 \qquad (i = 1, \ldots, n) \tag{2.136}$$

is the equation we will use to determine the constants of integration. Further, inserting the solution (2.135) in the source function

$$S(\tau, \mu) = \frac{F}{8} \left[\sum_{\alpha=1}^{n-1} L_\alpha e^{-k_\alpha \tau} \sum_j \frac{a_j}{1 + \mu_j k_\alpha} + L_n \sum_j \frac{a_j}{1 + \mu_j k_\alpha} + \gamma e^{-\tau/\mu_0} \sum_j \frac{a_j}{1 + \mu_j/\mu_0} \right] + \frac{F}{4} e^{-\tau/\mu_0} \tag{2.137}$$

From (2.123) and (2.133) we see that

$$\sum_j \frac{a_j}{1 + \mu_j k_\alpha} = 2 \quad \text{and} \quad \gamma \sum_j \frac{a_j}{1 + \mu_j/\mu_0} = 2(\gamma - 1) \tag{2.138}$$

Therefore

$$S(\tau, \mu) = \frac{F}{4} \left[\sum_{\alpha=1}^{n-1} L_\alpha e^{-k_\alpha \tau} + L_n + \gamma e^{\tau/\mu_0} \right] \tag{2.139}$$

The formal solution for the outgoing radiation (2.57), in the limit $\tau_{max} \to \infty$ is

$$I(\tau, +\mu) = \frac{1}{\mu} \int_\tau^\infty e^{-(t-\tau)/\mu} S(t) dt \tag{2.140}$$

with the source function (2.139)

$$I^+(\tau) = \frac{F}{4\mu}\left[\sum_{\alpha=1}^{n-1} L_\alpha e^{\tau/\mu}\int_\tau^\infty e^{-t\left(\frac{1}{\mu}+k_\alpha\right)}dt + L_n e^{\tau/\mu}\int_\tau^\infty e^{-t/\mu}dt + \gamma e^{\tau/\mu}\int_\tau^\infty e^{-t\left(\frac{1}{\mu}+\frac{1}{\mu_0}\right)}dt\right] \tag{2.141}$$

which results in

$$I^+(\tau) = \frac{F}{4}\left[\sum_{\alpha=1}^{n-1}\frac{L_\alpha e^{-k_\alpha\tau}}{1+\mu k_\alpha} + L_n + \frac{\gamma e^{-\tau/\mu_0}}{1+\mu/\mu_0}\right] \tag{2.142}$$

Doing the same for the incoming radiation (2.58), with the boundary condition $I^-(0) = 0$

$$I^-(\tau) = \frac{1}{\mu}\int_0^\tau e^{-(\tau-t)/\mu}S(t)dt \tag{2.143}$$

so we get

$$I^-(\tau) = \frac{F}{4}\left[\sum_{\alpha=1}^{n-1}\frac{L_\alpha}{1-\mu k_\alpha}\left(e^{-k_\alpha\tau}-e^{-\tau/\mu}\right) + L_n\left(1-e^{\tau/\mu}\right) + \frac{\gamma}{1-\mu/\mu_0}\left(e^{-\tau/\mu_0}-e^{-\tau/\mu}\right)\right] \tag{2.144}$$

It is of particular interest the form for the outgoing radiation from the surface of the atmosphere, i.e., the angular distribution of the reflected radiation at $\tau = 0$, which is given by

$$I^+(0) = \frac{F}{4}\left[\sum_{\alpha=1}^{n-1}\frac{L_\alpha}{1+k_\alpha\mu} + L_n + \frac{\gamma}{1+\mu/\mu_0}\right] \tag{2.145}$$

Now we introduce without proof the identity

$$1 - z^2\sum_{j=1}^{n}\frac{a_j}{z^2-\mu_j^2} = \frac{1}{H(z)H(-z)} \tag{2.146}$$

where the function $H(z)$ is defined as

$$H(z) = \frac{1}{\mu_1\ldots\mu_n}\frac{\prod_{j=1}^n(z+\mu_j)}{\prod_{\alpha=1}^n(1+k_\alpha z)} \tag{2.147}$$

Setting $z = \mu_0$ and with (2.134) we see that

$$\gamma = H(\mu_0)H(-\mu_0) \tag{2.148}$$

Then we can define a function

$$R(\mu) \equiv \sum_{\alpha=1}^{n-1} \frac{L_\alpha}{1-k_\alpha\mu} + L_n + \frac{H(\mu_0)H(-\mu_0)}{1-\mu/\mu_0} \tag{2.149}$$

and because the boundary condition in (2.136)

$$R(\mu_i) = 0 \qquad (i = 1, \ldots, n) \tag{2.150}$$

Next we see that

$$\left(1-\frac{\mu}{\mu_0}\right)\prod_{\alpha=1}^{n}(1-k_\alpha\mu)\,R(\mu) = \prod_{\alpha=1}^{n}\left(1-\frac{\mu}{\mu_0}\right)\left[\sum_{\alpha=1}^{n-1}L_\alpha + (1-k_\alpha\mu)\,L_n\right] + (1-k_\alpha\mu)\,H(\mu_0)H(-\mu_0) \tag{2.151}$$

is a polynomial of degree n in μ which vanishes for $\mu = \mu_i, i = 1, \ldots, n$; and then exists a relation of the form

$$R(\mu) = K\frac{(-1)^n}{\mu_1 \ldots \mu_n}\frac{\prod_{i=1}^{n}(\mu-\mu_i)}{\prod_{\alpha=1}^{n}(1-k_\alpha\mu)}\frac{1}{(1-\mu/\mu_0)} \tag{2.152}$$

where K is a constant. Using (2.147) we can rewrite it as

$$\left(1-\frac{\mu}{\mu_0}\right)R(\mu) = KH(-\mu). \tag{2.153}$$

In the limit $\mu \to \mu_0$, the last equation goes to $KH(-\mu_0)$. However, using the definition (2.149)

$$\left(1-\frac{\mu}{\mu_0}\right)R(\mu) = \left(1-\frac{\mu}{\mu_0}\right)\left[\sum_{\alpha=1}^{n-1}\frac{L_\alpha}{1-k_\alpha\mu} + L_n\right] + H(\mu_0)H(-\mu_0) \tag{2.154}$$

and then

$$\lim_{\mu\to\mu_0}\left(1-\frac{\mu}{\mu_0}\right)R(\mu) = H(\mu_0)H(-\mu_0) \tag{2.155}$$

Therefore we found the constant to be $K = H(\mu_0)$, and thus

$$R(\mu) = \frac{H(\mu_0)H(-\mu)}{1-\mu/\mu_0} \tag{2.156}$$

From (2.145), (2.148) and (2.149)

$$I^+(0) = \frac{F}{4} R(-\mu) \tag{2.157}$$

so finally the reflected intensity can be written, with (2.156)

$$I(0,\mu) = \frac{F}{4} \frac{\mu_0}{\mu + \mu_0} H(\mu) H(\mu_0) \tag{2.158}$$

This is the equation for the law of *diffuse reflection* in the conservative case (i.e., pure scattering).

The H-function

The function defined in (2.147) describes the intensity of radiation scattered by a semi-infinite medium of independent scatterers. For isotropic scattering, it can be expressed by the nonlinear integral form

$$H(\mu) = 1 + \frac{\omega_0}{2} \mu H(\mu) \int_0^1 \frac{H(\mu')}{\mu + \mu'} d\mu' \tag{2.159}$$

in the conservative case $\omega_0 = 1$, and can rewrite the last equation as

$$\frac{1}{H(\mu)} = \frac{1}{2} \int_0^1 \frac{\mu' H(\mu')}{\mu + \mu'} d\mu' \tag{2.160}$$

The numerical evaluation of this equation is described by Hiroi (1994), using the extended Simpson's rule, where the integral takes the form

$$\int_{x_0}^{x_N} f(x)dx = \frac{h}{3} \left[f_0 + 4f_1 + 2f_2 + \cdots + 2f_{N-2} + 4f_{N-1} + f_N \right] + O(N^{-4}) \tag{2.161}$$

with $x_i = x_0 + ih$, $f_i = f(x_i)$, $i = 0, 1, 2, \ldots, N$. The sampling points $(x_0, \ldots, x_N)$ for the integral can be chosen at every 0.001 of μ', with $N = 1000$, if a precision to five decimal places is desired in the H function values. The evaluation is performed iteratively until all values of H converge within a preset tolerance. The initial values for H can be estimated by the approximation (Hapke, 1981):

$$H(\mu) = \left[1 - \mu \left\{ 1 + \left(\frac{1}{2} - \mu \right) \ln \left(\frac{\mu + 1}{\mu} \right) \right\} \right]^{-1} \tag{2.162}$$

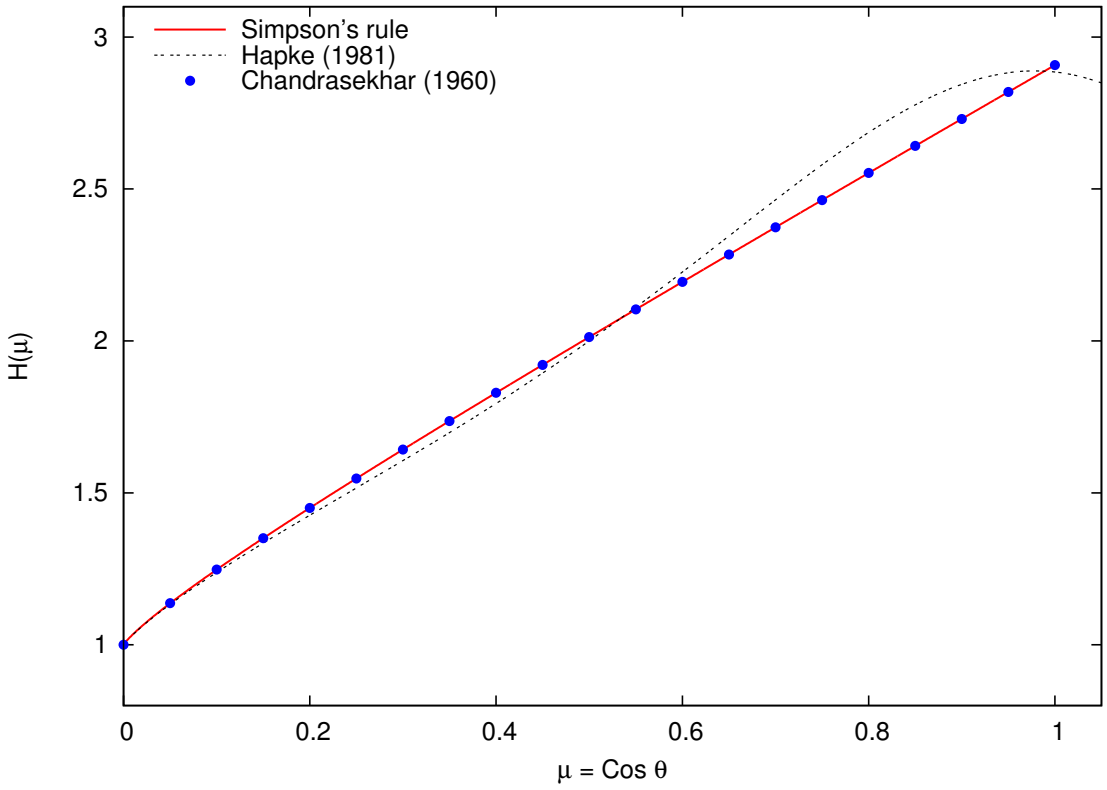

Figure 2.9 Evaluation of the $H(\mu)$ function using the Simpson's rule, compared with the Chandrasekhar (1960) results and the Hapke (1981) approximation, for the conservative case ($\omega_0 = 1$).

In the figure (2.9) we shown the result for the H function values after 100 iterations using $N = 1000$ points, the analytic form given by equation (2.162) and the tabulated values given in Chandrasekhar (1960). It is clear that is not difficult to achieve a high accuracy with this procedure. The Hapke (1981) approximation (2.162) behaves well at small angles, however the differences at angles close to 1 are greater than 10%.

One angle solution

We can compare the result given for the reflected radiation at the surface, with the exact solution in the case of one angle (Section 2.3.8). First, we note that the H

function

$$H(\mu) = \frac{1}{\mu_1 \dots \mu_n} \frac{\prod_{j=1}^{n}(\mu + \mu_j)}{\prod_{\alpha=1}^{n}(1 + k_\alpha \mu)} \tag{2.163}$$

in the case of one angle ($n = 1$) becomes

$$H(\mu) = \frac{1}{\mu_1}(\mu + \mu_1) \tag{2.164}$$

but if we choose the angle to be $\mu = \mu_1 = \mu_0$, and

$$H(\mu) = H(\mu_0) = 2 \tag{2.165}$$

Therefore the solution (2.158) for one angle is

$$I(0, \mu) = I(0, \mu_0) = \frac{F}{4}\left(\frac{1}{2}\right)[H(\mu_0)]^2 \tag{2.166}$$

$$I(0, \mu_0) = \frac{F}{2} \tag{2.167}$$

From the exact solution we know that $I^+ = u + v = u + \mu C_2$ or $I^+ = C_1 + C_2\tau + \mu C_2$, but at $\tau = 0$ we have $I^+ = C_1 + \mu C_2$. To compare with the Chandrasekhar solution we set $I_{bb} = 0$ (no thermal emission), so the coefficients are now

$$C_1 = I_{inc}\left(\frac{\tau_{max} + \mu}{\tau_{max} + 2\mu}\right) \quad \text{and} \quad C_2 = \frac{-I_{inc}}{\tau_{max} + 2\mu} \tag{2.168}$$

Therefore,

$$I(0, \mu_0) = I_{inc}\frac{\tau_{max} + \mu}{\tau_{max} + 2\mu} \tag{2.169}$$

In the limit $\tau_{max} \to \infty, I(0, \mu_0) \to I_{inc}$, thus

$$I(0, \mu_0) = \frac{F}{2} \tag{2.170}$$

and both solutions agree, as expected.

Many angles

We also compared our solution of the radiative transfer equations with the analytical approximations of Chandrasekhar in the pure scattering case with many angles. In

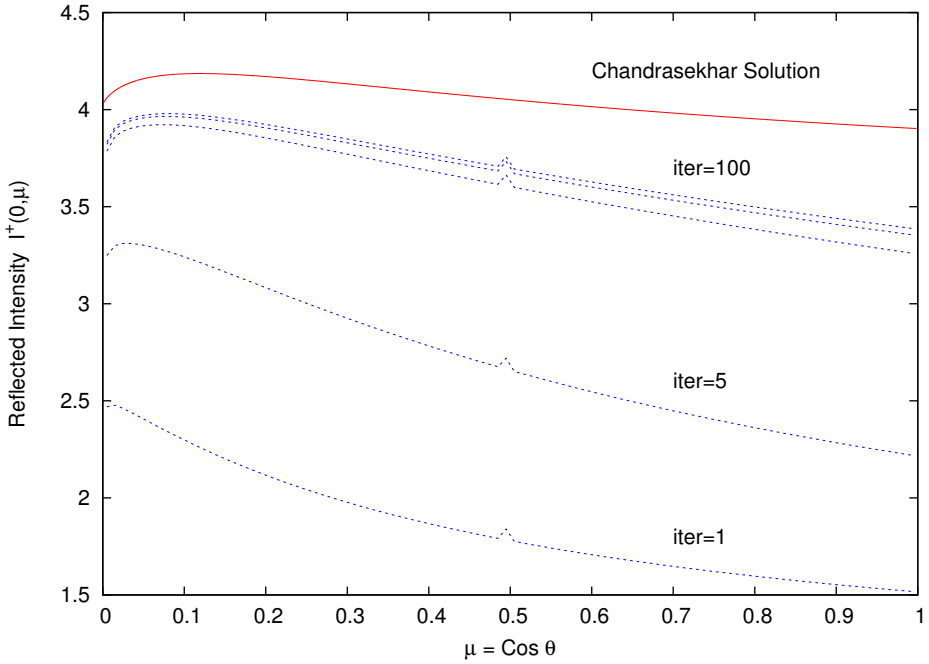

Figure 2.10 Angular distribution of the intensity at $\tau = 0$ calculated with Chandrasekhar solution (in red), and with Feautrier's method (in blue). The blue curves correspond to iterations 1, 5, 25, 50 and 100, from bottom to top, with $\tau_{max} = 10$. The incidence angle is $\mu_0 = 0.5$.

Figure 2.10 we show the angular distribution of the emergent intensity (at $\tau = 0$), calculated with equation (2.158) (in red), and the one resulting with our lambda iterative Feautrier routine (in blue) for different numbers of iterations. Both results were calculated using a grid with 100 angle points. The H-function in the Chandrasekhar solution was evaluated numerically using the procedure described previously (Hiroi, 1994). For our solution we used the Feautrier method described before, assuming $S_\nu = J_\nu$, $I_{bb} = 0$ and $\tau_{max} = 10$.

The blue curves in the plot are the resulting intensities for 1, 5, 25, 50 and 100 iterations, from bottom to top. Once again we can see our solution converges at τ^2_{max} iterations. The small peak present in all our curves is due to an small numerical error

that occurs at the angle of the incident radiation, which in this case is $\mu_0 = 0.5$.

Although our solution converges as expected, there is a significant discrepancy with the Chandrasekhar solution. The reason for this difference is because our calculation stops at $\tau_{max} = 10$, while equation 2.158 represents the solution for a semi-infinite slab. The error on average is $\sim 5 - 10\%$.

For our purposes we desire to cover the largest optical depth possible for realistic computational times and resources. Since Lambda iteration requires τ^2 loops to converge, we performed different calculations as in Figure 2.10 changing the value of τ_{max}. In Figure 2.11 we show the resulting (average) difference between Chandrasekhar and our solution, as a function of τ_{max}. It is clear in this Figure that diminishing improvement is achieved after $\tau_{max} \sim 20$, taking into account the required number of iterations. Therefore we limit all our calculations to $\tau_{max} = 10$, with the understanding that our resulting energy budget may be in error by as much as 10%.

2.4 Summary

The Compton down-scattering of X-rays by cold electrons can be accurately treated using a Gaussian profile approximation, which simplifies the procedure and reduces the computing time. The Feautrier method to solve the problem of radiative transfer has shown to be an excellent formalism, that can be extended to more general problems. The specific cases we discuss in this Chapter are limited to the isotropic scattering, assuming a quite simple source function. However, future investigation is needed in order to evaluate the accuracy of the method in a more realistic problem. The coupling between Comptonization and Radiative Transfer is crucial in accretion disc models.

Because the temperature profile over the disc depends on the radiation field at each point, and the ionization balance required for a realistic definition of the source function in radiation transfer depends on the temperature of the gas; a self-consistent approach must be taken into account. Shakura & Sunyaev equations provide a de-

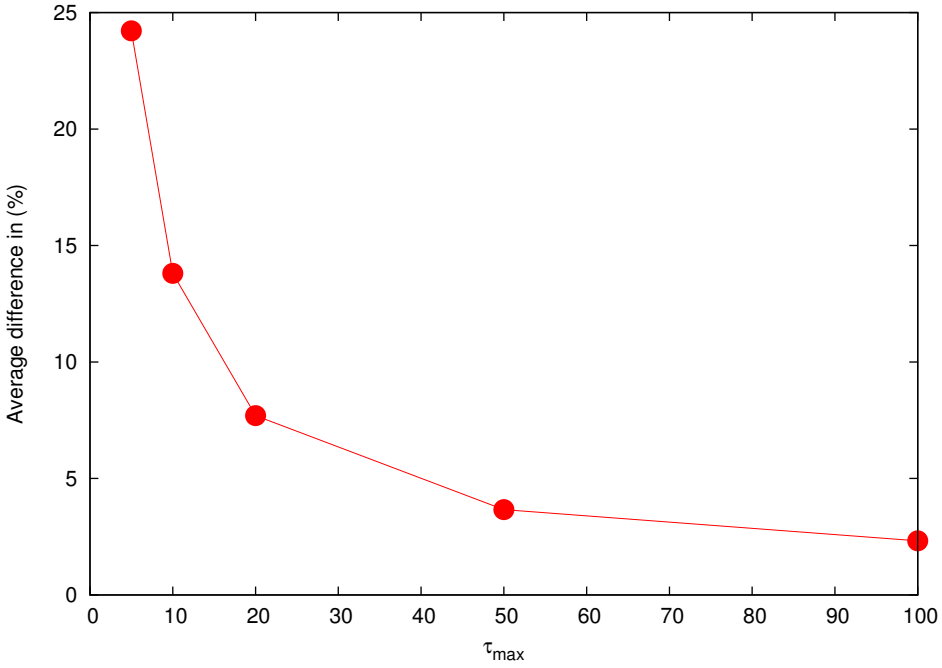

Figure 2.11 Percentual average difference between Chandrasekhar and Feautrier solutions as a function of the maximum optical depth.

scription of the geometry and a first guess for the state of the gas. Having a first estimate of the temperature profile, one can calculate the radiation field after many scatterings using the radiative transfer equations. The new radiation field can be then used to recalculate a temperature profile. Iterations of the whole process must be carried out to ensure a convergence of both solutions.

3

X-ray reflected spectra from accretion disk models

3.1 Introduction

The X-ray spectra from active galactic nuclei (AGN) and X-ray binaries often show evidence of interaction between radiation emitted near the compact object and the nearby gas, which leads to signatures imprinted on the observed spectrum. The effects of this reflection include iron K line emission, in the range 6-8 keV, which is observed from nearly all accreting compact sources (Gottwald et al., 1995); and the flattening of the spectrum above 10 keV, usually called the high energy bump or the Compton hump, since it originates due to the Compton scattering of photons by cold electrons in the gas.

The profile of the iron K line carries important information about the physics of the material around the compact object. Since the emission may occur in a relatively small region close to the center, the line profile can be affected by relativistic effects. The best-known example is the Seyfert 1 galaxy MCG-6-30-15 (Tanaka et al., 1995; Iwasawa et al., 1999), for which the iron line appears to be broad and skewed well beyond the instrumental resolution. Model line profiles for Schwarzschild and Kerr metrics have been calculated by Fabian et al. (1989) and Laor (1991), respectively.

Brenneman & Reynolds (2006) have used this information to constrain the spin of the black hole harbored by this AGN.

Observations of other accreting systems such as low mass X-ray binaries (LMXB) have also revealed the iron K line in emission. Bhattacharyya & Strohmayer (2007) reported the detection of a broad iron line emission in the *XMM Newton* spectrum of the LMXB system Serpens X-1. Using *Suzaku* observations, Cackett et al. (2008) confirmed this detection and found similar emission in two other LMXBs (4U 1820-30 and GX 349+2). Assuming relativistic broadening and applying the same models used in AGN observations, these authors have derived estimates for the inner radius of the accretion disk which can be used as an upper limit for the radius of the neutron star. Similar behavior appears in the millisecond pulsar SAX J1808.4-3658 (Cackett et al., 2009). Since the temperature of the surface layers of an accretion disk around a stellar-mass black hole or a neutron star is expected to be much higher than the temperature in the accretion disk of an AGN (see Equation 3.18), the Compton down scattering of photons can also modify the emission profile and even contribute to the broadening of the iron K line (Ross & Fabian, 2007). Reis et al. (2009) found evidence for such a situation in the *Suzaku* spectrum of the LMXB 4U 1705-44.

An X-ray emission line propagating in a dense gas has a non-negligible probability of interacting with an electron, which leads to a down scattering of photons. The maximum energy shift per scattering of a photon with energy E_c due to the electron recoil (for backscattered photons at 180°), has magnitude $\Delta E_{max} = 2E_c^2/(m_e c^2 + 2E_c)$, where $m_e c^2$ is the electron rest-mass energy. Many scatterings will therefore produce a discernible "Compton shoulder" between E_c and $E_c - \Delta E_{max}$ (Pozdniakov et al., 1979; Illarionov et al., 1979; Matt et al., 1991). Although the Compton shoulder and the iron Kβ emission line are weaker than the iron Kα emission line, both have been detected in AGN observations, especially those from the X-ray observatory *Suzaku* (Markowitz et al., 2007; Reeves et al., 2007; Yaqoob et al., 2007), and at least in one LMXB, GX 301-2 (Watanabe et al., 2003).

Initial studies of reprocessed radiation by cold matter were due to Lightman & Rybicki (1980) and Lightman et al. (1981), who derived the Green's functions for the

scattering of photons by cold electrons and discussed the implications for AGN observations (Lightman & White, 1988). George & Fabian (1991) included line production in their Monte Carlo calculations, while photoionization equilibrium was included by Zycki et al. (1994). Several authors expanded these studies assuming constant density along the vertical direction of the disk (Done et al., 1992; Ross & Fabian, 1993; Matt et al., 1993; Czerny & Zycki, 1994; Krolik et al., 1994; Magdziarz & Zdziarski, 1995; Ross et al., 1996; Matt et al., 1996; Poutanen et al., 1996; Blackman, 1999; Ross & Fabian, 2005), while hydrostatic calculations have been carried out by Rozanska & Czerny (1996); Nayakshin et al. (2000); Nayakshin & Kallman (2001); Ballantyne et al. (2001); Dumont et al. (2002) and Ross & Fabian (2007).

Nevertheless, one of the most significant limitations inherent in current reflection models is the limited treatment of the physics governing the atomic processes affecting the excitation and emission from the ions in the atmosphere, especially the iron K-shell structure. In most cases, reflection models implement analytic fits to the partial Hartree-Dirac-Slater photoionization cross sections of Verner & Yakovlev (1995), together with the line energies, fluorescence and Auger yields from Kaastra & Mewe (1993), which has been proven to be over simplified and incomplete (Gorczyca & McLaughlin, 2005). In some cases, the models lack atomic data for any of the neutral species (except for H and He).

In this chapter we present new models for illuminated accretion disks and their structure implementing state-of-the-art atomic data for the isonuclear sequences of iron (Kallman et al., 2004), and oxygen (García et al., 2005). In addition, the energy, spatial and angular resolution of our calculations are greater than previous works. The ionization balance calculations are performed in detail using the latest version of the photoionization code XSTAR. The radiation transfer equation is solved at each depth, energy and angle using the Feautrier formalism. We assume plane-parallel geometry and azimuthal symmetry.

This chapter is organized in the following way. In Section 3.2 we describe the theory and numerical methods used to solve radiation transfer, ionization and energy equilibrium, and the atomic data. In Section 3.3 we present a set of models for

constant density atmospheres at different degrees of ionization, viewing and incidence angles, as well as the effect of the abundance on the reflected spectrum. Finally, the main conclusions are summarized in Section 3.4.

3.2 Methodology

In this section we describe the theory used in our calculations, in particular, the numerical methods to solve the radiation transfer equation, the ionization equilibrium, energy conservation and the new atomic data incorporated in our models.

3.2.1 Radiative Transfer

The standard form of the transfer equation for a one dimensional, plane-parallel atmosphere is given by

$$\mu \frac{\partial I(z,\mu,E)}{\partial z} = \eta(z,E) - \chi(z,E) I(z,\mu,E), \tag{3.1}$$

where μ is the cosine of the angle with respect to the normal, and $\eta(z,E)$ and $\chi(z,E)$ are the total emissivity and opacity, respectively. It is convenient to write this equation in terms of the Thomson optical depth, $d\tau \equiv -\alpha_T dz = -\sigma_T n_e dz$, where σ_T is the Thomson cross section ($= 6.65 \times 10^{-25}$ cm^2), and n_e is the electron number density, such that

$$\omega(\tau,E)\mu \frac{\partial I(\tau,\mu,E)}{\partial \tau} = I(\tau,\mu,E) - \frac{\eta(\tau,E)}{\chi(\tau,E)} \tag{3.2}$$

where we have defined

$$\omega(\tau,E) \equiv \frac{\alpha_T}{\chi(\tau,E)}. \tag{3.3}$$

To solve the equation of radiative transfer we use Lambda iteration in the Feautrier formalism, as described in § 6.3 of Mihalas (1978). By restricting μ to the half-range $0 \leq \mu \leq 1$ to express the radiation field in its incoming and outgoing components, and using the symmetric and antisymmetric averages:

$$u(\tau,\mu,E) = \frac{1}{2}[I(\tau,+\mu,E) + I(\tau,-\mu,E)] \tag{3.4}$$

$$v(\tau, \mu, E) = \frac{1}{2}[I(\tau, +\mu, E) - I(\tau, -\mu, E)], \tag{3.5}$$

one can rewrite the Equation (3.2) as a second order differential equation

$$\mu^2\omega^2(E)\frac{\partial^2 u(\mu, E)}{\partial\tau^2} + \mu^2\omega(E)\frac{\partial\omega(E)}{\partial\tau}\frac{\partial u(\mu, E)}{\partial\tau} = u(\mu, E) - S(E) \tag{3.6}$$

where we have omitted the obvious dependence on τ. Notice that the second term on the left hand side of the equation appears since we are using the energy-independent Thomson optical depth as length variable, instead of the total optical depth $d\tau(E) = -\chi(z, E)dz$.

The second term in the right-hand side is the source function, which is defined at each depth and frequency as

$$S(E) = \frac{\eta(E)}{\chi(E)} = \frac{\alpha_{kn}J(E) + j(E)}{\alpha_{kn} + \alpha_a} \tag{3.7}$$

where

$$J(E) = \int_0^1 u(\mu, E)d\mu, \tag{3.8}$$

is the mean intensity (first moment of the intensity), and $j(E)$ is the thermal continuum plus line emissivity calculated at each depth. Here α_{kn} and α_a are the scattering and absorption coefficients, respectively: the former is defined by the product of the density times the Klein-Nishina cross section, while the latter contains the continuum cross section due bound-bound, bound-free and free-free absorption. Both $j(E)$ and α_a are obtained from the ionization balance at each point using XSTAR.

We also consider the redistribution of the photons due to Compton scattering using a Gaussian kernel convolved with $J(E)$. The Gaussian is centered at

$$E_c = E_0(1 + 4\theta - \epsilon_0), \tag{3.9}$$

where $\theta = kT/m_ec^2$ is the dimensionless temperature, E_0 is the initial photon energy and $\epsilon_0 \equiv E_0/m_ec^2$. The energy dispersion is given by $\sigma = E_0\left[2\theta + \frac{2}{5}\epsilon_0^2\right]^{1/2}$.

Therefore the total source function at each depth, as a function of the energy, is given by:

$$S(E) = \frac{\alpha_{kn}}{\chi(E)}J_c(E) + \frac{j(E)}{\chi(E)} \tag{3.10}$$

where

$$J_c(E) = \int dE' J(E') P(E', E) \tag{3.11}$$

is the Comptonized mean intensity, for which the kernel function (normalized to unity), can be written explicitly as

$$P(E_c, E_s) = \frac{1}{\sigma \pi^{1/2}} \exp\left[\frac{-(E_s - E_c)^2}{\sigma^2}\right]. \tag{3.12}$$

As shown by Ross & Fabian (1993), this treatment describes adequately the down scattering of photons with energies less than ~ 200 keV. This approximation is also discussed by Ross et al. (1978) and Nayakshin et al. (2000). There is an important limitation while using this treatment: if the bin width of a certain energy E_c is greater than 2 times the dispersion of the Gaussian, then there is a large probability for a photon to scatter into its own energy bin, producing a numerical pile up of photons at those energies. We use a logarithmically spaced energy grid, so the resolving power $\mathcal{R} = E/\Delta E$ is a constant that only depends on the number of grid points. Therefore, the bin width is $\Delta E = E/\mathcal{R}$, and the pile up occurs at a critical energy E_p when $\Delta E = 2\sigma(E_p)$; or

$$E_p = m_e c^2 \left[\frac{5}{4\mathcal{R}^2} - \frac{5kT}{m_e c^2}\right]^{1/2}. \tag{3.13}$$

From the last equation it is clear that the pile up appears only at low temperatures, specifically for temperatures less than $T_p = m_e c^2 / 4k\mathcal{R}^2$. The lowest resolving power used here is $\mathcal{R} = 350$, and then $T_p \sim 10^4$ °K. We will show later that we consider no cases for which the gas temperature becomes lower than this value. In fact, in the extreme limit of $T = 0$ (and using the same resolving power), the highest pile up energy would be $E_p \sim 1.6$ keV, leaving the high energy part of the spectrum unaffected.

To complete this solution, two boundary conditions are imposed; one at the top ($\tau = 0$), and one at the maximum depth ($\tau = \tau_{max}$). At the top, the incoming radiation field $I(0, -\mu, E)$ is equal to a power law, with photon index and normalization as free (input) parameters in the calculation. Subtracting Equations (3.4) and (3.5)

$$u(0, \mu, E) - v(0, \mu, E) = I_{inc} \tag{3.14}$$

and it is easy to show that

$$v(\tau,\mu,E) = \omega(\tau,E)\mu\frac{\partial u(\tau,\mu,E)}{\partial\tau} \tag{3.15}$$

therefore at the surface,

$$\omega(0,E)\mu\left[\frac{\partial u(\tau,\mu,E)}{\partial\tau}\right]_0 - u(0,\mu,E) = -I_{inc}. \tag{3.16}$$

At the lower boundary we specify the outgoing $I(\tau,+\mu,E)$ radiation field to be equal to a blackbody with the expected temperature for the disk:

$$\omega(\tau_{max},\mu,E)\mu\left[\frac{\partial u(\tau,\mu,E)}{\partial\tau}\right]_{\tau_{max}} + u(\tau_{max},\mu,E) = B(T_{disk}) \tag{3.17}$$

This condition appears since we assume that there is an intrinsic disk radiation due to the viscosity of the gas (Shakura & Sunyaev, 1973). The disk temperature at the lower boundary is then given by

$$T_{disk} = \left\{\frac{3GM\dot{M}}{8\pi\sigma R^3}\left[1-\left(\frac{R_0}{R}\right)^{1/2}\right]\right\}^{1/4} \tag{3.18}$$

where G is the Newtonian gravitation constant, σ is Stefan's constant, M is the mass of the central object, $\dot{M}$ the mass accretion rate, R is the distance from the center, and R_0 is the smallest radius at which the disk dissipates energy. Shakura & Sunyaev (1973) predicted that for a non-rotating black hole this occurs at the innermost stable circular orbit (ISCO), or $R_0 = 3R_s = 6GM/c^2$, where R_s is the Schwarzschild radius. However, recent magneto-hydrodynamics calculations (Noble et al., 2010), have shown that the electromagnetic stress responsible for the energy generation rises steadily inward in the region inside the ISCO, falling sharply to zero just before the event horizon. Therefore, we will assume $R_0 = R_s$, allowing energy generation in the inner part of the disk. It is clear that the properties of the accretion disk are introduced in the calculation by means of the lower boundary condition. Further, since we assume constant density for the gas along the vertical direction, it is customary to parametrize each model by the ratio of the net flux incident at

the surface over the density, using the common definition of the ionization parameter (Tarter et al., 1969):

$$\xi = \frac{4\pi F_{\rm x}}{n_e}, \tag{3.19}$$

where $F_{\rm x}$ is the flux of the illuminating radiation in the 1-1000 Ry energy band. Finally, Equations (3.6),(3.10),(3.16) and (3.17) are converted to a set of difference equations by discretization of depths, energies and angles. The solution of the system is found by forward elimination and back substitution. A full transfer solution requires the Feautrier solution to be iteratively repeated, in order to self-consistently treat the scattering process. This procedure requires $\sim \tau_{max}^2$ iterations (lambda iterations) for convergence.

3.2.2 Structure of the gas

Given the solution for the radiation field at each point in the atmosphere, we use the photoionization code XSTAR (Kallman & Bautista, 2001) to determine the state of the gas for a given value of the number density. The state of the gas is defined by its temperature and the level populations of the ions. The relative abundances of the ions of a given element and the level populations are found by solving the ionization equilibrium equations under the assumption of local balance, subject to the constrain of particle number conservation for each element. Schematically, for each level

$$\text{Rate in} = \text{Rate out}. \tag{3.20}$$

The processes include spontaneous decay, photoionization, charge transfer, electron collisions, radiative and dielectronic recombination. Similarly, the temperature of the gas is found by solving the equation of thermal equilibrium, which may be written schematically as

$$\text{Heating} = \text{Cooling}. \tag{3.21}$$

The heating term includes photoionization heating (including the Auger effect), Compton heating, charge transfer and collisional de-excitation. The cooling term includes

radiative and dielectronic recombination, bremsstrahlung, collisional ionization, collisional excitation of bound levels and charge transfer. All processes include their respective inverses so that the populations approach to local thermodynamic equilibrium (LTE) values under the appropriate conditions (i.e., high density or Planckian radiation field).

3.2.3 Radiative equilibrium

XSTAR calculates level populations, temperature, opacity and emissivity of the gas assuming that all the physical processes mentioned in the previous section are in steady state. Radiative equilibrium is achieved by calculating the integral over the net emitted and absorbed energies in the radiation field (E_c and E_h, respectively); and varying the gas temperature until the integrals satisfy the criterion

$$\frac{E_h - E_c}{E_h + E_c} \leq 10^{-4}. \tag{3.22}$$

The radiative equilibrium condition must be ensured also while solving the transfer equation. According to equation (2-83b) in Mihalas (1978):

$$\int_0^\infty \chi(E)\,[J(E) - S(E)]\,dE = 0, \tag{3.23}$$

i.e., the total energy absorbed by a volume of material must be equal to the total energy emitted (note that, as in § 3.2.1, we have omitted the explicit dependence on τ in the equations). By using the definitions of the flux and radiation pressure (second and third moments of the radiation field):

$$H(E) = \int_0^1 v(\mu, E)\mu d\mu \tag{3.24}$$

and

$$K(E) = \int_0^1 u(\mu, E)\mu^2 d\mu, \tag{3.25}$$

one can rewrite Equation (3.15) as

$$H(E) = \omega(E)\frac{\partial K(E)}{\partial \tau}. \tag{3.26}$$

Taking the derivative with respect to τ and multiplying by $\omega(E)$

$$\omega(E)\frac{\partial H(E)}{\partial \tau} = \omega^2(E)\frac{\partial^2 K(E)}{\partial \tau^2} + \omega(E)\frac{\partial \omega(E)}{\partial \tau}\frac{\partial K(E)}{\partial \tau}, \tag{3.27}$$

and comparing with the transfer Equation (3.6) integrated over μ,

$$\omega(E)\frac{\partial H(E)}{\partial \tau} = J(E) - S(E). \tag{3.28}$$

From here it is clear that the radiative equilibrium condition (3.23) is equivalent to

$$\frac{\partial}{\partial \tau}\int_0^\infty H(E)dE = 0, \tag{3.29}$$

i.e., the net flux must be conserved for any optical depth. Further, inserting the source function (3.10) in the right-hand side of (3.28):

$$\frac{\partial}{\partial \tau}\int_0^\infty H(E)dE = \frac{1}{\alpha_T}\int_0^\infty \left\{\alpha_{kn}\left[J(E) - J_c(E)\right] + \alpha_a J(E) - j(E)\right\} dE. \tag{3.30}$$

If the gas temperature is high enough ($T \gtrsim 10^6$ °K), the Compton scattering is the dominant process, while both the opacity and the emissivity of the gas are negligible and only the first term in the right-hand side of Equation (3.30) is important. For lower temperatures the inverse occurs: $J(E) \approx J_c(E)$, which cancels out the first term. Thus, using (3.29)

$$\frac{1}{\alpha_T}\int_0^\infty \left[\alpha_a J(E) - j(E)\right] dE = 0. \tag{3.31}$$

The conservation of the flux through the atmosphere is formally equivalent to the thermal equilibrium condition (3.21), but its accuracy will depend on the error associated with the evaluation of the left-hand side of Equation (3.31). Although we limit the error in the calculation of the emissivities $j(E)$ and opacities α_a by imposing the condition (3.22), the numerical conservation of the flux is a difficult task due to the fact that small errors accumulate over the large column densities covered in the calculation. It can be seen from Equation (3.31) that the error required in the calculation of emissivities and opacities must be of the order of α_T^{-1}. Assuming that typical values for the density are $n_e \sim 10^{10} - 10^{16}$ cm^{-3}, then $10^8 \lesssim \alpha_T^{-1} \lesssim 10^{14}$, much

greater than the value required in (3.22). Therefore, we also apply a renormalization of the emissivities calculated by XSTAR before the solution of the transfer equation, such that:

$$j^{new}(E) = j(E)\frac{\int_0^\infty \alpha_a J(E)dE}{\int_0^\infty j(E)dE}, \tag{3.32}$$

at each depth. By implementing this correction in our models, we have found that the net flux (and therefore the energy) is conserved better than 1% for intermediate to large values of the ionization parameter ($\log \xi > 3$), but the maximum error can be $\sim 7\%$ for low-ionization calculations ($\log \xi < 3$). These errors are estimated by comparing the total fluxes incident on the gas (i.e., $F_{\rm x}+F_{disk}$), with the total emergent flux.

3.2.4 Atomic data

The XSTAR atomic database collects recent data from many sources including CHIANTI (Landi & Phillips, 2006), ADAS (Summers, 2004), NIST (Ralchenko et al., 2008), TOPbase (Cunto et al., 1993) and the IRON project (Hummer et al., 1993). The database is described in detail by Bautista & Kallman (2001). Additionally, the atomic data associated with the K-shell of the Fe ions incorporated in the current version of XSTAR has been recently calculated and represents the most accurate and complete set available to the present. Energy levels and transition probabilities for first row ions Fe XVIII-Fe XXIII were reported by Palmeri et al. (2003a); for second row ions Fe X-Fe XVII were reported by Mendoza et al. (2004); and for the third row ions Fe II-Fe IX by Palmeri et al. (2003b). The impact of the damping by spectator Auger resonances on the photoionization cross sections was discussed by Palmeri et al. (2002). Photoionization and electron impact cross sections were presented for second row ions by Bautista et al. (2004). Energy levels, transition probabilities and photoionization cross sections for Fe XXIV were calculated by Bautista et al. (2003). A compilation of these results and a careful study of their impact on the photoionization models can be found in Kallman et al. (2004). Moreover, XSTAR also includes the atomic data relevant to the photoabsorption near the K edge of all oxygen ions

calculated by García et al. (2005).

The approach used by these authors for the computation of the atomic parameters of iron and oxygen was based on the implementation and comparison of results obtained from different atomic codes of public domain, namely AUTOSTRUCTURE (Badnell, 1997), HFR (Cowan, 1981), and the Breit-Pauli R-Matrix package (BPRM, Seaton, 1987; Berrington et al., 1987).

3.2.5 Iteration procedure

Starting at the top of the disk, the vertical structure of the gas is found by solving ionization and thermal balance at each spatial zone using XSTAR, as described in § 3.2.2. Since the radiation field is unknown the first time this is done, it is set to be equal to the incident power law at each depth. Once the last zone is reached, the temperature and density profiles are known, as well as the emissivities and opacities for each depth and energy. With this information the radiative transfer Equation (3.6) is solved as described in § 3.2.1 until the solution converges, which requires $\sim \tau_{max}^2$ Lambda iterations. This provides a new and more accurate radiation field, that can be used to recalculate the structure of the gas. Because the emissivities and opacities are updated when the structure of the gas is recalculated, the radiative transfer calculations must be also repeated. We then continue with this process until all quantities stop changing within a small fraction. Typically, this requires ~ 20 gas structure calculations, times τ_{max}^2 Lambda iterations.

For our purposes, we desire to cover the largest optical depth possible for realistic computational times and resources. Since Lambda iteration requires τ_{max}^2 loops to converge, we performed different numerical experiments, changing the value of τ_{max}. Comparisons with the semi-analytic solution by Chandrasekhar (1960) showed that the error behaves, in general, as $\sim 1/\tau_{max}$, corresponding to a leakage of energy through a scattering dominated slab. The comparison also showed that diminishing improvement is achieved after $\tau_{max} \sim 10 - 20$, taking into account the required number of iterations. Therefore we limit all our calculations to $\tau_{max} = 10$, with the

understanding that our resulting global energy budget may be in error by as much as 10%. Finally, our calculations consider high resolution spectra with an energy grid of at least 5×10^3 points ($\mathcal{R} = E/\Delta E \sim 350$), 200 spatial zones, and 50 angles to account for anisotropy of the radiation field. Typically, each one of these models can be calculated in few hours in a last generation PC, which means that a grid of 20-30 models can be produced in one or two weeks, depending on the computational resources available, and the specific parameters to represent the models (e.g., lower ionization models tend to run slower than high ionization cases). This is relevant since XSPEC model tables can be easily generated and used in the interpretation of astronomical observations. Higher resolution can be achieved, although computational time increases (at least) with the square of the number of energy grid points, quickly imposing limits on the sizes of the grids.

3.3 Results

In this section we show the results obtained with our model for constant density atmospheres. We present a total of 20 reflection models, calculated for various representative conditions. These models and input parameters used to produce them are summarized in Table 3.1. The first column of the Table contains an identification number assigned to each model and it will be used for reference through the rest of this Chapter. The next columns contain the input parameters that have been varied for each model, namely: the flux $F_{\rm x}$ of the ionizing radiation (in the 1-1000 Ry energy range), the resulting logarithm of the ionization parameter ξ (see Equation 3.19), the spectral energy resolution or resolving power $\mathcal{R} = E/\Delta E$ (determined by the number of energy grid-points used), the cosine of the incidence angle of the illuminating radiation with respect to the normal of the disk μ_0, and the abundance of iron normalized to its solar value $\rm A_{Fe}$. Other input parameters not listed in the Table since they are constant and common to all the models are: density $n_e = 10^{15}$ cm^{-3}, photon index of the incident radiation $\Gamma = 2$, mass of the central object $M = 10^8$ M$_\odot$, distance from the central object $R = 7R_s$, and the mass accretion rate $\dot{M} = 1.6 \times 10^{-3}\dot{M}_{Edd}$, where

$R_s = 2GM/c^2$ is the Schwarzschild radius and $\dot{M}_{Edd}$ is the accretion rate at the Eddington limit. We have chosen these parameters such that the numbers are similar to those typically used by previous authors. However, note that these parameters only affect the present models by changing the effective temperature of the disk (equivalent to changing the intrinsic disk flux), to be used as the inner boundary condition (3.17) in the radiation transfer problem. Specifically, by using Equation (3.18) this set of parameters correspond to an intrinsic disk flux of $F_{disk} = 3.6 \times 10^{13}$ erg/cm^2/s, or an effective temperature of $T_{disk} = 2.8 \times 10^4$ °K, which represents a cold disk when compared to the temperatures typically produced by the illuminating fluxes used here. This is convenient since it allows us to analyze the reprocessed spectrum as a direct consequence of the incident power law without significant modifications due to the black body of the disk.

3.3.1 Temperature profiles

The Figure 3.1 shows the temperature profile as a function of the Thomson optical depth resulting from constant density models for ten different ionization parameters (models 1-10 in Table 3.1). In the Figure, the lower left curve corresponds to the least ionized case, and each consecutive to a higher value of $F_{\rm x}$. The values of log ξ are included next to the respective curves. Because the τ grid is fixed with logarithmic spacing, the surface of the disk is in practice chosen to be $\tau_{top} = 10^{-2}$. The optical depth is measured from the surface towards the interior of the disk. Since the density is assumed to be constant, all these calculations are carried out along a distance of $\Delta z = \Delta\tau/\sigma_T n_e \approx 1.5 \times 10^{10}$ cm.

These curves show very similar general behavior; the temperature is higher at the surface (due to the heating by the incident radiation) and decreases towards the interior of the disk, reaching a minimum temperature. For the high illumination cases (large values of ξ, and/or very close to the surface), the dominant mechanism

Table 3.1. List of reflection models with their respective input parameters

Model	$F_{\rm x}$[a]	log ξ[b]	$\mathcal{R}$	μ_0	$A_{\rm Fe}$
1	5×10^{14}	0.8	350	0.71	1.0
2	1×10^{15}	1.1	350	0.71	1.0
3	2×10^{15}	1.5	350	0.71	1.0
4	5×10^{15}	1.8	350	0.71	1.0
5	1×10^{16}	2.1	350	0.71	1.0
6	2×10^{16}	2.5	350	0.71	1.0
7	5×10^{16}	2.8	350	0.71	1.0
8	1×10^{17}	3.1	350	0.71	1.0
9	2×10^{17}	3.5	350	0.71	1.0
10	5×10^{17}	3.8	350	0.71	1.0
11	2.5×10^{15}	1.5	3500	0.71	1.0
12	2.5×10^{16}	2.5	3500	0.71	1.0
13	2.5×10^{17}	3.5	3500	0.71	1.0
14	5×10^{16}	2.8	350	0.95	1.0
15	5×10^{16}	2.8	350	0.50	1.0
16	5×10^{16}	2.8	350	0.05	1.0
17	2.5×10^{16}	2.5	350	0.71	0.2
18	2.5×10^{16}	2.5	350	0.71	2.0
19	2.5×10^{16}	2.5	350	0.71	5.0
20	2.5×10^{16}	2.5	350	0.71	10.0

[a] erg/cm^2/s (1-1000 Ry)

[b] erg cm/s (See Equation 3.19)

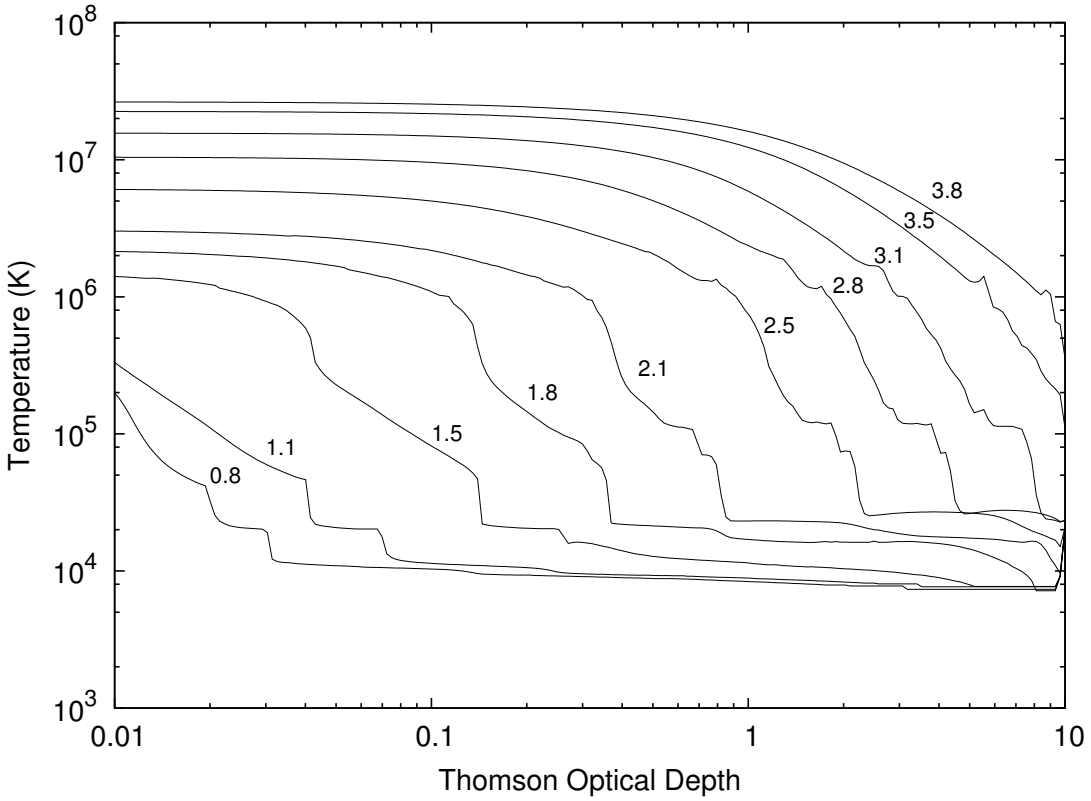

Figure 3.1 Temperature profiles for different illumination fluxes using constant density models ($n = 10^{15}$ cm^{-3}). The value of log ξ is shown next to each corresponding curve (models 1-10).

is Compton heating and cooling (Krolik et al., 1981), with a rate given by:

$$n_e \Gamma_e = \frac{\sigma_T}{m_e c^2} \left[\int EF(E)dE - 4kT \int F(E)dE \right], \tag{3.33}$$

in the non relativistic limit. When this process dominates, the temperature approaches an asymptotic value, the *Compton temperature*, given by the balance of the two terms in the previous equation:

$$T_{\rm C} = \frac{< E >}{4k}, \tag{3.34}$$

where

$$< E >= \frac{\int F(E)EdE}{\int F(E)dE} = F_{\rm tot}^{-1} \int F(E)EdE \tag{3.35}$$

is the mean photon energy. From Equations (3.34) and (3.35) it is clear that $T_{\rm C}$ only depends on the shape of the spectrum. In particular, for the incident power law used here ($\Gamma = 2$), the Compton temperature of the radiation is $T_{\rm C} = 2.8 \times 10^7$ °K. Note that the temperature at surface for the case with $\log \xi = 3.8$ (model 10) is indeed very close to $T_{\rm C}$.

In most cases, the gas remains at the high temperature limit throughout the region where the ionizing radiation field is unchanged from the incident field, thus forming a hot skin. The temperature gradually decreases in this hot skin as the bremsstrahlung cooling becomes more important. As photons are removed from the Lyman continuum energies either by scattering or absorption and re-emission, at some point hydrogen recombines and the opacity grows rapidly, causing a drop in the temperature. Eventually the opacity becomes very large so that few photons are left in the 1-1000 Ry energy range, at which point the radiation field thermalizes to a nearly constant temperature ($T \sim 10^4$ °K).

It is worthwhile to mention that for the models with the two lowest ionization parameters (models 1 and 2), the opacity of the gas is large compared to the ionizing flux even at the surface of the disk and therefore the gas reaches the low temperature limit very rapidly. Conversely, for the two models with $\log \xi = 2.5 - 3.1$ (models 6-8), the illumination is high enough to allow the photons to penetrate much deeper

into the atmosphere, and the gas remains at high temperature ($T \sim 10^6$ °K) even for large optical depths ($\tau > 1$). In fact, by looking the intermediate cases (models 3-8), one can clearly identify two temperature zones: the hot skin correspond to $T \gtrsim 10^6$ °K, while the cold region occurs for $T \lesssim 10^5$ °K. Note also that although the transition between the hot and cold regions can be sudden, there is no thermal instability in these calculations, since in all these cases the constant density restriction is applied (Krolik et al., 1981). Some of the models show small temperature inversions, such as the one in the curve corresponding to $\log \xi = 3.5$ (model 9), that can be seen around $\tau_{\rm T} \approx 6$. This inversion occurs in the place within the slab where the temperature changes rapidly but also in a zone where the resolution in the optical depth is reduced due to larger the step size in the grid, which could lead to small scale thermal instabilities in the solution (Buff & McCray, 1974). Despite this, there are no large scale thermal instabilities in these calculations, since in all these cases the constant density restriction is applied (Krolik et al., 1981).

3.3.2 Reflected spectra

Figure 3.2 shows the reflected spectra for each of the models shown in the previous section (models 1-10 in Table 3.1), in the entire energy range covered in the calculations (1 eV to 210 keV). The spectra emerging from the top of the slab are plotted as solid curves, while the intrinsic disk flux is shown in the dotted curve. The dashed curve represents the X-rays incident at the top of the disk, assumed to be in the form of a power law with $\Gamma = 2$ and an exponential high energy cutoff at 200 keV (to improve clarity, only the incident power law for the lowest ionization case is shown). The corresponding values of $\log \xi$ are indicated above each curve, starting with the smaller value at the bottom, and increasing the ionization to the top. The curves are shifted to improve clarity. From bottom to top, each consecutive curve is rescaled by a factor increased by one order of magnitude with respect to the previous one (i.e., 1, 10, 100,...,10^9). Strong absorption profiles and edges are clearly seen in the neutral cases for $\log \xi$ =0.8, 1.1 and 1.5 (models 1-3), although it is important to

mention that some small numerical problems occur in the thermal energy range of the spectrum for the lower flux case. For a few energy bins the reflected outgoing flux becomes negative, due to the large opacities for such energies (especially around 100 eV) and numerical errors in calculating the mean intensity. The redistribution of the photons due to Comptonization is evident above 10 keV (Compton bump), and in the smearing of the line profiles. For the models with the lowest illumination (models 1-3), there is a significant modification of the original power law continuum due to the large values of the photoelectric opacity for energies between 100 eV and 10 keV, where most of the strong absorption occurs. Nevertheless, none of these models shows a spectrum dominated by absorption. Even in the lowest ionization case ($\log \xi = 0.8$), there are strong emission lines present through the whole energy range. This combination of emission and absorption features in the reflected spectra is a direct consequence of our accurate treatment of radiation transfer and the temperature gradient along the vertical direction of the disk discussed in the previous section.

The iron K line shows the effects of Compton scattering in models with $\log \xi \geq 1.5$, since those are the cases for which a hot skin ($T \sim 10^6$ °K) is present for at least a fraction of the total depth of the disk. By comparing the most ionized models, in particular those for $\log \xi = 2.8$ and $\log \xi = 3.1$ (models 7 and 8), one can see a very drastic change from a highly ionized to an almost featureless spectrum, and even fewer features are seen in the two models for $\log \xi = 3.5$ and 3.8 (models 9 and 10). This is due to the fact that in these cases the gas is always at high temperature within the range of our calculations. Despite this, emission from highly ionized iron K lines is still apparent in the reflected spectrum.

Figure 3.3 shows the same results as Figure 3.2, but in the 2-10 keV energy range. Here it is possible to see the structure of the iron inner shell transitions in detail. The Compton shoulder is apparent in the first three curves from bottom to top (least ionized cases). Changes in the Fe Kα emission line are distinguishable as the ionization parameter increases. The neutral Kβ line is only evident in the three least ionized cases (models 1-3), as well as the Fe absorption edge at ~ 7.5 keV. This

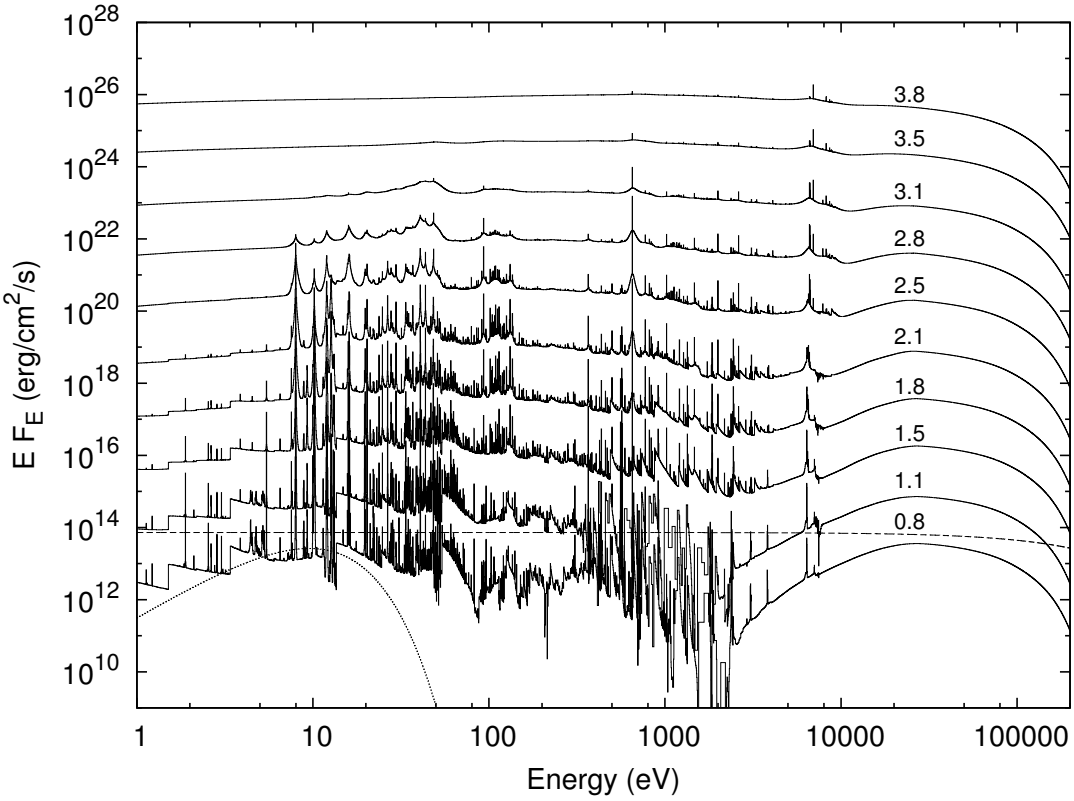

Figure 3.2 *Solid curves:* Reflected spectra for the models presented in Figure 3.1. The value of log ξ is shown next to each corresponding curve (models 1-10). The curves are shifted by arbitrary factors for clarity. These are, from bottom to top: 1, 10, 100,...,10^9. *Dashed curve:* incident ionizing spectrum (power law), corresponding to the lowest ionization case (log $\xi = 0.8$). *Dotted curve:* intrinsic disk flux (black body), common to all the models.

figure also shows a more complex structure of the iron line in intermediate cases of ionization: line positions and intensities vary between mostly neutral emission at 6.4 and 7.2 keV for Kα and Kβ, to a very ionized profile with lines around 6.5-7.0 keV and 7.8-8.2 keV for the same transitions.

We have calculated the equivalent widths for the Fe Kα lines in all these spectra. Because of the large deviations of the reprocessed continuum from the incident power law in some of these models (particularly for low ξ), in order to calculate the equivalent width we define a local continuum by interpolating a straight line between two points in the region around the line, specifically between 6 and 7 keV. The integration is performed within this range as well, such that only Kα emission is taken into account.

The resulting equivalent widths for the Fe Kα emission line vary between $\sim 400-800$ eV for the cases with $1 \lesssim \log\xi \lesssim 3$ (left panel in Figure 3.3). For higher values of the ionization parameter the equivalent widths decrease very rapidly, to approximately 40 eV for the most ionized case ($\log \xi = 3.8$, model 10). Since the gas is more ionized for high illumination, the emission of the line becomes exclusively due to H- and He-like iron ions, which combined with the extreme Compton scattering of the photons results in the reduction of the equivalent width of the line. This tendency resembles the X-ray Baldwin effect (Iwasawa & Taniguchi, 1993), which have been observed in many active galactic nuclei spectra (e.g., Page et al., 2004).

3.3.3 Spectral features

In order to provide a finer analysis of the reflected spectra, we perform calculations increasing the energy resolution by an order of magnitude, i.e., using 5×10^4 energy grid-points ($\mathcal{R} \sim 3500$). Since these calculations are more expensive in terms of CPU-time, we only show three representative cases. These calculations are shown in Figures 3.4-3.6, and correspond to models 11, 12 and 13 in Table 3.1. These spectra (Figures 3.4-3.6), are plotted in their physical units and without any renormalization or rescaling, and besides the much higher energy resolution, all the other input parameters in the models are the same as the ones used for the models present previously

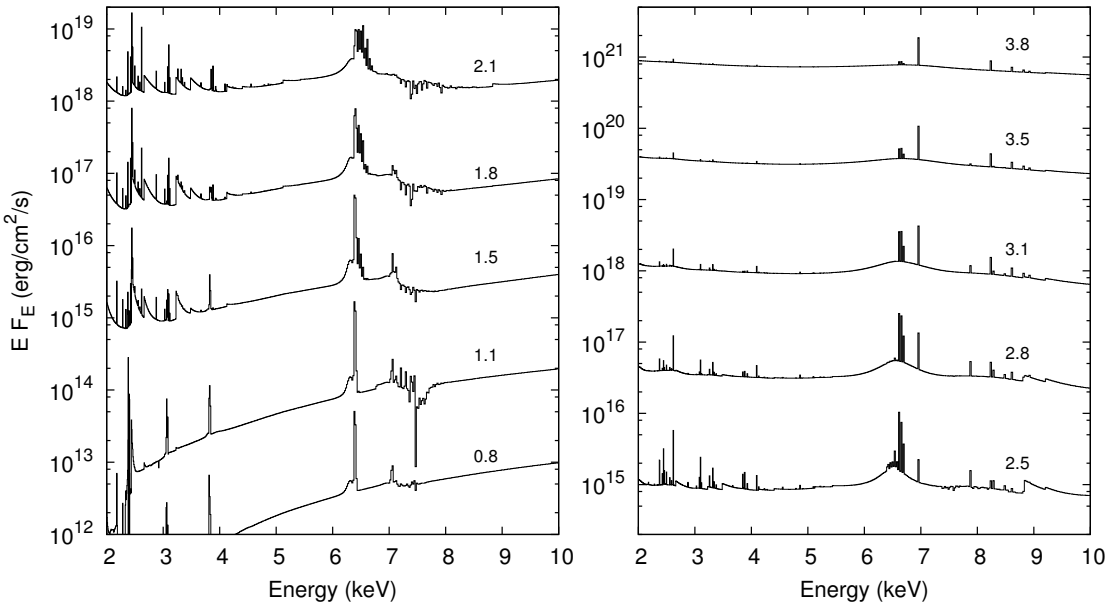

Figure 3.3 Reflected spectra as shown in Figure 3.2 in the 2-10 keV region. The value of log ξ is shown next to each corresponding curve (models 1-10). The curves are shifted by arbitrary factors for clarity. These are, from bottom to top in each panel: 1, 10, 100, $10^4, 10^5$.

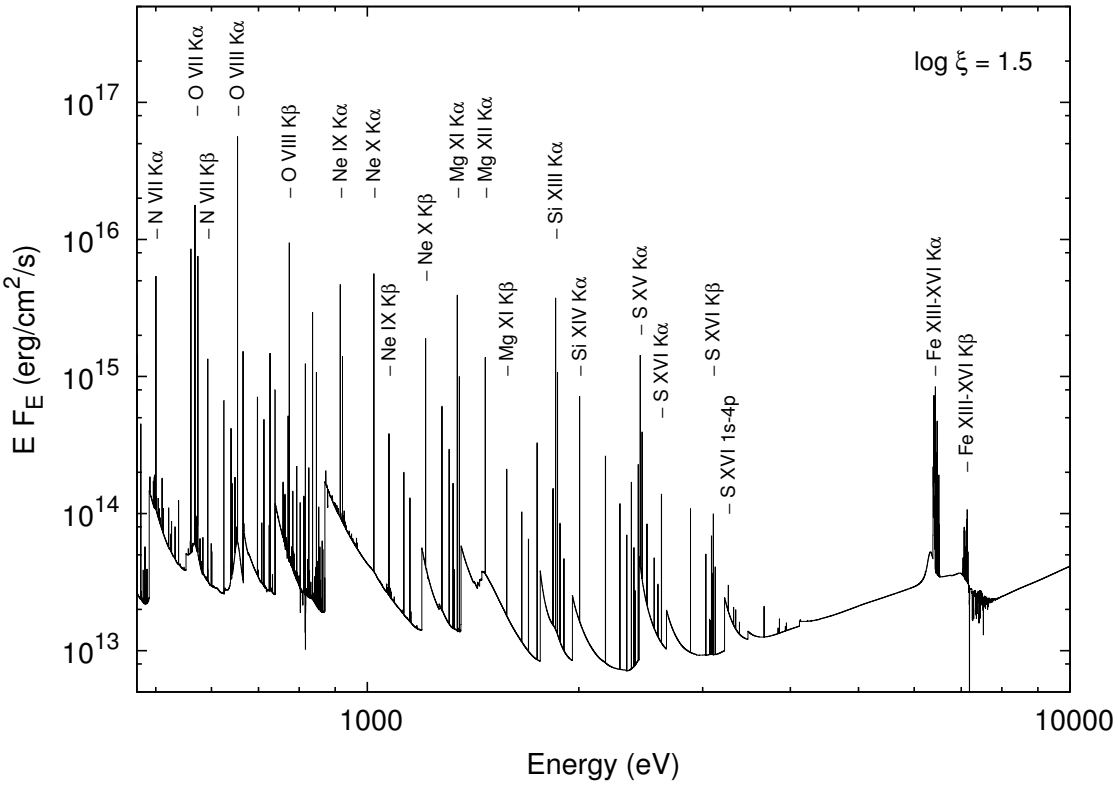

Figure 3.4 Reflected spectra for $\log \xi = 1.5$ while using a resolving power of $\mathcal{R} \sim 3500$ (model 11). All the other input parameters are the same used before (as in Figures 3.1 and 3.2), although no rescaling is applied. The strongest emission lines are labeled.

in Figures 3.1 and 3.2.

Figure 3.4 shows the reflected spectra corresponding to $\log \xi = 1.5$ (model 11), in the 0.5-10 keV energy range, while using a resolving power of $\mathcal{R} \sim 3500$. The most prominent and relevant emission lines are identified in the Figure. In general, the spectrum is dominated by many absorption edges plus radiative recombination continua (RRC). RRCs occur when a free electron is captured by an ion into an unoccupied orbit; if the electron carries more energy than it needs to be bound to the ion, the excess will be radiated as a photon. Emission K lines from H- and He-like nitrogen, oxygen, neon and magnesium are present in the region around and below 2 keV. At higher energies, there is clear emission from Si XII-XXIV and S XV-

XVI. The iron Kα and Kβ components are clearly visible at $\sim$ 6.4 keV and $\sim$ 7.1 keV, respectively, as expected from mostly neutral emission. Many lines are blended together in a small region (about 50 eV for each component), but the emission is mainly due to iron, specifically Fe XIII up to Fe XVI. The Compton shoulder in both components is also evident, as well as a very marked absorption edge at $\sim$ 7.5 keV blended with a complex structure of absorption profiles. These absorption features correspond to resonances given by transitions from the ground state to the $1s - np$ autoionizing states, where $n = 3, ..., 30$; for our particular atomic data set. These are K-vacancy states that can decay either radiatively or via Auger spectator channels, being the latter dominant for $n \geq 3$ (Palmeri et al., 2002). The resonance structure seen in this spectrum covers the 7.1-8. keV energy range, thus it is mainly due to second row Fe ions, which resemble the opacity curves shown by Palmeri et al. (2002), as well as the photionized spectra in Kallman et al. (2004), for similar values of the ionization parameter considered here. The energy position of the absorption edge indicates that it is likely produced by Fe XIII-XIV, according to the energies presented in Kallman et al. (2004) (see in particular their Figure 2).

Figure 3.5 shows the resulting spectra when $\log \xi = 2.5$ (model 12), again for a high resolution energy grid ($\mathcal{R} \sim 3500$). There is a significant change in the overall continuum, particularly in the 1-10 keV region, in comparison with the previous case ($\log \xi = 1.5$). This is because in the lower ionization case the photoelectric opacity dominates in this energy band and changes the original incident power law shape, while the continuum spectrum in Figure 3.5 still shows the original slope ($\Gamma = 2$). Lower opacity also allows the efficient propagation of line emission (since photons are able to escape), especially the emission from heavier elements (Ar XVII, Ca XIX and Ca XX), since the gas is more ionized. In general, this spectrum shows more emission lines and weaker absorption edges. However, some RRCs can still be identified, especially around the sulfur and calcium lines. The K lines from nitrogen, oxygen and neon ions are again the strongest emission features in the low energy part of the spectrum. The high energy region changes noticeably with respect to the previous case with lower ionization. The strongest Fe Kα emission in this case is due to Fe XXV

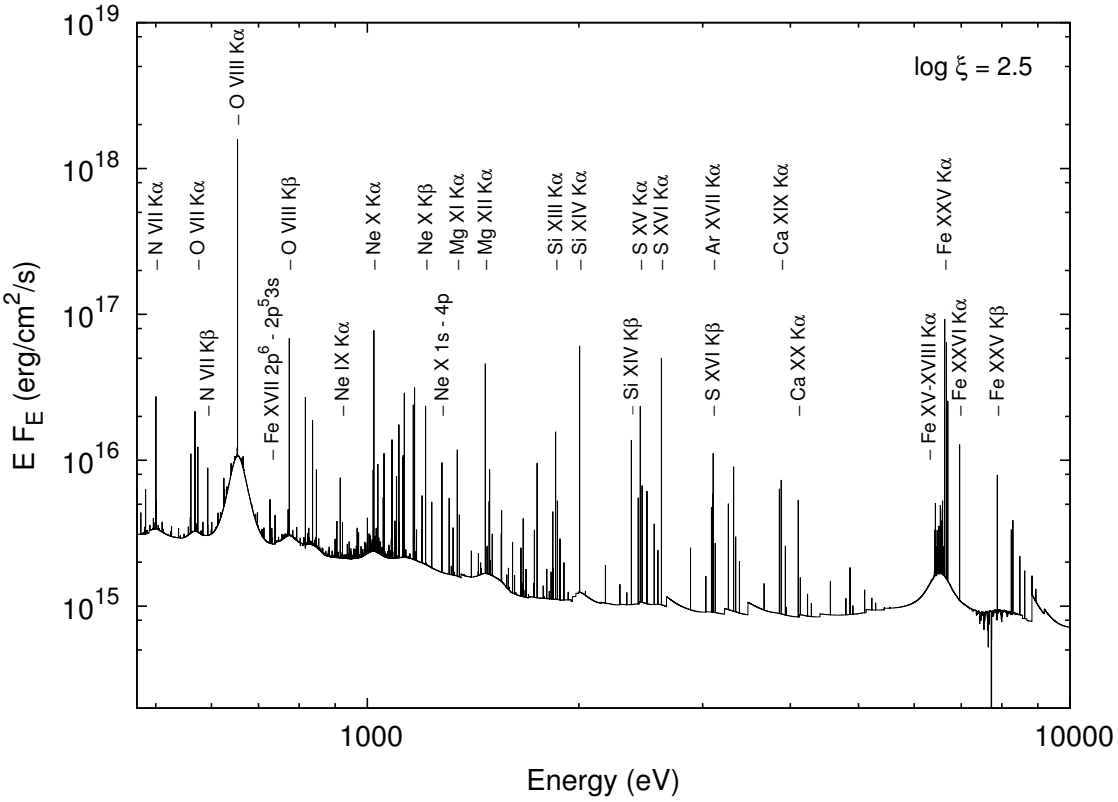

Figure 3.5 Reflected spectra for $\log \xi = 2.5$ while using a resolving power of $\mathcal{R} \sim 3500$ (model 12). All the other input parameters are the same used before (as in Figures 3.1 and 3.2), although no rescaling is applied. The strongest emission lines are labeled.

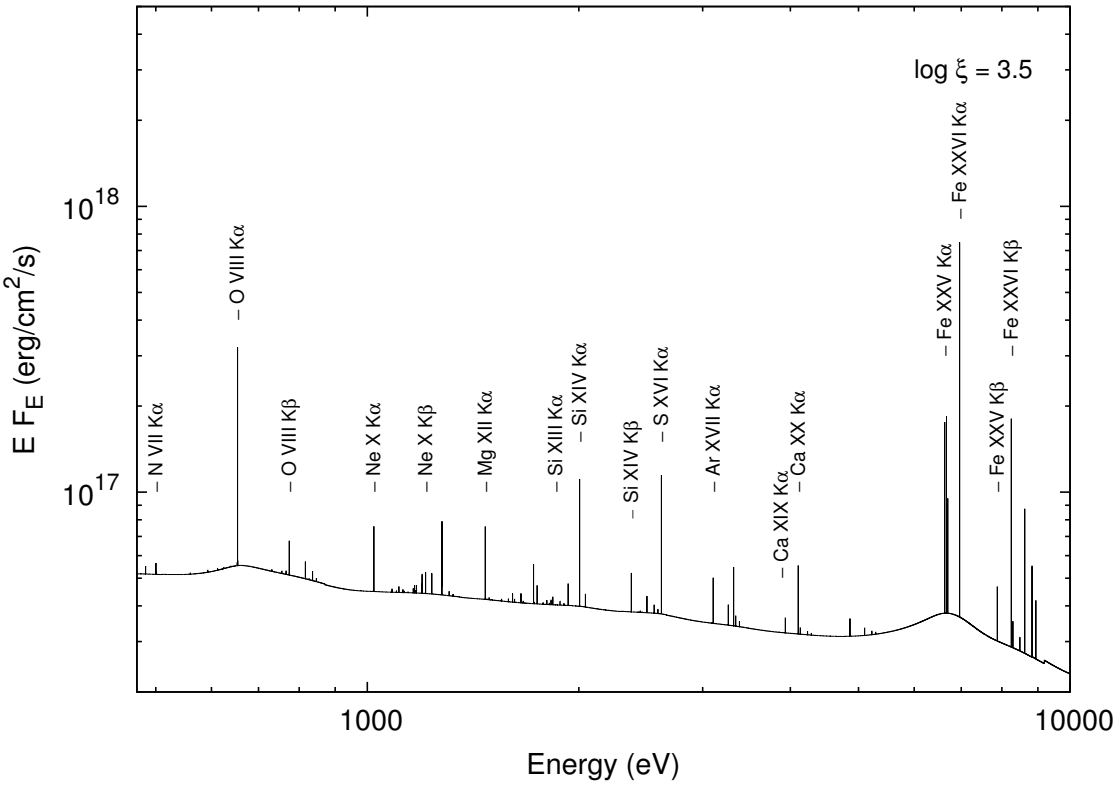

Figure 3.6 Reflected spectra for $\log \xi = 3.5$ while using a resolving power of $\mathcal{R} \sim 3500$ (model 13). All the other input parameters are the same used before (as in Figures 3.1 and 3.2), although no rescaling is applied. The strongest emission lines are labeled.

ions at ~ 6.7 keV. However, there is a rich structure of emission lines with centroid energies that cover from ~ 6.4 keV to 6.7 keV produced by ions at lower ionization stages (Fe XV-XVIII). The Fe XXVI Kα emission line is clearly observable at 6.965 keV. All these lines are superimposed on a very broad, Comptonized profile. The Kβ component is replaced by a few distinguishable emission lines mainly due to H- and He-like iron. As in the previous case, a rich structure of absorption profiles is noticeable between 7.2 and 8.2 keV. A small absorption edge can be seen just below the RRC located at ~ 9 keV.

It is important to notice that the O VIII Kα emission line shows the same kind of broadening as the Fe K line. In fact, the other oxygen lines also show broadening

in some degree, as well as those coming from neon. This is somewhat unexpected, since photons at those energies would need many scatterings in order to produce such broadening if the gas were cold. However, since the temperature is high ($T \sim 10^6$ °K) even at $\tau \sim 1$, broadening also takes place through the dependence of the Gaussian kernel on the temperature (see § 3.2.1). This also means that the H-like oxygen lines are being produced efficiently over a large range of optical depths, which can be verified by looking at higher ionization parameters. Figure 3.6 shows the last model with a resolving power of $\mathcal{R} \sim 3500$, resulting from a gas at $\log \xi = 3.5$ (model 13). Almost no absorption features can be seen in this spectrum, and the emission comes mostly from recombination of fully ionized ions. Both iron and oxygen Kα line profiles are very broad and Comptonized. There are no apparent signs of broad components in the weaker lines, such as those from neon, although this is likely due to the fact that the redistribution is so extreme that it completely smears the profile over the continuum. Therefore, only those photons produced very close to the surface come out of the slab unscattered. The emission in the iron K region is exclusively due to H- and He-like ions. There is strong emission from the Rydberg series of Fe XXV, namely transitions from 1s 4p, 5p and 6p to the ground state $1s^2$, at 8.62, 8.83 and 8.94 keV, respectively.

3.3.4 Anisotropy: incident and viewing angles

The boundary condition expressed in Equation (3.14) depends, in general, on the angle with respect to the normal on which the radiation is incident. Isotropic illumination implies that the source of radiation is extended and very close to the region where the calculation takes place. On the other hand, locating the source of the external X-rays at a specific point far away of the accretion disk constrains the angle at which radiation will penetrate in the atmosphere. To account for such a situation, the right hand side of Equation (3.14) can be expressed as

$$I_{inc} = I_0 \delta(\mu - \mu_0), \tag{3.36}$$

where μ_0 is the cosine of the incidence angle. The lower panel of Figure 3.7 shows the

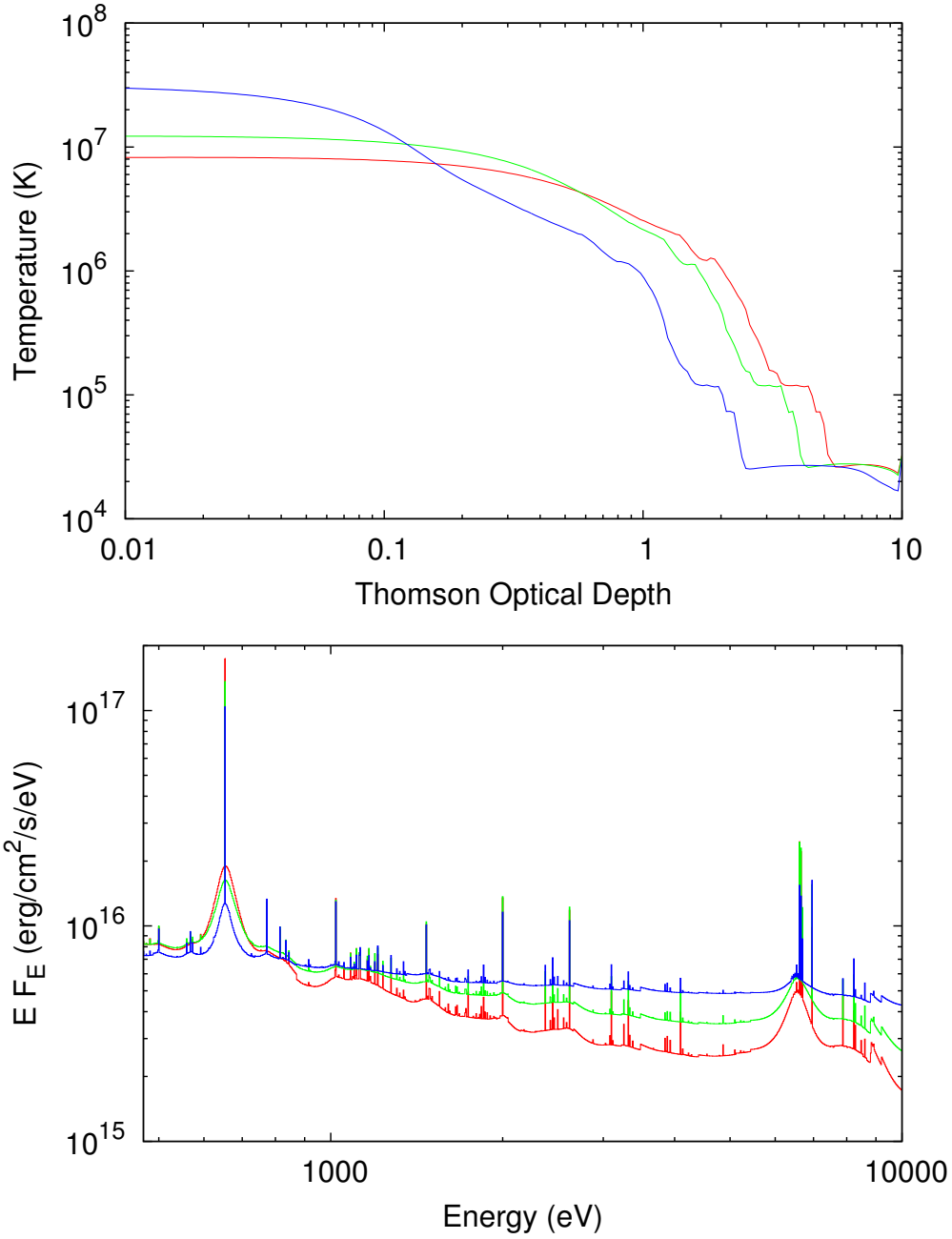

Figure 3.7 Temperature profiles (upper panel) and reflected spectra (lower panel), resulting from a constant density model with $\log \xi = 2.8$ for three different incidence angles (models 14-16). In the two panels, the *red* curves corresponds to $\mu_0 = 0.95$ ($\theta \approx 0^o$, normal incidence); the *green* curves to $\mu_0 = 0.5$ (or $\theta = 60^o$); and the *blue* to $\mu_0 = 0.05$ ($\theta \approx 90^o$, grazing incidence).

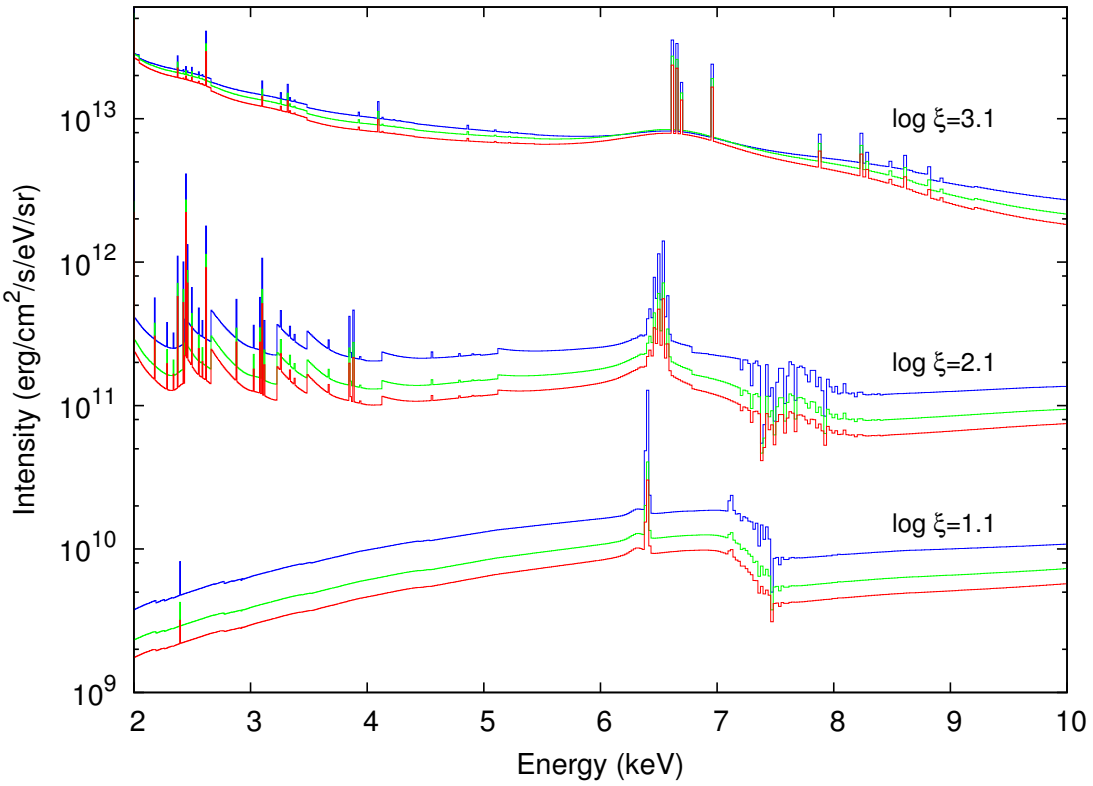

Figure 3.8 Outgoing intensities in the 2-10 keV energy range for constant density models from 3 different ionization parameters (models 2, 5 and 8), as viewed at three different angles with respect to the normal. In all cases, the red curves corresponds to $\mu = 0.95$, the green curves to $\mu = 0.5$, and the blue curves to $\mu = 0.05$.

reflected spectra for a constant density model in which $\log \xi = 2.8$ for three different incidence angles (models 14-16 in Table 3.1). The red curve corresponds to $\mu_0 = 0.95$ (normal incidence), the green curve corresponds to $\mu_0 = 0.5$, and the blue curve to $\mu_0 = 0.05$ (grazing incidence). The upper panel of the Figure shows the corresponding temperature profiles as a function of the Thomson optical depth, obtained for each case. At the surface of the disk ($\tau = 0$), the temperature increases with the incidence angle, such that the grazing incidence shows the highest temperature of the three cases. However, when the illumination occurs at normal incidence, the radiation ionizes deeper regions in the slab and there is a larger amount of hot material for those cases. In this model, the physical quantity that describes the amount of illumination is the net X-ray flux $F_{\rm x}$, in units of energy per unit area per unit of time. Since the flux is defined as the second moment of the intensity, (Equation 3.24), therefore $F_{\rm x} = \frac{1}{2}\int I_{inc}\mu d\mu$, and using Equation (3.36)

$$I_{inc} = \frac{2F_{\rm x}}{\mu_0}\delta(\mu - \mu_0), \tag{3.37}$$

which means that for the same value of $F_{\rm x}$ (or the same ionization parameter ξ), varying the incidence angle μ_0 effectively varies the intensity of the radiation incident at the surface. This will, of course, produce more heating and raise the temperature and ionization of the top layers in the disk. However, the angular dependence of the radiation field ensures that in the cases of normal incidence the illuminating radiation reaches deeper regions in the atmosphere than those of grazing angles, as is expected. Although the effects on the reflected spectra are not obvious, the spectrum for the grazing incidence (blue curve) is stronger than the other two, mimicking a case of a higher illumination (note that none of the curves have been offset). Nevertheless, the emission lines are, in general, very similar in all cases. It is also interesting to see how the temperature profiles of the three models converge at large optical depths, since the radiation fields become more isotropic after many scatterings.

The anisotropy of the reflected radiation field can also be investigated by looking its angular distribution through different viewing angles. Figure 3.8 contains the reflected spectra for 3 different ionization parameters (indicated next to each case), as

is observed from 3 different angles with respect to the normal, in the 2-10 keV energy range. For consistency the colors represent the same angles as in Figure 3.7, i.e., the red curves indicate $\mu = 0.95$ (face-on), the green curves $\mu = 0.5$, while the blue curves correspond to $\mu = 0.05$ (edge-on). Note that no rescaling or normalization is applied to these curves, therefore the differences are exclusively due to the differences in the ionizing fluxes and on the viewing angles. Moreover, the physical quantity plotted here is the outgoing specific intensity $I(0, +\mu, E)$ instead of the flux (as the other Figures), which is an angle averaged quantity. In fact, these 3 cases are those presented in Figures 3.2 and 3.3 (models 2, 5 and 8 in Table 3.1), and thus their temperature profiles correspond to those shown in Figure 3.1. In general, the reprocessed features are stronger when the disk is observed face-on than when the viewing angle is parallel to the surface. Nayakshin et al. (2000) found the same tendency in their hydrostatic models, which they explained to be a consequence of an effective Thomson depth that changes when the slab is observed at different angles, according to the geometrical projection $\tau_{eff} = \tau/\mu$. However, their results suggest that the reflection features almost disappear for small values of μ, and that no visible iron could been detected in such cases. The results shown in Figure 3.8 do not completely agree with this, since the Fe K lines are strong even for the high ionization case. Nevertheless, one must take this comparison with care, since all the results presented in this Chapter correspond to constant density models, while Nayakshin et al. (2000) calculations were done under hydrostatic equilibrium. In any case, the trend in the emerging spectra shown in Figures 3.7 and 3.8 is similar to previous models in the literature, such as those by Nayakshin et al. (2000) and Ballantyne et al. (2001).

3.3.5 Iron abundance

We have also studied the effects of the iron abundance on the ionization of the atmosphere and the reprocessed spectra. The upper panel of Figure 3.9 shows the temperature profiles along the vertical direction for a gas at $\log \xi = 2.5$ when the iron abundance is assumed to be 0.2, 1, 2, 5 and 10 times its solar value (models 17,

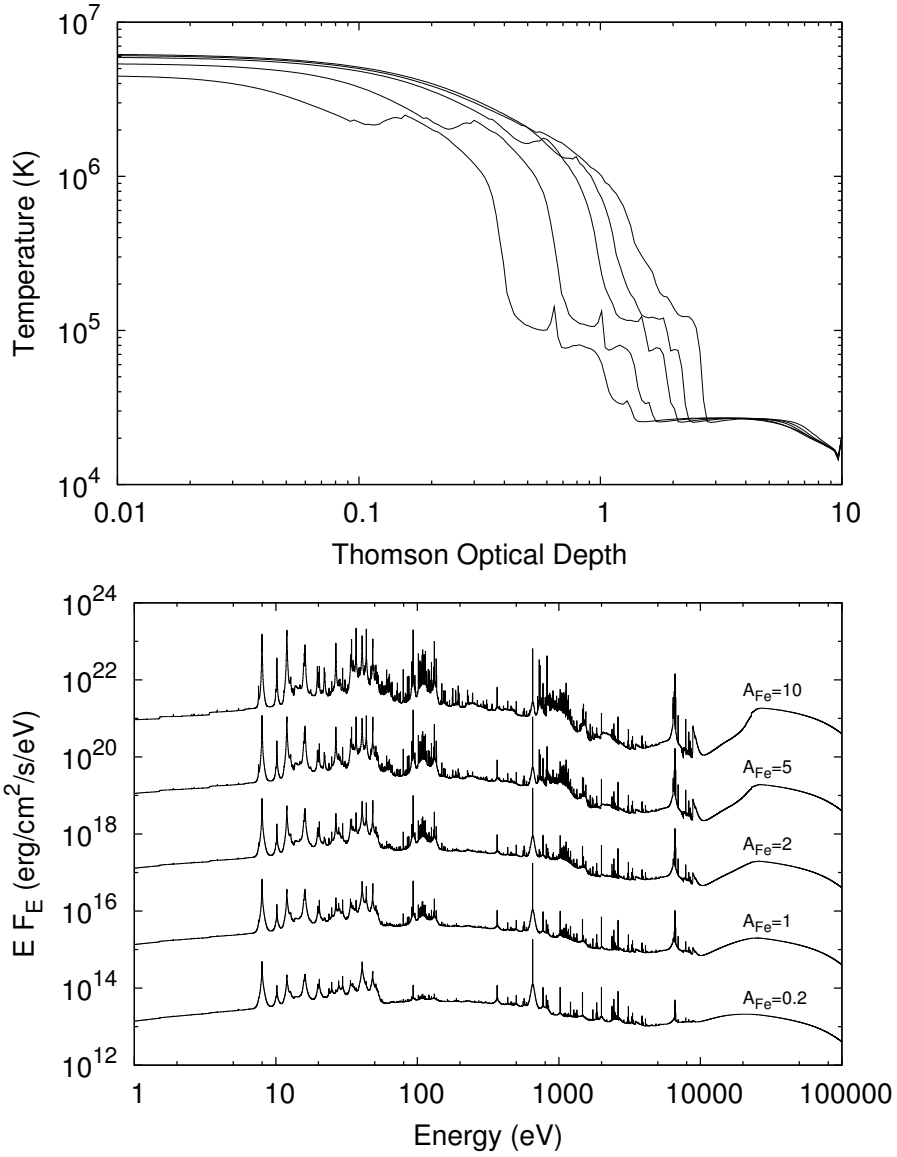

Figure 3.9 *Upper panel*: temperature profiles from a constant density model with $\log \xi = 2.5$ and different iron abundances with respect to the solar values. From right to left, each curve corresponds to: A_{Fe}=0.2, 1, 2, 5 and 10 (models 17, 6 and 18-20, respectively). *Lower panel*: reflected spectra for the same models. The curves are shifted by arbitrary factors for clarity. These factors are, from bottom to top: $10^{-2}, 10^{0}, 10^{2}, 10^{4}$, and 10^{6}. The values of the iron abundance with respect to the solar value are shown at the top of each curve.

6 and 18-20, respectively). The solar atomic abundances used in all our calculations are those from Grevesse et al. (1996), and in particular for iron is 3.16×10^{-5} (with respect to the hydrogen). The curves towards the left of the plot correspond to higher values of the iron abundance, which means that the gas is effectively cooler than the solar and sub-solar cases. This shows that the iron produces a net cooling as its abundance is increased. The transition between the hot and cold regions in the gas occurs at lower optical depths for the super-solar abundance models, decreasing the thickness of the hot skin. However, all the models converge to the same temperature in the cold region of the disk ($T \sim 2.5 \times 10^4$ °K).

The corresponding reflected spectra are shown in the lower panel of Figure 3.9. These curves are shifted by factors of $10^{-2}, 10^0, 10^2, 10^4$, and 10^6 from bottom to top for clarity. The iron emission is enhanced when the abundance is increased, as can be clearly seen at ~ 6 keV, ~ 1 keV and ~ 0.1 keV for the K-, L- and M-shell transitions, respectively. It is also evident that the continuum is highly modified in the 1-40 keV energy region, which is where the larger opacity takes place. However, there are no significant modifications at higher energies (i.e., if these spectra are placed on the top of each other, there are no differences in the region above 40 keV).

The suppression of the continuum combined with the enhancement of the K-shell emission lines, as the iron abundance is increased, shows a significant impact on the line equivalent width. When solar abundance is assumed, the equivalent width for the Fe Kα is ~ 700 eV. This value is increased to about 1.1, 2.3 and 3.9 keV when iron is chosen to be twice, five and ten times more abundant, respectively. Conversely, this value decreases to ~ 203 eV for the model when $A_{Fe} = 0.2$.

3.3.6 Comparison with previous models

Taking into account that our main contribution to the already existing models of accretion disk is the inclusion of the most complete atomic data available (particularly important for iron), we compare our results for constant density accretion disks models with those included in REFLION (Ross & Fabian, 2005). Such a comparison is shown

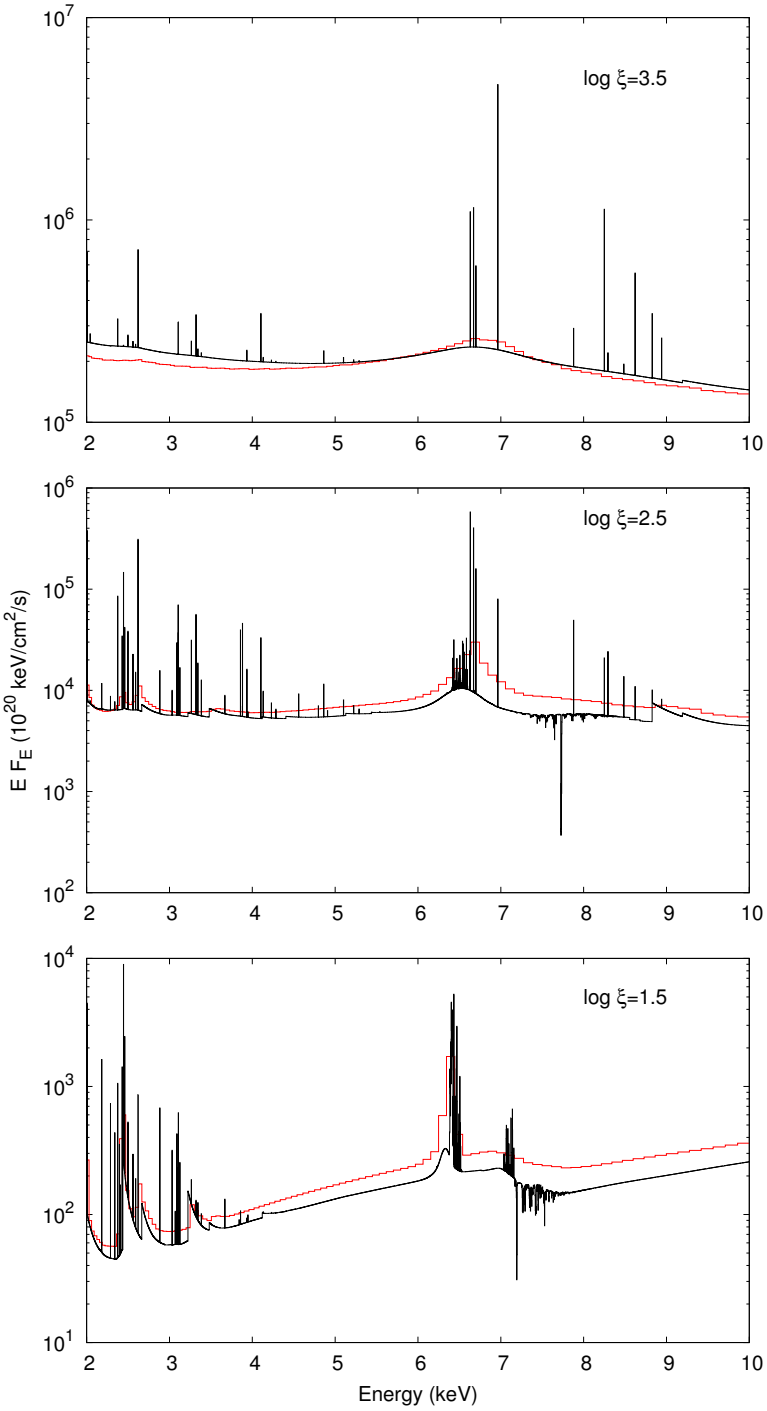

Figure 3.10 Reflected spectra from constant density models for three different ionization parameters (models 11-13), plotted in the 2-10 keV energy range. The red curves are the models from REFLION (Ross & Fabian, 2005), for the same input parameters.

in Figure 3.10 where the reflected spectra for three different ionization parameters are shown ($\log \xi = 1.5, 2.5$ and 3.5). In the figure, the black curves correspond to our calculations (models 11-13), while the red curves are the models from REFLION with the same input parameters. It is clear from this comparison that these two models show important differences. The Fe K line profile around 6.4 keV from our model is shown to be much more intense but with similar widths, and the absorption edge at $\sim$ 7.5 keV to be quite strong (especially for the lower ionization). In fact, the equivalent widths of the iron Kα emission line are similar in both models for $\log \xi = 1.5$, our models predict a value of 610 eV while REFLION predicts 793 eV. However, there are larger discrepancies in the higher ionization cases: our models predict equivalent widths of 695 eV and 92 eV for $\log \xi = 2.5$ and 3.5, respectively; while REFLION models show values of 473 eV and 49 eV for the same cases, respectively. As before, these equivalent widths were calculated using a local continuum which is defined by interpolating a straight line between two points. In this case the integration was performed between 6 and 7 keV in order to take into account only the contribution from the Kα emission (since any Fe Kβ emission will occur at energies above 7 keV). Furthermore, the same integration region is applied to all the models in order to provide a consistent quantity to compare models with different ionization parameters.

However, we have also calculated the equivalent widths when the integration region is modified for each model such that the entire broadened line is included. The new integration regions are: 6.1-6.6 keV, 5.9-7.3 keV, and 5.2-7.8 keV for models with $\log \xi = 1.5, 2.5$ and 3.5, respectively. The resulting equivalent withs from our models are 569 eV, 829 eV and 255 eV; while REFLION predicts 700 eV, 813 eV and 420 eV for the same models, respectively. Clearly, there is a better agreement when the entire line profile is taken into account, especially for the two lowest ionization cases. Although both set of models share the same input parameters, in REFLION the illuminating spectrum extends up to 1 MeV with an exponential cutoff placed at 300 keV, while our models cover up to 210 keV, with the exponential cutoff placed at 200 keV. This could be responsible for some of the differences seen here, in particular by altering the broad component of the Fe K emission which is highly affected by the Comptonization

of the photons in the gas. In general, our models predicts stronger Fe Kα emission, a more complex structure for the Fe absorption edge, and the presence of the Fe Kβ emission line at ~ 7.2 keV, not seen in the REFLION models.

Additionally, we have also compared our models with those presented by Nayakshin et al. (2000). In many aspects these models are the most similar to the ones presented in this Chapter, in particular since they have also used the code XSTAR to solve the ionization structure of the gas. By means of visual comparison of their figures we found a good general agreement in the five constant density models included in Nayakshin et al. (2000). However, our models predict higher temperatures in the regions close to the surface of the disk (at small optical depths), and lower temperatures at large optical depths; which affects the ionization of the gas and the final reprocessed spectrum. This is likely due to the fact that their models only explicitly treat a smaller optical depth (up to $\tau_{\rm Thomson} = 4$) than ours, and the radiation transmitted through this region is treated approximately.

3.4 Conclusions

In this Chapter we have presented new models for the structure of X-ray illuminated accretion disks and their reflected spectra, assuming constant density along the vertical direction. These models include the most recent and complete atomic data for the iron isonuclear sequence. The energy resolution used in the reflected spectra exceeds other models previously published as well as the resolution of the detectors on current X-ray observatories (*Chandra*, *XMM Newton, Suzaku*), and it is comparable to the expected resolving powers of the forthcoming X-ray missions such as *Astro-H*.

In models with intermediate values of the ionization parameter ($1.5 \leq \log\xi \leq 3.1$), the structure of the gas often displays a two temperature regime: a hot skin ($T > 10^6$ °K) close to the surface where the Compton heating and cooling dominates, and a cold region ($T < 10^5$ °K) where the photoelectric opacity quickly thermalizes the radiation fields. The thickness of the hot skin increases with the illumination. Although these solutions are thermally stable, the transition between the hot and cold

regions can be sudden. The emergent spectra corresponding to these models show a clear combination of absorption and emission features, particularly for $\log \xi < 2.5$. For higher illumination cases the effects of Compton scattering become more evident, even in the low-energy part of the spectrum ($E < 100$ eV). In the high energy part of the spectrum Compton scattering partially smears the profile of the iron K line. The Compton hump above 10 keV is clearly visible in all the models considered here.

The equivalent width of the Fe Kα emission line varies between $\sim$ 400-800 eV for models with $1 \lesssim \log\xi \lesssim 3$. Once the ionization parameter is larger than 10^3, the equivalent width decreases drastically. The lowest value of the equivalent width is $\sim$ 20 eV, corresponding to the highest illumination case ($\log \xi = 3.8$). This behavior resembles the X-ray Baldwin effect, recently observed in several AGNs. A comparison with other models previously published such as REFLION shows important differences in the structure of the iron K lines. In particular, the equivalent widths in those models can differ by a factor of 2 when compared to the ones shown in this Chapter.

In general, our simulations show that the K-shell atomic data is crucial to properly model the structure and profile of the iron lines. These results also suggest that the line emission from Fe ions in different ionization stages and Comptonization of high energy photons by cold electrons can be responsible for significant line broadening. These processes need to be taken into account since they can be mistaken for relativistic effects, especially in cases when the gas is partially or high ionized.

4

Theory of The Atomic Structure

4.1 Introduction

Both modern quantum mechanics and computational physics have been crucial in the development of the necessary tools for the calculation of the atomic structure of many elements, with an accuracy that, in many cases, is comparable to laboratory measurements. In this chapter we present a review of the methodology used in the calculation of atomic data for the isonuclear sequence of nitrogen, namely energy levels, wavelengths, partial and total radiative and Auger rates, and photoionization cross sections. Each theoretical framework is related to different computer codes in the public domain, such as AUTOSTRUCTURE, HFR and BPRM. Although these share the same final purpose, they differ in terms of the numerical techniques and minor physical aspects. These could yield to significant differences in the final result. The relevance of using different techniques lies in the possibility of a detailed comparison of each one of the physical quantities computed, as well as the identification of the relevance of small corrections introduced by each approximation.

4.2 AUTOSTRUCTURE

The computer code AUTOSTRUCTURE (Eissner et al., 1974; Badnell, 1986, 1997, previously called SUPERSTRUCTURE), is a tool for the calculation of the atomic structure of a given ion. It has been defined by its authors as "an automatic computational program of general purposes", which means that, in principle, its capabilities do not depend on the particular ion to be studied, and that its implementation is more automatized since the information required from the user in minimal. This code allows the calculation of energy terms in LS coupling, energy levels in intermediate coupling, radiative and Auger data and wavelengths.

Its main feature is the use of the Slater method as a expansion technique to generate the eigenfunctions of the angular momentum operators L^2, L_z, S^2 and S_z, described in detail by Condon & Shortley (1951). Other important features are:

- The algebraic and analytic problems are treated separately inside the code, which represent a huge advantage in the study of isonuclear sequences: the algebra is calculated only once, while the analytic part calculates the radial wave functions, energies and other quantities for each member of the sequence.

- There is flexibility in the type of radial wave functions that can be used, which can be provided by the user, or calculated internally using a modified Thomas–Fermi potential.

- It is capable of processing dipolar transition probabilities in order to obtain cascade coefficients.

With these features, AUTOSTRUCTURE makes use of the eigenfunctions mentioned above to calculate the matrix elements of the non-relativistic Hamiltonian, the Breit–Pauli relativistic operators and the electric dipolar and magnetic quadrupolar radiative operators.

4.2.1 Energy Levels

The quantum mechanical description of any atom or ion requires the solution of the Schrodinger wave equation. For a many body system in steady state it can be written as

$$H\Psi = E\Psi \tag{4.1}$$

where E is the total energy, H is the Hamiltonian operator and Ψ is the wave function that describes the system. For an ion with N electrons the non-relativistic Hamiltonian is given by

$$H_{nr} = -\sum_{i=1}^{N}\left(\nabla_i^2 + \frac{2Z}{r_i}\right) + \sum_{i>j}\frac{2}{r_{ij}} \tag{4.2}$$

with energies in Rydberg. This expression assumes that the nucleus can be treated as a point charge; Z is the atomic number, r_i is the distance of the i-th electron from the nucleus, and r_{ij} is the distance between the i-th and j-th electrons. An exact solution of Equation (4.1) only can be found for systems with one electron, such as the hydrogen atom ($N = 1$). Nonetheless, it is possible to obtain an approximate wavefunction by replacing the Hamiltonian in Equation (4.2), by one that can be solved. As a first approximation an independent model of particles can be adopted

$$H_{nr} \approx H_o = \sum_{i=1}^{N}\left\{-\nabla_i^2 - \frac{2Z}{r_i} + U_i\right\} \tag{4.3}$$

If a wavefunction Φ satisfies the new wave equation

$$H_o\Phi = E_o\Phi \tag{4.4}$$

it means that Φ is an approximation of Ψ, with the difference that the new function can be rewritten as a combination of independent functions as

$$\Phi = \varphi(1)\varphi(2)...\varphi(i)...\varphi_N \tag{4.5}$$

where $\varphi(i)$ is the wavefunction of the i-th electron. Therefore, Equation (4.4) becomes

$$\left[-\nabla_i^2 - \frac{2Z}{r_i} + U_i\right]\varphi(i) = E_{oi}\varphi(i) \tag{4.6}$$

As a second approximation we can assume that U_i is a central potential, from where Equation (4.6) can be separated as combination of functions depending on the angular, radial and spin coordinates

$$\varphi(r,\theta,\phi,\sigma) = \frac{P(r)}{r} Y_{lm_l}(\theta,\phi)\chi_{m_s} \tag{4.7}$$

where $Y_{lm_l}(\theta,\phi)$ is the spherical harmonic and χ_{m_s} is the spin function. The radial function $P(r)$ is now a solution of the equation

$$\left[\frac{d^2}{dr^2} + \frac{2Z}{r} - U(r) - \frac{l(l+1)}{r^2} + \epsilon\right] P(r) = 0, (\epsilon = E_{oi}) \tag{4.8}$$

with the boundary conditions $P(0) = P(\infty) = 0$. Then, we have an eigenvalue problem, where the eigenvalues and eigenvectors are ϵ_{nl} and P_{nl}, respectively, and n plays the same role as the principal quantum number in the equation for the hydrogen atom. As a result, the functions for one electron can be completely specified in terms of the four quantum numbers n, l, m_l, m_s, which are called *orbital-spin functions*. In this approximation, the total wave function describes a configuration of electrons in which the quantum numbers n and l are specified for each electron (even though the wave functions are still degenerate with respect to m_l and m_s). The difficulty of this scheme lies in choosing a potential $U(r)$ also approximated for one electron.

The function (4.5) does not ensure Pauli's exclusion principle. However it can be satisfied if we make Φ take the form of a *Slater determinant* of the orbital-spin functions. It is convenient that the orbital-spin functions form an orthonormal set

$$\int \varphi^{(1)}_{nlm_lm_s} \varphi^{(1)}_{n'l'm'_lm'_s} d\tau_1 = \delta_{nn'}\delta_{ll'}\delta_{m_sm'_s}\delta_{m_lm'_l} \tag{4.9}$$

where $d\tau_1$ means that the integration is over the whole space and that the sum is performed over all the spin coordinates of electron 1. Since the Hamiltonian is independent of the spin, it must commute with the total spin angular momentum operators S^2 and S_z, as well as with the total orbital angular momentum operators L^2 and L_z, which also commute with the previous two. This means that the exact solution of Equation (4.1) is also an eigenfunction of these operators. Therefore the

approximated wave functions are taken as linear combinations of the Slater determinants coupled to produce the eigenfunctions of the four operators mentioned above. In the scheme of the Russell–Saunders coupling (LS coupling), the spin and orbital angular momentum are coupled independently in order to produce the $\mid LSM_LM_S\rangle$ states. Clearly, it is advantageous to use LS coupling in systems where the spin-orbit effects are negligible.

4.2.2 Variational Principle in the Calculation of Energy Levels

Each configuration C used in the expansion in AUTOSTRUCTURE will produce a set of terms t where

$$t = C\beta SL \tag{4.10}$$

and β a degeneration parameter. The wave function of a particular state is then given by a linear combination of the wave functions of the configuration

$$\mid \gamma SLM_SM_L\rangle = \langle C\beta SL \mid \gamma SL\rangle \mid C\beta SLM_SM_L\rangle \tag{4.11}$$

To calculate the matrix elements, the wave functions are expressed in terms of the Slater states

$$\mid t\rangle = \langle u \mid t\rangle \mid u\rangle \tag{4.12}$$

where

$$\mid u\rangle = \pi_{g=1}^{N} \mid n_g l_g \mu_g m_g\rangle \tag{4.13}$$

and

$$M_S = \sum_{g=1}^{N} \mu_g \tag{4.14}$$

$$M_L = \sum_{g=1}^{N} m_g \quad . \tag{4.15}$$

Thus, each matrix element is calculated in the representation of the Slater states and then transformed to the representation of the configurations t

$$\langle t \mid H \mid t' \rangle = \langle t \mid u \rangle \langle u \mid H \mid u' \rangle \langle u' \mid t' \rangle \quad . \tag{4.16}$$

The coefficients of the coupled vectors $\langle u \mid t \rangle$ are obtained by looking at which combinations of the Slater states are eigenvectors of S^2 and L^2 simultaneously, and then diagonalizing the S^2 and L^2 matrices.

The radial wave functions can be obtained with the functional of the well known variational principle

$$\delta \left\{ \langle t \mid H - E \mid t' \rangle \right\} = 0 \tag{4.17}$$

where t and t' are the trial functions. The radial functions P_{nl} are solutions of the equation

$$\left\{ \frac{d^2}{dr^2} - \frac{l(l+1)}{r^2} + 2V(\lambda_l, r) + \epsilon_{nl} \right\} P_{nl}(r) = 0 \tag{4.18}$$

under the boundary conditions $r \to 0$ and $r \to \infty$. The potential $V(\lambda_l, r)$ is of the type of the Thomas–Fermi statistical model, and the functions P_{nl} depend on the scaling parameters λ_l, which are considered as variational parameters. Thus,

$$E_i = E_i(\lambda_s, \lambda_p, ...) = \langle \gamma SL \mid H \mid \gamma SL \rangle \tag{4.19}$$

replacing Equation (4.17) by

$$\delta F = \delta \left\{ \sum_{i=1}^{INC} g_i E_i(\lambda_s, \lambda_p, ...) \right\} \tag{4.20}$$

where g_i is the statistical weight of the i term, and INC is the number of energies included in the minimization process.

4.2.3 Relativistic Corrections to the Hamiltonian

The relativistic effects usually have a small impact on the calculation. However, if high accuracy is desired, they might be quite relevant, in particular for ions with high

atomic number, or highly ionized species where high velocities are involved. Historically, the first relativistic approximation to the Schrodinger equation was proposed by Klein–Gordon. However this only admits solutions in which the probability density is negative, thus lacking physical meaning. Later, Paul Dirac found the proper relativistic wave equation that solved these type of problems. The solution of the Dirac equation represents the most correct way of including relativistic corrections in atomic calculations. Dirac's deduction was made for one electron systems only. In the case of many bodies, the solution of the Dirac equation is extremely difficult and cumbersome. Therefore, in practice (and specifically in AUTOSTRUCTURE), lower order operators are introduced to complement the Hamiltonian described before, which are obtained through expansions of powers of α, the fine-structure constant. The resulting Hamiltonian is known as the relativistic Breit–Pauli Hamiltonian (Breit, 1932), and can be expressed as

$$H_{\rm bp} = H_{\rm nr} + H_{\rm 1b} + H_{\rm 2b} \tag{4.21}$$

where $H_{\rm nr}$ is the one showed in Equation (4.2), and $H_{\rm 1b}$ and $H_{\rm 2b}$ are the operators associated with the one or two body interactions, respectively. Each one of them contains a different kind of correction, namely

$$H_{\rm 1b} = \sum_{i=1}^{N} f_i({\rm mass}) + f_i({\rm d}) + f_i({\rm so}) \tag{4.22}$$

$$H_{\rm 2b} = \sum_{i>j} g_{ij}({\rm so}) + g_{ij}({\rm ss}) + g_{ij}({\rm css}) + g_{ij}({\rm d}) + g_{ij}({\rm oo}) \tag{4.23}$$

1. **1-Body Operators**

   The 1-body mass correction operator,

   $$f_i({\rm mass}) = -\frac{1}{4}\alpha^2\nabla_i^4 \tag{4.24}$$

   represents the term for the correction in the kinetic energy of the electron due to the variation of its mass as a function of the velocity.

The 1-body Darwin operator,

$$f_i(\mathrm{d}) = -\frac{1}{4} Z\alpha^2 \nabla_i^2 \frac{1}{r_i} \tag{4.25}$$

corresponds to the relativistic correction for the potential energy.

The spin-orbit 1-body operator

$$f_i(\mathrm{so}) = \frac{Z\alpha^2}{r_i^3}(l_i.s_i) \tag{4.26}$$

corresponds to the interaction of the intrinsic magnetic moment of the electron with the magnetic field produced by its orbit around the nucleus.

2. **2-Body Operators**

The fine-structure 2-body spin-orbit operator

$$g_{ij}(\mathrm{so}) = -\alpha^2 \left(\frac{r_{ij}}{r_{ij}^3} \times p_i \right) \cdot (s_i + 2s_j) \tag{4.27}$$

considers the interaction of the electron spin with the orbit of another electron, and the contribution of its own spin-orbit interaction. Other operators are:

The spin-spin operator is

$$g_{ij}(\mathrm{ss}) = 2\alpha^2 \frac{1}{r_{ij}^3} \left(s_i s_j - \frac{3(s_i.r_{ij})(s_j.r_{ij})}{r_{ij}^2} \right) \quad ; \tag{4.28}$$

The contact spin-spin operator

$$g_{ij}(\mathrm{css}) = -\frac{16\pi\alpha^2}{3}(s_i.s_j)\delta^3(r_{ij}) \quad ; \tag{4.29}$$

The 2-body Darwin operator

$$g_{ij}(\mathrm{d}) = -\frac{1}{2}\alpha^2 \nabla^2 \left(\frac{1}{r_{ij}} \right) \quad ; \tag{4.30}$$

and the orbit-orbit operator between valence electrons

$$g_{ij}(\mathrm{oo}) = -\alpha^2 \left(\frac{P_i.P_j}{r_{ij}} + \frac{r_{ij}(r_{ij}.P_i).P_j}{r_{ij}^2} \right) \quad . \tag{4.31}$$

4.2.4 Photoionization Cross Sections

Consider the photoionization process

$$h\nu + A_i \rightarrow A_j^+ + e^- \tag{4.32}$$

where A_i is an atom in the state i and A_j^+ is the residual ion in the state j. The total cross section of the emission of electrons in any direction due to the absorption of a photon with energy $h\nu$ (from an unpolarized beam), is given by

$$\sigma_{ji}(\nu) = \frac{8\pi^3\nu}{3c}\frac{1}{g_i}S_{ji} \tag{4.33}$$

where S_{ji} is the line strength and g_i is the statistical weight if the initial state. It is important to notice that when considering an atomic system as $A^+ + e^-$, the initial state i correspond to the bound state and the final state j correspond to the free state. The wave function of the bound state is normalized to unity, while the normalization of the final state (or state of the continuum), is defined as

$$\langle \Psi_j \mid \Psi_{j'} \rangle = \delta_{jj'}\delta(E - E') \quad . \tag{4.34}$$

When using Rydberg as energy unit, Equation (4.33) is transform to

$$\sigma ji(\mu) = \frac{4\pi^2\alpha a_0^2}{3}(I_i + E_j)\frac{1}{g_i}S_{ji} \tag{4.35}$$

where I_i is the ionization threshold energy and E_j is the kinetic energy of the excited electron.

4.3 X-ray Fluorescence lines

In accretion discs around black holes reprocessing of a hard X-ray continuum in relatively cool matter ($\sim 10^5 - 10^6$ K) and can generate intense iron K radiation from less ionized iron. Iron fluorescence can be quite prominent and has long been known to constitute an essential component of the disk spectra.

The reprocessing mechanism, for any species with more than two electrons, begins with the photoionization of a 1s electron by a photon with energy ϵ above the K edge, sending an element A in charge state $i-1$, to charge state i, where i is in a quasi bound state that is coupled to the continuum, denoted here with a double asterisk

$$\epsilon + A_{i-1} \rightarrow A_i^{**} + e^- \tag{4.36}$$

The intermediate state A_i^{**}, since it lies above the threshold, has a non-vanishing probability to react

$$A_i^{**} \rightarrow A_{i+1} + e^- \tag{4.37}$$

The ejection of an electron by this mechanism is called *Autoionization*. Referred also as *Auger effect* for 1s vacancy states, autoionization is often the dominant decay route for the 1s-hole state. The reaction products are *Auger electrons*; i.e., an electron with a kinetic energy that is characteristic of the atomic energy level structure, and an ion in charge state $i+1$, which can be excited or at its ground state. For iron, autoionization rates $\sim 10^{12} - 10^{14}$ s^{-1} are typical (Kallman et al., 2004). Competing with the autoionization of the state A_i^{**} is spontaneous radiative decay. Radiative transitions rates are of the same order of magnitude as Auger rates in iron, but can be smaller by factors of a few. The case of highest probability involves a radiative transition that fills the K-shell hole. The line energy ϵ_K is characteristic of the atomic structure of the ion. We write the reaction as

$$A_i^{**} \rightarrow A_i^{*} + \epsilon_K \tag{4.38}$$

The resulting ion A_i^* is indicated as being an excited level, although there are cases when it is a ground level. Transitions filling the K-hole, from $n = 2$ are referred to as $K\alpha$ transitions, and from $n = 3$, $K\beta$ transitions. These processes are shown schematically in Figure (4.1).

These two processes together, the photoionization followed by radiative emission of a K photon, make up what is called *inner fluorescence*. The K *fluorescence yield* Y_K is the quotient if the rate at which K lines are generated from an irradiated sample

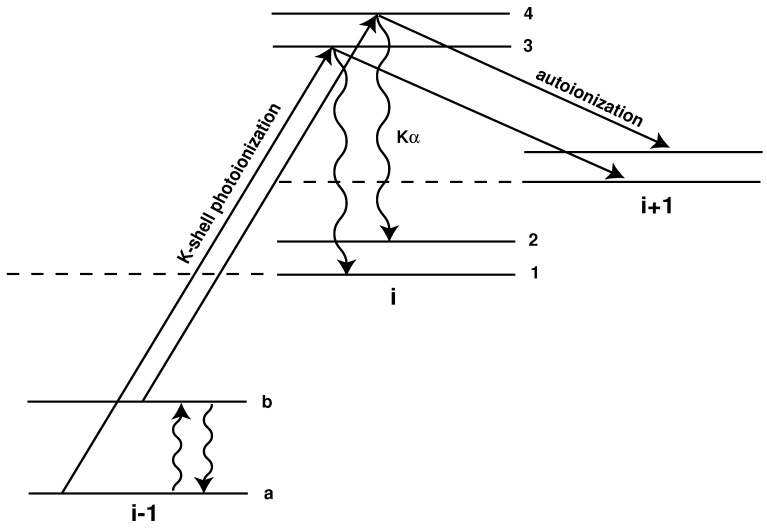

Figure 4.1 Schematic view of atomic processes involved in the production of iron K-spectra.

and the rate at which K-shell holes are produced in the sample (Bambynek et al., 1972). The usual convention is to associate a fluorescence yield with pre-ionization charge state. For example, Fe II K lines are associated with a Fe I yield.

For a set of energy levels u that lie above the ionization threshold, and a set of stabilized levels l, all of which belong the charge state i (See Figure 4.1), the emissivity summed over all K lines is

$$j_K = \sum_u \sum_l n_{i,u} A^r_{ul} \tag{4.39}$$

where we assume that transitions $u \rightarrow l$ are members of the $K\alpha$ complex in i. Level population densities of level u in charge state i are denoted $n_{i,u}$, and radiative transition rates by A^r. The units are cm^{-3} s^{-1}. The level population density is found by dividing the population flux into level u by the total decay rate of the level

$$n_{i,u} = \frac{\sum_k n_{i-1,k} \beta_{ku}}{\sum_j A^r_{uj} + \sum_m A^a_{um}} \tag{4.40}$$

where A^a_{um} is the Auger rate connecting level u in state i to level m in state $i+1$.

Energy levels k in the pre-ionization charge state $i-1$ are represented as $n_{i-1,k}$, and β_{ku} is the photoionization rate connecting level k in state $i-1$ with autoionizing levels u in state i. The the emissivity becomes

$$j_K = \sum_k \sum_u \sum_l n_{i-1,k} \beta_{ku} \Gamma_{ul} \tag{4.41}$$

where we define the *line fluorescence yield* Γ_{ul} for each transition $u \rightarrow l$ by

$$\Gamma_{ul} = \frac{A^r_{ul}}{\sum_j A^r_{uj} + \sum_m A^a_{um}} \tag{4.42}$$

Now we normalize the emissivity by dividing it by the total photoionization rate, which gives an expression for the *fluorescence yield*

$$Y_K = \frac{\sum_k \sum_u \sum_l n_{i-1,k} \beta_{ku} \Gamma_{ul}}{\sum_k \sum_u n_{i-1,k} \beta_{ku}} \tag{4.43}$$

Then the yield $Y_{K\alpha}$ is thus a weighted average of the line fluorescence yields, where the weightings are determined by the level population distribution of charge state $i-1$ and the level-to-level photoionization rates.

5

Nitrogen K-shell photoabsorption

5.1 Introduction

The improved resolution and sensitivity of current satellite-borne X-ray observatories (*Chandra* and *XMM Newton*) allow the study of previously inaccessible weak spectral features of astrophysical interest. In the early stages of these missions, it was realized that absorption by low-ionization species was common. Additionally, all charge states (except the fully ionized) left identifiable imprints in the X-ray spectrum proved to be a powerful diagnostic. Inner-shell absorption is important in the outflows of Seyfert galaxies in terms of both Fe Lα (Sako et al., 2001; Behar et al., 2001) and Kα lines of high-Z elements (Behar & Netzer, 2002), and also of elements in the first row of the periodic table such as oxygen (Pradhan, 2000; Behar et al., 2003; García et al., 2005). Furthermore, inner-shell absorption of continuum X-rays from bright galactic sources is a useful diagnostic of the interstellar medium (Yao et al., 2009; Kaastra et al., 2009).

Nitrogen K-shell absorption and emission are detected in X-ray spectra, mostly due to the H- and He-like charge states. For instance, observations of the emission lines of N VI and N VII in the ejecta of η Carinae by Leutenegger et al. (2003) have resulted in the lower bound N/O > 9 for its nitrogen abundance. This result puts a constraint in the evolution of η Car and is a signature of CNO-cycle processing.

The N VI triplet is observed in the spectrum of the magnetic B star β Cep where it has been used to test magnetically confined wind shock models (Favata et al., 2009). It is found that the plasma is not heated by magnetic reconnection and there is no evidence for an optically thick disk at the magnetic equator. Highly ionized emission lines of nitrogen have been observed by Miyata et al. (2008) on the north-eastern rim of the Cygnus Loop supernova remnant which can be used to determine nitrogen abundances, which turn out to be 23% solar. Seyfert galaxy outflows may also have super-solar N abundances (Brinkman et al., 2002; Arav et al., 2007).

Narrow absorption Kα and Kβ lines of N VI have been identified in the warm absorber of the MR 2251-178 quasar, which point to a complex velocity field with an outflow of ionized material (Ramírez et al., 2008). K-shell absorption by Li-like N V, which has prominent UV lines, or by lower charge states at wavelengths $\lambda > 29$ Å is difficult to detect due to the reduced sensitivity of current X-ray instruments towards these longer wavelengths. Notable exceptions include : Kα absorption by N V at 29.42 Å has been reported by Steenbrugge et al. (2005) in the outflow of NGC 5548; and N absorption by a white dwarf outflow has been observed following the outburst of nova V4743 Sagittarii (Ness et al., 2003). In the latter case, only the H- and He-lines are discussed, but lower charge states of N are clearly seen in the spectrum longward of 29 Å (see Fig. 3b in Ness et al., 2003).

The current proliferation of X-ray spectra with high signal-to-noise ratio in astronomical archives makes the computation of nitrogen K-shell photoabsorption particularly timely. This is also an additional and important step in the ongoing effort to compute reliable atomic data by García et al. (2005); Palmeri et al. (2008a,b); Witthoeft et al. (2009) for K-line analysis within the context of the XSTAR spectral modeling code (Kallman & Bautista, 2001). Available spectroscopic data for K-vacancy levels of the N isonuclear sequence are notably scarce, mainly limited to N V and N VI for which a few levels are listed in the NIST database (Ralchenko et al., 2008) and four measured wavelengths have been reported by Beiersdorfer et al. (1999). This shortage of reliable measurements precludes empirical corrections to calculated level energies. On the other hand, several relativistic methods have been

previously used to generate atomic data for nitrogen K-vacancy states: the saddle-point complex-rotation method (Davis & Chung, 1989; Chung, 1990; Shiu et al., 2001; Lin et al., 2001, 2002; Zhang et al., 2005); the Raleigh–Ritz variational method (Hsu et al., 1991; Yang & Chung, 1995; Wang & Gou, 2006); and multiconfiguration Dirac–Fock (MCDF) approaches such as those by Hata & Grant (1983); Hardis et al. (1984); Chen (1986); Chen & Crasemann (1987, 1988); Chen et al. (1997). Photoabsorption cross sections in the near K-edge region of N ions have been obtained by Hartree–Slater central-field computations (Reilman & Manson, 1979), where the resonance structure due to quasibound states as well as configuration correlations are neglected. The net effect of the resonance structure is to fill in the photoionization cross section below the inner-shell threshold altering the shape of the K edge.

In this chapter we report on calculations of energy level structure and bound-bound and bound-free transition probabilities for the K-shell of nitrogen. The outline of the present chapter is as follows. The numerical methods are briefly described in Section 5.2 while an analysis of the results based on comparisons with previous experimental and theoretical values is carried out in Section 5.3. Some conclusions are discussed in Section 5.4.

5.2 Numerical methods

The numerical approach used here has been fully described in Bautista et al. (2003). Level energies, wavelengths, A-coefficients, and radiative and Auger rates are computed with the codes AUTOSTRUCTURE (Eissner et al., 1974; Badnell, 1986, 1997) and HFR (Cowan, 1981). For consistency, configuration-interaction (CI) wave functions of the type

$$\Psi = \sum c_i \phi_i \tag{5.1}$$

are calculated with the relativistic Breit–Pauli Hamiltonian

$$H_{\rm bp} = H_{\rm nr} + H_{\rm 1b} + H_{\rm 2b} \tag{5.2}$$

where $H_{\rm nr}$ is the usual non-relativistic Hamiltonian. The one-body relativistic operators

$$H_{\rm 1b} = \sum_{n=1}^{N} f_n({\rm mass}) + f_n({\rm d}) + f_n({\rm so}) \tag{5.3}$$

represent the spin–orbit interaction, $f_n({\rm so})$, the non-fine-structure mass variation, $f_n({\rm mass})$, and the one-body Darwin correction, $f_n({\rm d})$. The two-body Breit operators are given by

$$H_{\rm 2b} = \sum_{n<m} g_{nm}({\rm so}) + g_{nm}({\rm ss}) + g_{nm}({\rm css}) + g_{nm}({\rm d}) + g_{nm}({\rm oo}) \tag{5.4}$$

where the fine-structure terms are $g_{nm}(so)$ (spin–other-orbit and mutual spin-orbit), $g_{nm}(ss)$ (spin–spin), and the non-fine-structure counterparts $g_{nm}(css)$ (spin–spin contact), $g_{nm}(d)$ (two-body Darwin), and $g_{nm}(oo)$ (orbit–orbit). It must be pointed out that HFR neglects contributions from the two-body term $H_{\rm 2b}$ of Equation (5.4).

In HFR, core-relaxation effects (CRE) are always taken into account since each electron configuration is represented with its own set of non-orthogonal orbitals optimized by minimizing the average configuration energy. In AUTOSTRUCTURE, on the other hand, configurations may be represented with either orthogonal or non-orthogonal orbitals which then enables estimates of the importance these effects. In the present calculation five approximations are considered in order to study the effects of electron correlation, i.e. configuration interaction (CI) and CRE, and thus to estimate data accuracy.

Approximation AS1 Atomic data are computed with AUTOSTRUCTURE including CI from only the $n = 2$ complex. CRE are neglected.

Approximation AS2 Atomic data are computed with AUTOSTRUCTURE including both $n = 2$ CI and CRE.

Approximation AS3 Atomic data are computed with AUTOSTRUCTURE including CI from both the $n = 2$ and $n = 3$ complexes. CRE are neglected.

Approximation HF1 Atomic data are computed with HFR including CI only from the $n = 2$ complex.

Approximation HF2 Atomic data are computed with HFR including CI from both the $n = 2$ and $n = 3$ complexes.

Photoabsorption cross sections are obtained with the codes Breit-Pauli R-Matrix BPRM (Berrington et al., 1987; Seaton, 1987) and HULLAC (Hebrew University Lawrence Livermore Atomic Code, Bar-Shalom et al., 2001). In BPRM, wave functions for states of an N-electron target and a colliding electron with total angular momentum and parity $J\pi$ are expanded in terms of the target eigenfunctions

$$\Psi^{J\pi} = \mathcal{A} \sum_i \chi_i \frac{F_i(r)}{r} + \sum_j c_j \Phi_j \ . \tag{5.5}$$

The χ_i functions are vector coupled products of the target eigenfunctions and the angular components of the incident-electron functions; $F_i(r)$ are the radial part of the continuum wave functions that describe the motion of the scattered electron; and $\mathcal{A}$ is an antisymmetrization operator. The functions Φ_j are bound-type functions of the total system constructed with target orbitals. The Breit–Pauli relativistic version has been developed by Scott & Burke (1980) and Scott & Taylor (1982), but the inclusion of the two-body terms (see Equation 5.4) is currently in progress, and thus not included. Auger and radiative damping are taken into account by means of an optical potential (Robicheaux et al., 1995; Gorczyca & Badnell, 1996; Gorczyca & McLaughlin, 2000) where the resonance energy with respect to the threshold acquires an imaginary component. In the present work, the N-electron targets are represented with all the fine structure levels within the $n = 2$ complex. It is important to mention that the BPRM approach does not allow the inclusion of CRE in the photoionization calculations; therefore, both the initial and final states correspond to configurations represented with orthogonal orbitals. Thus, the wave functions for the target states are those produced with approximation AS1.

HULLAC is a multiconfiguration, relativistic computing package that is based on the relativistic version of the parametric potential method by Klapisch et al. (1977), and employs a factorization-interpolation method within the framework of the distorted wave approximation (Bar-Shalom et al., 1988). It includes the Breit interaction

for relativistic configuration averages and can take into account part of the correlation effects by allowing different potentials for each group of configurations. Its newest version (Klapisch & Busquet, 2009), which is used here, incorporates a number of improvements such as important corrections to the photoionization subroutines. For the present work we calculated only transition energies and direct photoionization cross sections, but HULLAC can also efficiently compute photo-autoionization resonances by means of the isolated resonance approximation (Oreg et al., 1991), which are subsequently superimposed on the continuum photoionization cross section. Moreover, attempts have been made to adapt HULLAC to calculate the quantum interference of resonances with the continuum that leads to Fano-type asymmetric profiles (Behar et al., 2000, 2004). However, these calculations with HULLAC are beyond the scope of the present paper.

5.3 Results

5.3.1 Energy levels

Energies have been computed for both valence and K-vacancy levels in the five approximations delineated in Section 5.2 and with HULLAC. A comparison of approximations AS1 with AS2 provides an estimate of CRE while those of AS1 with AS3 and HF1 with HF2 give measures of out-of-complex CI. Also, level energy accuracy can be bound with a comparison of AS2 and HF1, that is, from two physically comparable approximations but calculated with two independent numerical codes.

In Figure 5.1, average energy differences for AS1 vs. AS2 and AS1 vs. AS3 are plotted for each ionic species, $3 \leq N \leq 7$. It may be seen that while core relaxation effects lowers the valence-level energies by around 0.5–0.8 eV, it raises by a similar amount those for the K-vacancy levels in species with electron number $3 \leq N \leq 5$; as a consequence, transition wavelengths for these ions are expected to be shorter due to this effect. Although $n = 3$ CI also causes a lowering (less than 0.7 eV) of the valence level energies (see Figure 5.1), the impact on the K-vacancy level energies is

more pronounced (as large as 1.5 eV): it mainly lowers levels for species with $N < 5$ and raises those for $N > 5$. The latter result is mostly due to K-vacancy levels from the $n = 2$ and $n = 3$ complexes intermixing in the lowly ionized members.

Figure 5.2 shows the corresponding quantities for HF1 and HF2. As shown in Figure 5.2, the effect of CI on the energies computed with HFR is somewhat different as they are decreased (less than 0.5 eV) for both valence and K-vacancy levels, the minimum occurring in ions with $N = 5$ and $N = 6$. Level energy differences between the AS2 and HF1 data sets are within 0.5 eV which is a reliable accuracy ranking of the present level energies.

Computed level energies are compared with the few spectroscopic measurements available ($2 \leq N \leq 3$) in Table 5.1. It may be seen that CRE in AUTOSTRUCTURE (approximation AS2) in general reduce differences with experiment. Furthermore, HFR and HULLAC seem to provide better energies than AUTOSTRUCTURE; differences of HFR (HULLAC) with experiment not being larger than 1.53 eV (1.19 eV). In the He-like system, HULLAC is particularly accurate for triplet states and less so for singlet states. The accurate approximation of HF2 is compared with previously computed term energies in Table 5.2. Although we would not quote present term energies with the same number of significant figures as previous results, HF2 values are consistently lower.

Fine-structure level splittings in HF2 can be problematic as shown in Table 5.3. It may be seen that HF2 gives a value in good accord (1%) with beam-foil measurements for the $\Delta E(^5\mathrm{P}_2, ^5\mathrm{P}_1)$ splitting of the $1s2s2p^2\ ^5\mathrm{P}$ K-vacancy term of N IV but an intolerably discrepant one (factor of 2) for $\Delta E(^5\mathrm{P}_3, ^5\mathrm{P}_2)$. On the other hand, both AS2 splittings are in reasonable agreement (10%) with experiment and with results obtained with the relativistic Raleigh–Ritz variational method (Yang & Chung, 1995; Wang & Gou, 2006) and MCDF (Hata & Grant, 1983; Hardis et al., 1984). This problem has been shown by Hata & Grant (1983) to be due to the neglect of the Breit interaction which is the case in HF2.

The most stringent accuracy requirements for the energies come from the capabilities of the astronomical instruments which can observe these transitions. Current

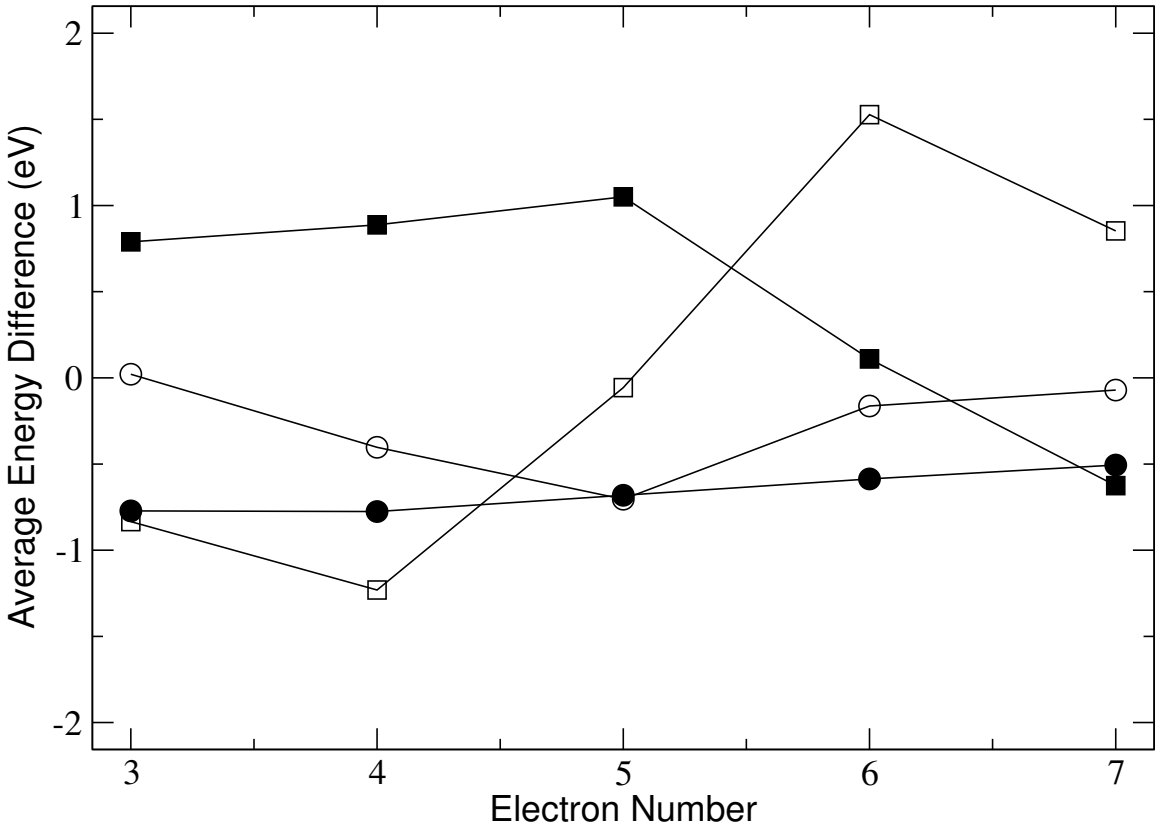

Figure 5.1 Average level energy differences with respect to approximation AS1 for ions of the nitrogen isonuclear sequence with electron number $3 \leq N \leq 7$. Filled circles: valence level energies computed with AS2. Open circles: valence level energies computed with AS3. Filled squares: K-vacancy level energies computed with AS2. Open squares: K-vacancy level energies computed with AS3.

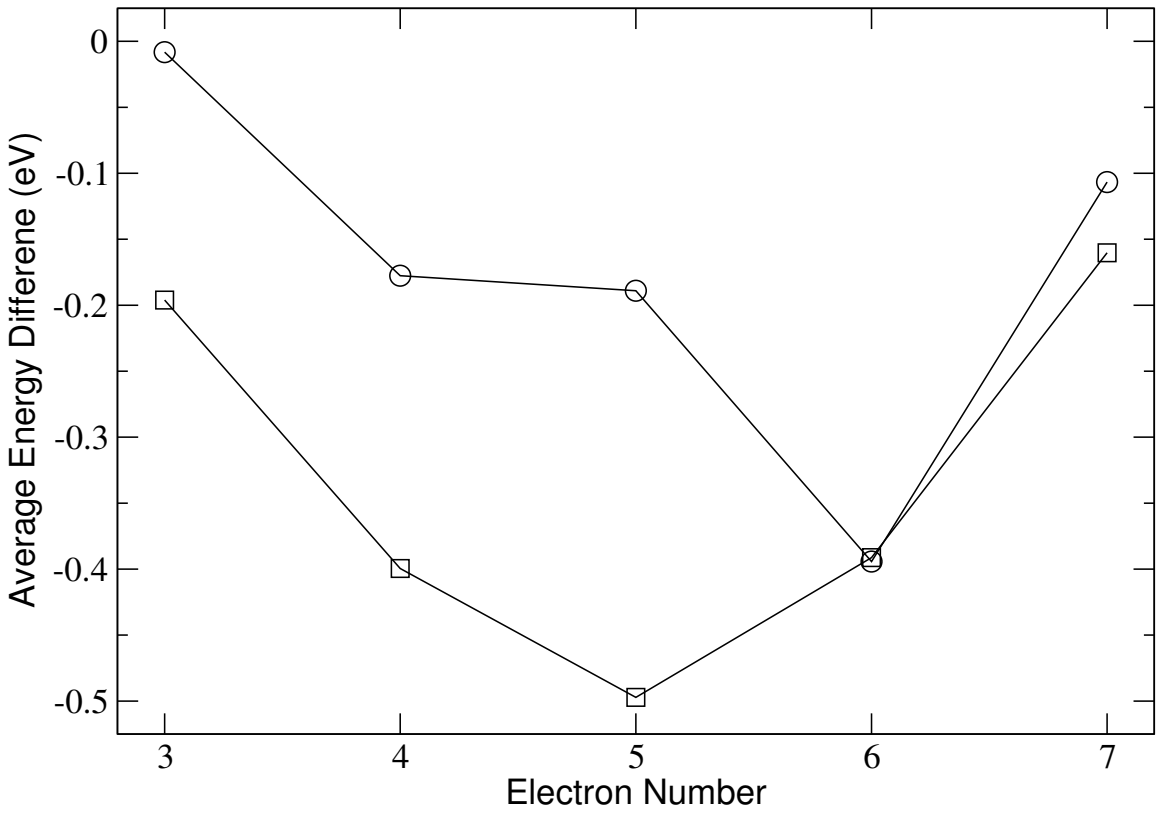

Figure 5.2 Average level energy differences with respect to approximation HF1 for ions of the nitrogen isonuclear sequence with electron number $3 \leq N \leq 7$. Open circles: valence level energies computed with HF2. Open squares: K-vacancy level energies computed with HF2.

Table 5.1. Measured and computed K-vacancy level energies (eV)

N	Level	E	E(Th) − E(Expt)					
		Expt	AS1	AS2	AS3	HF1	HF2	HULLAC
2	1s2s ^{3}S$_1$	419.80	−1.76	−1.34	−2.35	−0.59		0.01
2	1s2p ^{3}P$^o_0$	426.30	−1.85	−0.93	−2.36	−0.56		0.09
2	1s2p ^{3}P$^o_1$	426.30	−1.85	−0.93	−2.36	−0.54		0.11
2	1s2p ^{3}P$^o_2$	426.33	−1.86	−0.94	−2.37	−0.53		0.13
2	1s2s ^{1}S$_0$	426.42	−1.61	−0.21	−2.15	0.03		0.69
2	1s2p ^{1}P$^o_1$	430.70	−1.64	−0.85	−2.24	−0.24		0.67
3	1s(^{2}S)2s2p(^{3}P^o) ^{4}P$^o_{5/2}$	414.61	−2.49	−1.97	−3.64	−1.48	−1.53	0.42
3	1s(^{2}S)2s2p(^{3}P^o) ^{2}P$^o_{3/2}$	421.52[a]	−1.72	−0.80	−2.18	−0.51	−0.62	0.83
3	1s(^{2}S)2p^2(^{3}P) ^{4}P$_{5/2}$	425.70	−2.54	−1.64	−3.37	−1.31	−1.33	1.19

Note. — Experimental level energies (relative to the ion ground state) from the NIST database (Ralchenko et al., 2008).

[a]Derived from the wavelength measurement of Beiersdorfer et al. (1999).

Table 5.2. Computed total energies (au) for K-vacancy terms

N	Term	HF2	Other theory
3	$1s2s2p\ ^4P^o$	−33.240	−33.192008[a], −33.192204[b]
3	$1s(^2S)2s2p(^3P^o)\ ^2P^o$	−32.952	−32.919222[a]
3	$1s(^2S)2s2p(^1P^o)\ ^2P^o$	−32.777	−32.768550[a]
4	$1s2s^22p\ ^3P^o$	−36.219	−36.171232[c], −36.173064[d]
4	$1s2s2p^2\ ^3S$	−35.646	−35.615357[d]
4	$1s2s2p^2\ ^3P$	−35.842	−35.788866[d]
4	$1s2s2p^2\ ^3P$	−35.542	−35.536868[d]
4	$1s2s2p^2\ ^3D$	−35.815	−35.785042[d]
4	$1s2s^22p\ ^1P^o$	−36.081	−36.036967[e]
4	$1s2p^3\ ^1P^o$	−35.086	−35.082958[e]
4	$1s2s2p^2\ ^1D$	−35.594	−35.583448[f]
4	$1s2s2p^2\ ^1P$	−35.445	−35.435017[f]
4	$1s2s2p^2\ ^1S$	−35.425	−35.415017[f]
4	$1s2s2p^2\ ^5P$	−36.160	−36.0934586[g], −36.0934407[h]
4	$1s2p^3\ ^5S^o$	−35.596	−35.5414665[g], −35.5413248[h]
4	$1s2p^3\ ^3P^o$	−35.214	−35.204065[i]
4	$1s2p^3\ ^3D^o$	−35.387	−35.366601[i]

[a]Breit–Pauli saddle-point complex-rotation method (Davis & Chung, 1989)

[b]Relativistic Raleigh–Ritz variational method (Hsu et al., 1991)

[c]Breit–Pauli saddle-point complex-rotation method (Chung, 1990)

[d]Breit–Pauli saddle-point complex-rotation method (Lin et al., 2001)

[e]Breit–Pauli saddle-point complex-rotation method (Lin et al., 2002)

[f]Breit–Pauli saddle-point complex-rotation method (Shiu et al., 2001)

[g]Relativistic Raleigh–Ritz variational method (Wang & Gou, 2006)

[h]Relativistic Raleigh–Ritz variational method (Yang & Chung, 1995)

[i]Breit–Pauli saddle-point complex-rotation method (Zhang et al., 2005)

Table 5.3. Level splittings (cm^{-1}) for the $1s2s2p^2\ ^5P$ K-vacancy term of N IV

Level splitting	Expt[a]	HF2	AS2	Other theory
$\Delta E(^5P_2,^5P_1)$	127± 1	126	119	127.07[b]; 126.9[c]; 129.19[d]; 128.94[e]
$\Delta E(^5P_3,^5P_2)$	79.5± 0.8	188	70	78.49[b]; 78.45[c]; 86.72[d]; 86.58[e]

[a]Beam-foil measurements by Berry et al. (1982)

[b]Relativistic Raleigh–Ritz variational method (Wang & Gou, 2006)

[c]Relativistic Raleigh–Ritz variational method (Yang & Chung, 1995)

[d]MCDF-EAL calculation of Hata & Grant (1983)

[e]MCDF calculation of Hardis et al. (1984)

instruments, the *Chandra* and *XMM-Newton* gratings, have a resolving power which is nominally $\varepsilon/\Delta\varepsilon \leq 1000$, which imposes a resolution of $0.4 - 0.5$ eV in the energy region of the nitrogen K lines ($400 - 500$ eV), essentially the same accuracy we have achieved in the present calculations. However, in spectra with good statistical signal-to-noise it is possible to determine line centroids to a factor $\sim$3 more accurately than this. Future instruments, principally the grating instruments considered for the International X-ray Observatory (IXO), may also have resolving power as high as 3000. Knowledge of transition wavelengths and energy levels with this precision is needed for truly unambiguous identification of observed features and comparison with models. Clearly, precise laboratory measurements are irreplaceable requisites in the theoretical fine-tuning of these calculations in order to reduce the current uncertainties.

5.3.2 Wavelengths

The accuracy of computed wavelengths must be determined without a comparison with measurements due to the scarcity of the latter. CRE and $n = 3$ CI in AUTOSTRUCTURE impact wavelengths in an opposite manner to that displayed for the K-vacancy levels in Figure 5.1. Specifically, core relaxation on average shortens wavelengths by as much as 150 mÅ in ions with $2 \leq N \leq 5$ while the effect is less pronounced on the higher members. CI increases wavelengths by $\sim$50 mÅ for $N \leq 4$ and decreases them by as much as 150 mÅ for $N \geq 5$. CI in HFR in general increases wavelengths with a maximum of 25 mÅ at $N = 5$.

Wavelengths computed with AS2 are on average 7 ± 21 mÅ greater than HF1. This finding can be further appreciated in a comparison with the few available measured wavelengths (see Table 5.4) where computed values are always greater. HF1 differences with experiment are the smallest (less than 37 mÅ) while CRE in AUTOSTRUCTURE (AS2) also reduces discrepancies.

Wavelengths for K transitions in nitrogen ions have been previously computed with the MCDF method by Chen (1986); Chen & Crasemann (1987, 1988); Chen

Table 5.4. Experimental and theoretical wavelengths (Å) for nitrogen ions

N	Lower level	Upper level	λ(Expt)[a]	λ(Th) − λ(Expt)				
				HF1	AS1	AS2	AS3	HULLAC
2	$1s^2\ ^1S_0$	$1s2s\ ^3S_1$	29.5321(26)		0.1266	0.0971	0.1683	0.0012
2	$1s^2\ ^1S_0$	$1s2p\ ^3P^o_1$	29.0835(26)	0.0374	0.1274	0.0642	0.1627	–0.0074
2	$1s^2\ ^1S_0$	$1s2p\ ^1P^o_1$	28.7861(22)	0.0167	0.1108	0.0576	0.1515	–0.0444
3	$1s^22s\ ^2S_{1/2}$	$1s2s2p\ ^2P^o_{3/2}$	29.4135(37)	0.0353	0.1208	0.0560	0.1550	–0.0573

[a]Wavelength measurements by Beiersdorfer et al. (1999)

et al. (1997). While reasonable agreement is found with HF2 for species with $N = 3$ (average difference of 13 ± 25 mÅ) and $N = 5$ (average difference of -4 ± 33 mÅ), puzzling discrepancies are found for those with $N = 4$ and $N = 6$. As shown in Figure 5.3, the MCDF wavelengths of Chen & Crasemann (1987) show the large average difference with respect to HF2 of 155 ± 45 mÅ; i.e., on average, they are significantly longer. The situation in the C-like ion is somewhat different (see Figure 5.4) where the average difference with HF2 is now -45 ± 449 mÅ showing a very wide and clustered scatter with questionable deviations as large as 800 mÅ. These comparisons lead us to conclude that the wavelengths computed with HF2, our best approximation, are accurate to better than 100 mÅ.

5.3.3 *A*-coefficients

By comparing A-coefficients computed with approximations AS1 and AS2, CRE on the K radiative decay process may be estimated. Discarding transitions subject to cancellation which always display large differences, it is found that, for $\log A \geq 10$, CRE generally causes differences not greater than 20%. However, larger discrepancies (54%) are found for transitions undergoing multiple electron jumps such as those tabulated in Table 5.5. A-coefficients for these peculiar transitions computed with HF1, which should be comparable to AS2, are also included in Table 5.5 finding good

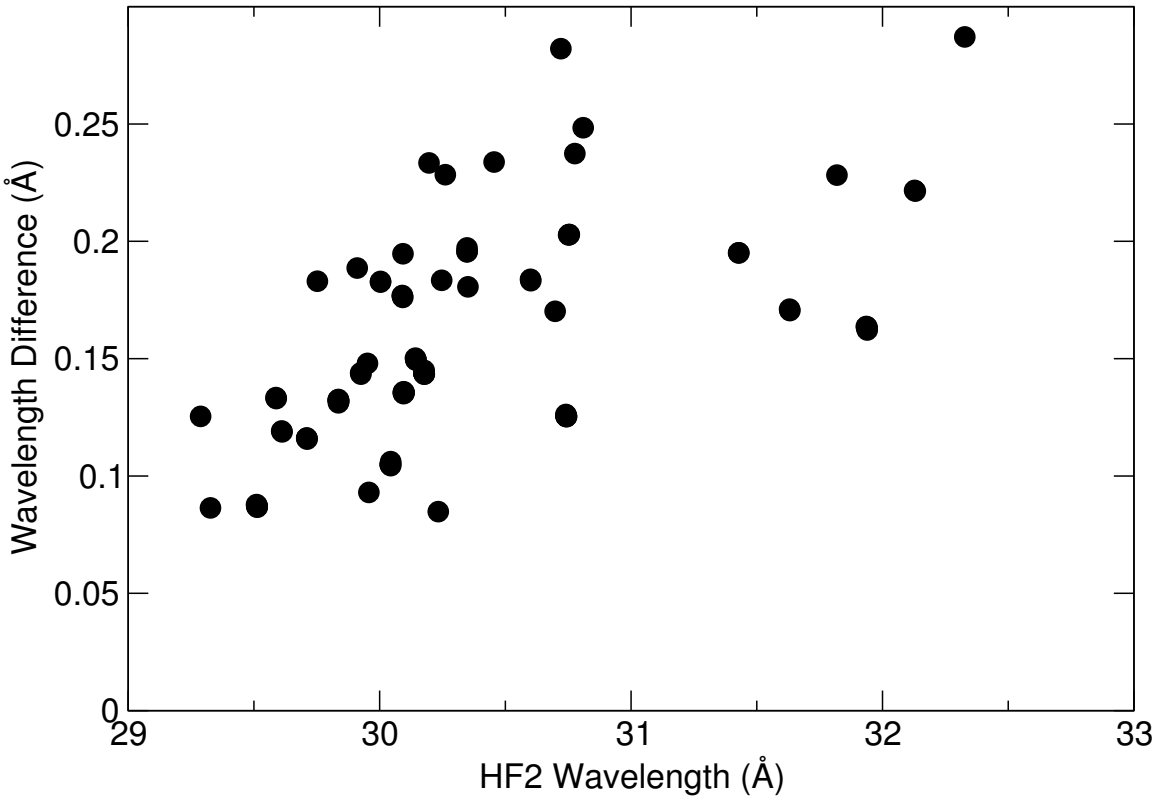

Figure 5.3 Wavelength differences between MCDF (Chen & Crasemann, 1987) and HF2 for N IV. An average difference of 155 ± 45 mÅ is observed.

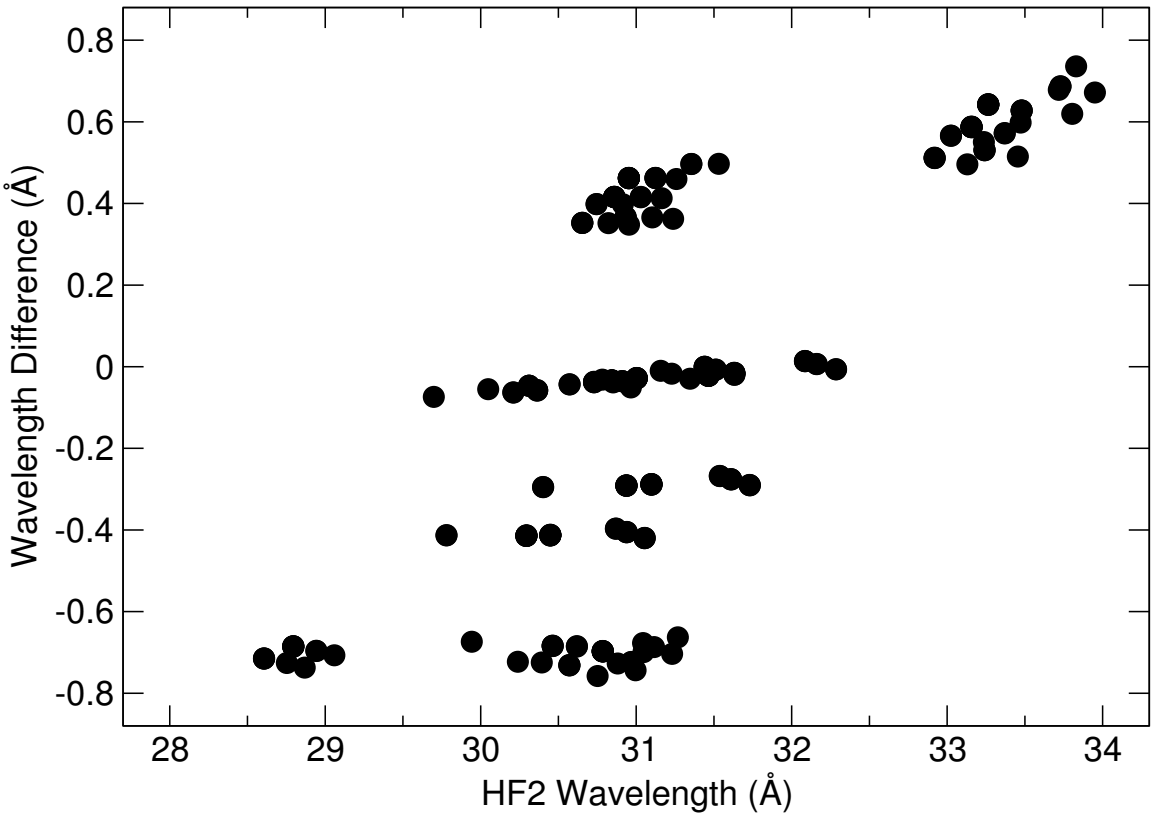

Figure 5.4 Wavelength differences between MCDF (Chen et al., 1997) and HF2 for N II. Differences as large as 800 mÅ are observed.

Table 5.5. Core relaxation effects on K radiative decay

N	j	i	A_{ji} (s^{-1})		
			AS1	AS2	HF1
3	$1s2s^2\ ^2S_{1/2}$	$1s^22p\ ^2P^o_{1/2}$	3.85E+10	5.36E+10	4.63E+10
3	$1s2s^2\ ^2S_{1/2}$	$1s^22p\ ^2P^o_{3/2}$	7.62E+10	1.06E+11	9.18E+10
4	$1s2s^22p\ ^1P^o_1$	$1s^22p^2\ ^1D_2$	9.72E+10	1.36E+11	1.24E+11
5	$1s2s^22p^2\ ^2P_{1/2}$	$1s^22p^3\ ^2P^o_{1/2}$	1.17E+10	1.80E+10	1.78E+10
5	$1s2s^22p^2\ ^2P_{3/2}$	$1s^22p^3\ ^2P^o_{3/2}$	1.54E+10	2.36E+10	2.32E+10

agreement (within 15%); in fact, differences between A-coefficients computed with approximations AS2 and HF1 are in general within 22%. Furthermore, CI from the $n = 3$ complex tends to decrease A-coefficients with $\log A \geq 10$, AS3 being on average 16% lower than AS1 and HF2 6% lower than HF1.

MCDF A-coefficients by Chen (1986); Chen & Crasemann (1987, 1988); Chen et al. (1997) agree with HF2 to around 25% except for $N = 6$ where they are found to be, on average, higher by a factor of 4 (see Figure 5.5). This outcome certainly questions the accuracy of the MCDF A-coefficients by Chen et al. (1997) for C-like nitrogen. We find that for $\log A \geq 10$ present A-coefficients are accurate to within 20% for transitions not affected by cancellation.

5.3.4 Radiative widths

A comparison of AS1 and AS2 radiative widths for the K-vacancy levels indicates that CRE are mainly noticeable in the highly ionized species, namely those with $N \leq 4$, where on average the radiative widths are increased by around 10%. On the other hand, the inclusion of levels from the $n = 3$ complex in the CI expansion (AS3) leads

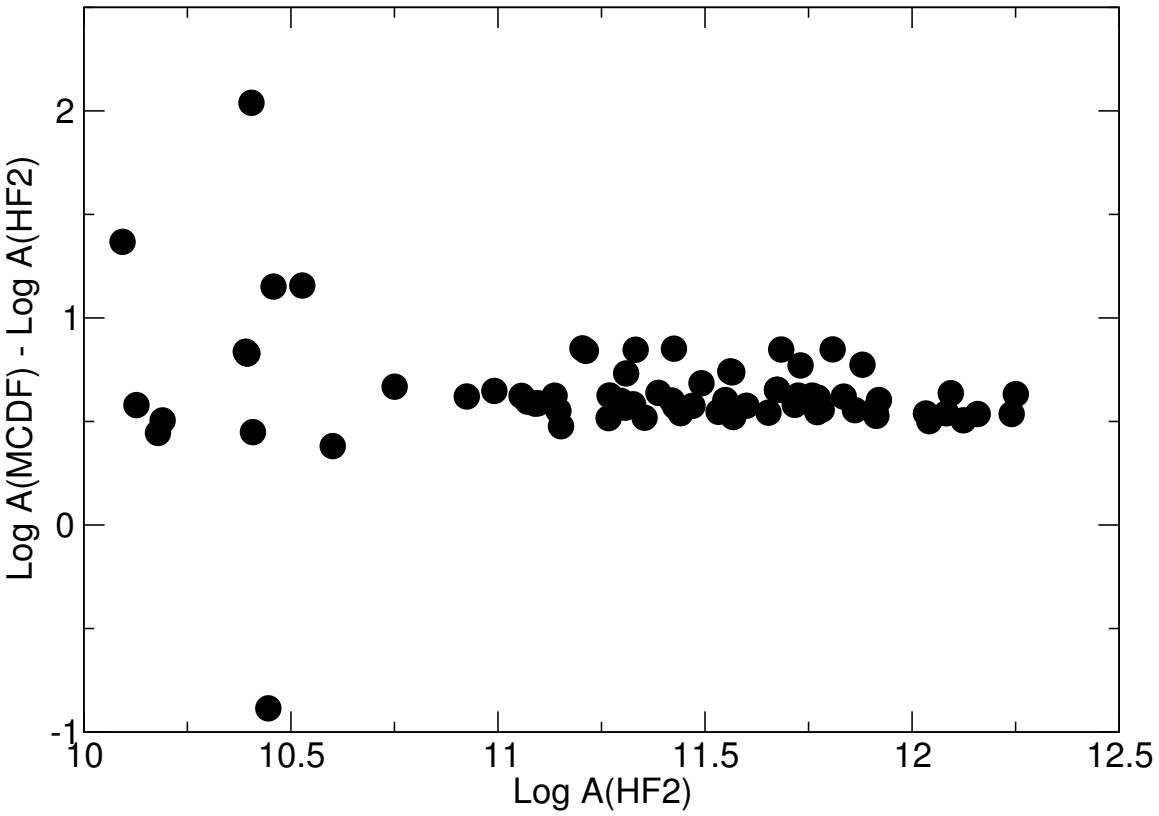

Figure 5.5 A-coefficient differences (s^{-1}) between MCDF (Chen et al., 1997) and HF2 for N II. It is found that MCDF is on average higher by a factor of 4.

to slightly reduced radiative widths (less than 7%) with respect to AS1 for the lowly ionized members ($N \geq 5$). Larger reductions ($\sim$20%) are also observed for the lowly ionized species between HF2 (which contains CI from the $n = 3$ complex) and HF1 (which contains CI only from the $n = 2$ complex).

A remarkable exception is the radiative width of the $1s2s^22p^3\ ^5S^o_2$ level in the C-like ion. For this level, AS2 gives $A_j = \sum_i A_{ji} = 7.09 \times 10^6$ s^{-1} in good agreement with HF1 (7.65×10^6 s^{-1}); however, the AS3 and HF2 radiative widths are respectively $A_j = 5.31 \times 10^8$ s^{-1} and $A_j = 3.77 \times 10^9$ s^{-1}, i.e. around two orders of magnitude larger. The reason for this huge increase when levels from $n = 3$ complex are included in the CI expansion may be appreciated in Table 5.6. Within the $n = 2$ complex, the $1s2s^22p^3\ ^5S^o_2$ decays radiatively to the $1s^22s^22p^2\ ^3P_j$ ground levels via two spin-forbidden Kα transitions which have small A-coefficients ($\lesssim 10^7$ s^{-1}). When the $n = 3$ complex is taken into account, $3 \rightarrow 2$ spin-allowed channels appear which exhibit considerably larger A-coefficients that add up to the quoted enhancement. The observed discrepancy between AS3 and HF2 (a factor of 7) are due to severe cancellation in the $\Delta n \neq 0$ transitions.

Radiative widths computed for ions with electron number $3 \leq N \leq 6$ with the MCDF method (Chen, 1986; Chen & Crasemann, 1987, 1988; Chen et al., 1997) agree with HF2 to around 20% except for the C-like species where MCDF is a factor of 4.6 higher.

5.3.5 Auger widths

Auger widths computed with AS2 and HF1 agree to within 20% but are sensitive to both CRE and CI as depicted in Figures 5.6–5.7. A comparison of AS1 and AS2 shows that, on average, CRE effects increase Auger widths with $\log A_a \geq 12$ linearly as a function of the ion electron number N. In AUTOSTRUCTURE CI also increases Auger widths, particularly for highly ionized species (around 28% for ions with $3 \leq N \leq 4$) while in HFR Auger widths are decreased (up to 15% for the lowly ionized members). We believe these contrasting outcomes are due to the way orbitals

Table 5.6. Radiative decay routes of $1s2s^22p^3\ {}^5S^o_2$ in N II

j	i	A_{ji} (s^{-1})	
		AS3	HF2
$1s2s^22p^3\ {}^5S^o_2$	$1s^22s^22p^2\ {}^3P_1$	2.04E+6	8.57E+6
	$1s^22s^22p^2\ {}^3P_2$	2.97E+6	2.53E+7
	$1s^22s2p^23d\ {}^5P_1$	5.07E+7	3.43E+8
	$1s^22s2p^23d\ {}^5P_2$	8.36E+7	5.70E+8
	$1s^22s2p^23d\ {}^5P_3$	1.17E+8	7.97E+8
	$1s^22p^33p\ {}^5P_1$	7.85E+7	6.99E+8
	$1s^22p^33p\ {}^5P_2$	1.31E+7	1.16E+9
	$1s^22p^33p\ {}^5P_3$	1.83E+8	1.63E+8
$\sum_i A_{ji}$		5.31E+8	3.77E+9

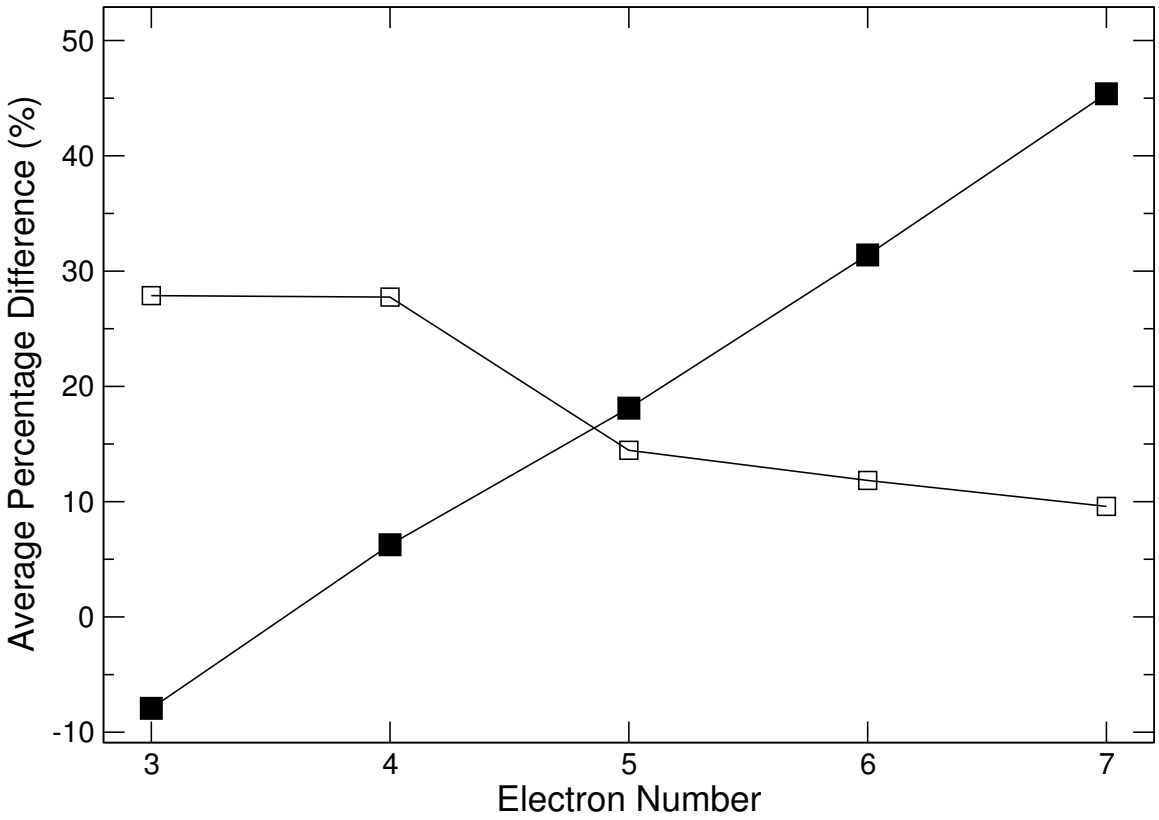

Figure 5.6 Average percentage difference between Auger widths ($\log A_{\rm a} \geq 12$) computed with the AS2 and AS1 approximations (filled squares) and with AS3 and AS1 (open squares).

have been optimized in AUTOSTRUCTURE.

Excluding the C-like ion, MCDF Auger widths by Chen (1986); Chen & Crasemann (1987, 1988); Chen et al. (1997) with $\log A_{\rm a} \geq 12$ in general agree with HF2 to around 20%. Larger discrepancies are encountered for a handful of K-vacancy levels listed in Table 5.7 which are mainly caused by level admixture. It may be seen therein that Auger widths computed with our different approximations also display a wide scatter thus supporting this diagnostic. For the C-like ion, the MCDF Auger widths are, on average, a factor of 3 higher than HF2 and thus believed to be of poor quality.

In Table 5.8, Auger widths for the 1s2s2p levels of N V computed with the Breit–

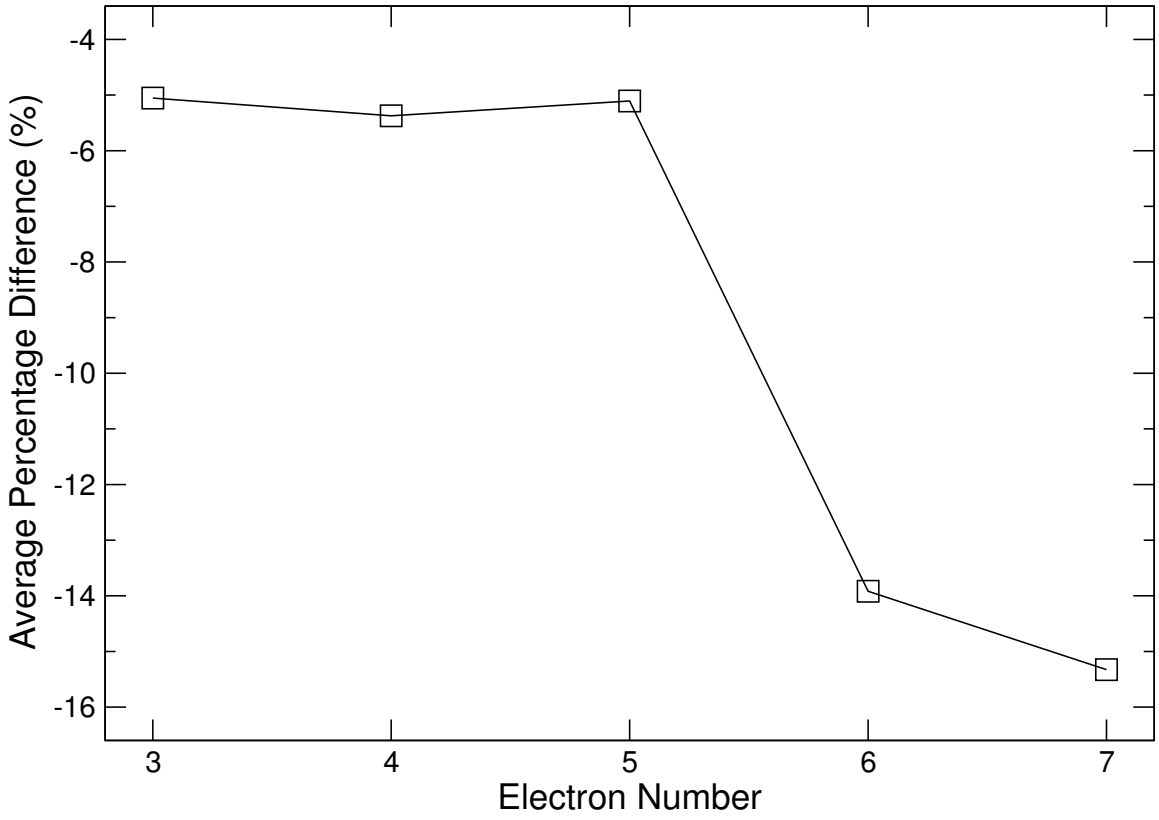

Figure 5.7 Average percentage difference between Auger widths ($\log A_{\rm a} \geq 12$) computed with the HF2 and HF1.

Table 5.7. Discrepant Auger rates (s^{-1})

N	Level	AS1	AS2	AS3	HF1	HF2	MCDF[a]
3	$1s(^2S)2s2p(^3P^o)\ ^2P^o_{1/2}$	1.51E+13	5.81E+12	2.15E+13	8.61E+12	7.63E+12	1.41E+13
3	$1s(^2S)2s2p(^3P^o)\ ^2P^o_{3/2}$	1.43E+13	5.27E+12	2.02E+13	8.29E+12	7.30E+12	1.35E+13
4	$1s(^2S)2s2p^2(^4P)\ ^3P_0$	3.09E+13	1.99E+13	4.41E+13	1.86E+13	1.77E+13	3.73E+13
4	$1s(^2S)2s2p^2(^4P)\ ^3P_1$	3.08E+13	1.98E+13	4.40E+13	1.86E+13	1.76E+13	3.68E+13
4	$1s(^2S)2s2p^2(^4P)\ ^3P_2$	3.04E+13	1.95E+13	4.36E+13	1.85E+13	1.75E+13	3.55E+13
4	$1s(^2S)2s2p^2(^2P)\ ^1P_1$	2.26E+13	2.88E+13	2.62E+13	2.46E+13	2.34E+13	1.43E+14
4	$1s(^2S)2s2p^2(^2S)\ ^1S_0$	1.34E+14	1.33E+14	1.77E+14	1.28E+14	1.19E+14	1.77E+13
5	$1s(^2S)2s2p^3(^5S^o)\ ^4S^o_{3/2}$	3.90E+13	2.98E+13	4.10E+13	2.54E+13	2.48E+13	3.89E+13
5	$1s(^2S)2s2p^3(^3S^o)\ ^2S^o_{1/2}$	2.34E+13	3.09E+13	2.88E+13	5.30E+13	1.31E+14	3.49E+13
5	$1s(^2S)2s2p^3(^1P^o)\ ^2P^o_{1/2}$	1.37E+14	1.67E+14	1.56E+14	1.27E+14	3.48E+13	1.52E+14

[a]MCDF computations by Chen (1986); Chen & Crasemann (1987, 1988)

Pauli saddle-point complex-rotation method (Davis & Chung, 1989) are compared with AS2, HF2, and the MCDF values of Chen (1986). The agreement with AS2 is within 15% while very large differences are found for the HF2 $^4P^o_j$ levels which are most surely due to the neglect of the two-body Breit interaction in HFR. The accord with MCDF is around 25% except for the 1s2s2p $^2P^o$ term where a discrepancy of a factor of 2 is encountered. The latter is difficult to explain.

Auger widths for K-vacancy terms in N IV computed with the Breit–Pauli saddle-point complex-rotation method (Lin et al., 2001, 2002; Zhang et al., 2005) are compared with AS2, HF2, and MCDF (Chen & Crasemann, 1987) in Table 5.9. The level of agreement with AS2 and HF2 is around 20% except for the values quoted by Zhang et al. (2005) for the $1s2p^3\ ^3P^o$ and $^3D^o$ terms which are discrepant by about 50%, in contrast with the MCDF Auger widths for these two terms which agree with AS2 and HF2 to within 10%. The rest of the MCDF Auger widths are in good agreement except for the $1s2s2p^2\ ^3P$ term which has already been singled out in Table 5.7 as being sensitive to level mixing.

Table 5.8. Auger energy widths (au) for 1s2s2p levels in N V

Level	AS2	HF2	Other theory
$1s(^2S)2s2p(^3P^o)\ ^4P^o_{1/2}$	1.46E−08	3.48E−10	1.50E−08[a], 1.532E−08[b]
$1s(^2S)2s2p(^3P^o)\ ^4P^o_{3/2}$	4.53E−09	8.83E−10	4.98E−09[a], 3.952E−09[b]
$1s(^2S)2s2p(^3P^o)\ ^4P^o_{5/2}$	4.26E−10		4.587E−10[b]
$1s(^2S)2s2p(^3P^o)\ ^2P^o$	1.32E−04	1.79E−04	3.31E−04[a], 1.54E−04[b]
$1s(^2S)2s2p(^1P^o)\ ^2P^o$	1.68E−03	1.47E−03	1.14E−03[a], 1.53E−03[b]

[a]MCDF calculations by (Chen, 1986)

[b]Breit–Pauli saddle-point complex-rotation method (Davis & Chung, 1989)

5.3.6 Photoabsorption cross sections

In Figure 5.8, we show the high-energy photoabsorption cross sections of N I – N V computed with the BPRM package. Intermediate coupling has been used by implementing the AS1 approximation to describe the target wave functions. In order to resolve accurately the K-threshold region, radiative and Auger damping are taken into account as described by Gorczyca & McLaughlin (2000) using the Auger widths calculated with the HF2 approximation. For comparison, we have included the photoionization cross sections obtained with the HULLAC code and those by Reilman & Manson (1979), the latter calculated in a central-field potential. This comparison shows that the K-threshold energies of BPRM and HULLAC are in very good accord (within 1 eV) and the background cross sections to within $\sim 10\%$. Note that for the sake of comparison, we have used HULLAC only to compute the direct bound-free photoionization cross section and not the resonances.

Background cross sections by Reilman & Manson (1979) are in excellent agreement with BPRM for all ions, but K-edge positions and structures are clearly discrepant. The present BPRM calculations result in smeared K edges due to the dominance of the Auger spectator (KLL) channels over the participator (KLn) channels. This overall

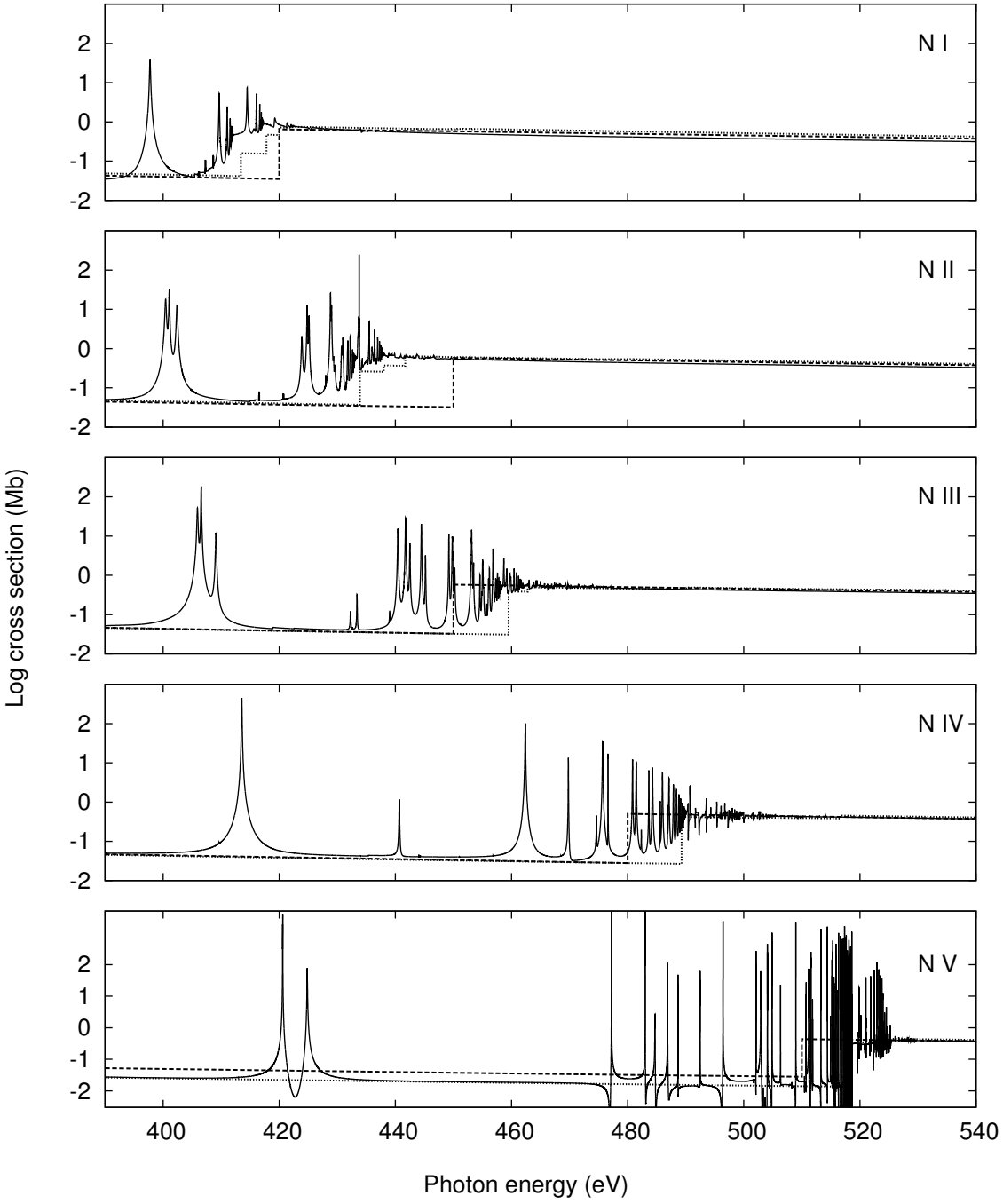

Figure 5.8 High-energy photoabsorption cross sections for nitrogen ions in the K-edge region. Solid curve: BPRM. Dotted curve: HULLAC. Dashed curve: Reilman & Manson (1979).

behavior is similar to that reported in previous calculations (Kallman et al., 2004; Witthoeft et al., 2009), and in particular to that displayed by the corresponding oxygen ions (see Figure 5 in García et al., 2005).

5.3.7 Additional Tables

We include two long tables in the Appendix A, with all the atomic structure data. For nitrogen ions with electron occupancy $N = 1 - 7$ and for both valence and Auger levels, Table A.1 tabulates the spin multiplicity, total orbital angular momentum and total angular momentum quantum numbers, configuration assignment, energy, and radiative and Auger widths. For K transitions, Table A.2 tabulates the wavelength, A-coefficient, and gf-value.

5.4 Conclusions

Detailed calculations have been carried out on the atomic properties of K-vacancy states in ions of the nitrogen isonuclear sequence. Data sets containing energy levels, wavelengths, A-coefficients and radiative and Auger widths for K-vacancy levels have been computed with the atomic structure codes HFR and AUTOSTRUCTURE. High-energy photoionization and photoabsorption cross sections for members with electron occupancies $N \geq 3$ have been calculated with the BPRM and HULLAC codes.

Our best approximation (HF2) takes into account both core-relaxation effects and configuration interaction from the $n = 3$ complex. By comparing results from different approximations with previous theoretical work and the few spectroscopic measurements available, we conclude that level energies and wavelengths for all the nitrogen ions considered in the present calculations can be quoted to be accurate to within 0.5 eV and 100 mÅ, respectively. The accuracy of A-coefficients and radiative and Auger widths is estimated at approximately 20% for transitions neither affected by cancelation nor strong level admixture. Outstanding discrepancies are found with some MCDF data, in particular wavelengths and A-coefficients for the C-like ion

which are believed to be due to numerical error by Chen et al. (1997).

We have also presented detailed photoabsorption cross sections of nitrogen ions in the near K-threshold region. Due to the lack of previous experimental and theoretical results, we have also performed simpler calculations using the HULLAC code in order to check for consistency and to estimate accuracy. Comparison of BPRM and HULLAC indicates that present K-threshold energies are accurate to within 1 eV. However, background cross sections are in better agreement with those computed by Reilman & Manson (1979) in a central-field potential for all ions except the Li-like system. These photoabsorption cross sections and their structures are similar to those displayed by ions in the same isoelectronic sequence (Witthoeft et al., 2009), especially to the corresponding oxygen ions (García et al., 2005). The present atomic data sets are available to the public and have being incorporated in the XSTAR modeling code in order to generate improved opacities in the nitrogen K-edge region, which will lead to useful astrophysical diagnostics such as those mentioned in Section 5.1.

Table 5.9. Auger widths (meV) for K-vacancy terms in N IV

Term	AS2	HF2	Other theory
$1s2s^22p\ ^3P^o$	84.1	71.8	77.4[a]; 79.0[b]
$1s(^2S)2s2p^2(^4P)\ ^3P$	12.9	11.6	23.8[a]; 10.8[b]
$1s(^2S)2s2p^2(^2D)\ ^3D$	66.9	62.6	53.4[a]; 57.7[b]
$1s(^2S)2s2p^2(^2S)\ ^3S$	31.2	29.7	26.7[a]; 28.6[b]
$1s(^2S)2s2p^2(^2P)\ ^3P$	66.4	55.5	58.5[a]; 55.0[b]
$1s2s^22p\ ^1P^o$	55.2	48.3	53.8[a]; 58[c]
$1s2p^3\ ^1P^o$	44.9	47.0	43.8[a]; 43[c]
$1s2p^3\ ^3D^o$	80.7	80.3	75.0[a]; 53.87[d]
$1s2p^3\ ^3P^o$	47.4	47.5	45.5[a]; 34.16[d]

[a]MCDF method (Chen & Crasemann, 1987)

[b]Breit–Pauli saddle-point complex-rotation method (Lin et al., 2001)

[c]Breit–Pauli saddle-point complex-rotation method (Lin et al., 2002)

[d]Breit–Pauli saddle-point complex-rotation method (Zhang et al., 2005)

6

Concluding Remarks

Answers to outstanding questions concerning accretion disks will not come alone, but with the need to reproduce and predict new observations and to identify spectral profiles at high resolution. In this dissertation we have developed new and powerful tools to analyze these observations, which yield a better understanding of the physics governing accretion onto black holes. In particular, this study constitutes the most accurate description, to date, of the physics of illuminated accretion disks and their emission spectra in the X-ray energy range.

We have presented new models for the structure of X-ray illuminated accretion disks and their reflected spectra, assuming constant density along the vertical direction. These models include the most recent and complete atomic data for the iron isonuclear sequence. The energy resolution used in the reflected spectra exceeds other models previously published as well as the resolution of the detectors on current X-ray observatories (*Chandra*, *XMM Newton, Suzaku*), and it is comparable to the expected resolving power of the forthcoming X-ray missions such as *Astro-H*.

Additionally, detailed calculations have been carried out on the atomic properties of K-vacancy states in ions of the nitrogen isonuclear sequence. Data sets containing energy levels, wavelengths, A-coefficients and radiative and Auger widths for K-vacancy levels have been computed with the atomic structure codes HFR and AUTOSTRUCTURE. High-energy photoionization and photoabsorption cross sections for

members with electron occupancies $N \geq 3$ have been calculated with the BPRM and HULLAC codes.

The calculation of the inner-shell atomic data of nitrogen ions is also relevant outside the context of accretion disk models. For instance, recent studies have pointed out significant discrepancies (up to 35%), in the abundances of C, N, O and Ne on the Sun (Asplund et al., 2005). Fluorescence N-Kα lines originated from coronal X-ray photoionization can be used as independent abundance diagnostics.

In general, our simulations show that the K-shell atomic data is crucial to properly model the structure and profile of the iron lines. These results also suggest that the line emission from Fe ions in different ionization stages and Comptonization of high energy photons by cold electrons can be responsible for significant line broadening. These processes need to be taken into account since they can be mistaken for relativistic effects, especially in cases when the gas is partially or high ionized.

Because the state of the gas in the accretion disk depends on the radiation field at each point, and the ionization balance required for a realistic definition of the source function in the radiation transfer depends on both the temperature and density of the gas, a self-consistent approach must be taken into account in order to solve the hydrostatic equilibrium equation instead of assuming constant density. This will be considered as the next step of this project. Future work will also consider the inclusion of new K-shell atomic data recently calculated for the Ne, Mg, Si, S, Ar and Ca by Palmeri et al. (2008a) and Witthoeft et al. (2009), as well as for the nickel isonuclear sequence (Palmeri et al., 2008b).

A

Tables

Table A.1: Valence and Auger levels for nitrogen ions

N	i	$2S+1$	L	$2J$	Configuration	Energy eV	Ar s^{-1}	Aa s^{-1}
1	1	2	0	1	1s 2S1/2	0.0000		
1	2	2	0	1	2s 2S1/2	500.3121		
1	3	2	1	1	2p 2Po1/2	500.3124	1.51E+12	
1	4	2	1	3	2p 2Po3/2	500.4214	1.51E+12	
2	1	1	0	0	1s2 1S0	0.0000		
2	2	3	0	2	1s2s 3S1	419.2093		
2	3	3	1	0	1s2p 3Po0	425.7365	7.01E+07	
2	4	3	1	2	1s2p 3Po1	425.7572	1.52E+08	
2	5	3	1	4	1s2p 3Po2	425.7992	7.21E+07	
2	6	1	0	0	1s2s 1S0	426.4470	9.68E+00	
2	7	1	1	2	1s2p 1Po1	430.4582	2.12E+12	
3	1	2	0	1	1s22s 2S1/2	0.0000		
3	2	2	1	1	1s22p 2Po1/2	9.9459	3.32E+08	
3	3	2	1	3	1s22p 2Po3/2	9.9774	3.35E+08	
3	4	2	0	1	1s2s2 2S1/2	410.1562	1.22E+11	9.79E+13
3	5	4	1	1	1s(2S)2s2p(3Po) 4Po1/2	413.0288	5.05E+06	1.44E+07
3	6	4	1	3	1s(2S)2s2p(3Po) 4Po3/2	413.0471	1.27E+07	3.65E+07
3	7	4	1	5	1s(2S)2s2p(3Po) 4Po5/2	413.0778	0.00E+00	1.76E+07
3	8	2	1	1	1s(2S)2s2p(3Po) 2Po1/2	420.8755	1.65E+12	7.63E+12
3	9	2	1	3	1s(2S)2s2p(3Po) 2Po3/2	420.8968	1.65E+12	7.30E+12
3	10	4	1	1	1s(2S)2p2(3P) 4P1/2	424.3267	7.99E+08	5.54E+06
3	11	4	1	3	1s(2S)2p2(3P) 4P3/2	424.3446	8.06E+08	4.65E+08
3	12	4	1	5	1s(2S)2p2(3P) 4P5/2	424.3741	8.15E+08	2.85E+09

Continued on Next Page...

Table A.1 – Continued

N	i	$2S+1$	L	$2J$	Configuration	Energy eV	Ar s^{-1}	Aa s^{-1}
3	13	2	1	1	1s(2S)2s2p(1Po) 2Po1/2	425.6391	1.63E+11	6.06E+13
3	14	2	1	3	1s(2S)2s2p(1Po) 2Po3/2	425.6545	1.55E+11	6.10E+13
3	15	2	2	3	1s(2S)2p2(1D) 2D3/2	429.2436	8.33E+11	1.07E+14
3	16	2	2	5	1s(2S)2p2(1D) 2D5/2	429.2442	8.32E+11	1.07E+14
3	17	2	1	1	1s(2S)2p2(3P) 2P1/2	430.3236	2.68E+12	1.20E+08
3	18	2	1	3	1s(2S)2p2(3P) 2P3/2	430.3597	2.68E+12	4.50E+10
3	19	2	0	1	1s(2S)2p2(1S) 2S1/2	437.1874	7.86E+11	1.60E+13
4	1	1	0	0	1s22s2 1S0	0.0000		
4	2	3	1	0	1s22s2p 3Po0	8.3920		
4	3	3	1	2	1s22s2p 3Po1	8.4008	4.70E+02	
4	4	3	1	4	1s22s2p 3Po2	8.4184		
4	5	1	1	2	1s22s2p 1Po1	17.2102	2.77E+09	
4	6	3	1	0	1s22p2 3P0	21.8846	1.85E+09	
4	7	3	1	2	1s22p2 3P1	21.8933	1.85E+09	
4	8	3	1	4	1s22p2 3P2	21.9105	1.86E+09	
4	9	1	2	4	1s22p2 1D2	24.2150	2.31E+08	
4	10	1	0	0	1s22p2 1S0	30.3419	3.36E+09	
4	11	3	1	0	1s2s22p 3Po0	410.0799	5.72E+10	1.10E+14
4	12	3	1	2	1s2s22p 3Po1	410.0948	5.73E+10	1.09E+14
4	13	3	1	4	1s2s22p 3Po2	410.1250	5.74E+10	1.09E+14
4	14	5	1	2	1s(2S)2s2p2(4P) 5P1	411.7017	5.76E+06	2.65E+08
4	15	5	1	4	1s(2S)2s2p2(4P) 5P2	411.7173	3.94E+06	1.32E+08
4	16	5	1	6	1s(2S)2s2p2(4P) 5P3	411.7406	3.76E+06	5.29E+08
4	17	1	1	2	1s2s22p 1Po1	413.8718	1.67E+12	7.34E+13
4	18	3	1	0	1s(2S)2s2p2(4P) 3P0	420.3553	2.30E+12	1.77E+13
4	19	3	1	2	1s(2S)2s2p2(4P) 3P1	420.3670	2.30E+12	1.76E+13
4	20	3	1	4	1s(2S)2s2p2(4P) 3P2	420.3907	2.30E+12	1.75E+13
4	21	3	2	2	1s(2S)2s2p2(2D) 3D1	421.0956	7.26E+11	9.51E+13
4	22	3	2	6	1s(2S)2s2p2(2D) 3D3	421.0957	7.26E+11	9.51E+13
4	23	3	2	4	1s(2S)2s2p2(2D) 3D2	421.0958	7.26E+11	9.51E+13
4	24	3	0	2	1s(2S)2s2p2(2S) 3S1	425.7094	7.88E+11	4.51E+13
4	25	5	0	4	1s2p3 5So2	427.0700	3.33E+09	4.73E+08
4	26	1	2	4	1s(2S)2s2p2(2D) 1D2	427.1172	7.44E+11	1.75E+14
4	27	3	1	0	1s(2S)2s2p2(2P) 3P0	428.5054	9.19E+10	8.43E+13
4	28	3	1	2	1s(2S)2s2p2(2P) 3P1	428.5172	9.15E+10	8.42E+13
4	29	3	1	4	1s(2S)2s2p2(2P) 3P2	428.5402	9.06E+10	8.44E+13
4	30	1	1	2	1s(2S)2s2p2(2P) 1P1	431.1610	2.35E+12	2.34E+13
4	31	1	0	0	1s(2S)2s2p2(2S) 1S0	431.7259	8.44E+11	1.19E+14
4	32	3	2	2	1s2p3 3Do1	432.7622	6.93E+11	1.22E+14
4	33	3	2	4	1s2p3 3Do2	432.7623	6.93E+11	1.22E+14

Continued on Next Page...

Table A.1 – Continued

N	i	$2S+1$	L	$2J$	Configuration	Energy eV	Ar s^{-1}	Aa s^{-1}
4	34	3	2	6	1s2p3 3Do3	432.7626	6.92E+11	1.22E+14
4	35	3	0	2	1s2p3 3So1	433.9272	3.13E+12	2.28E+09
4	36	1	2	4	1s2p3 1Do2	436.2197	2.27E+12	1.23E+14
4	37	3	1	0	1s2p3 3Po0	437.4444	6.84E+11	7.21E+13
4	38	3	1	2	1s2p3 3Po1	437.4456	6.84E+11	7.21E+13
4	39	3	1	4	1s2p3 3Po2	437.4482	6.84E+11	7.21E+13
4	40	1	1	2	1s2p3 1Po1	440.9335	2.25E+12	7.14E+13
5	1	2	1	1	1s22s22p 2Po1/2	0.0000		
5	2	2	1	3	1s22s22p 2Po3/2	0.0211		
5	3	4	1	1	1s22s2p2 4P1/2	6.5608	5.55E+02	
5	4	4	1	3	1s22s2p2 4P3/2	6.5680	6.12E+01	
5	5	4	1	5	1s22s2p2 4P5/2	6.5799	1.72E+02	
5	6	2	2	3	1s22s2p2 2D3/2	13.0818	6.64E+08	
5	7	2	2	5	1s22s2p2 2D5/2	13.0819	6.61E+08	
5	8	2	0	1	1s22s2p2 2S1/2	16.8125	3.27E+09	
5	9	2	1	1	1s22s2p2 2P1/2	19.1005	6.95E+09	
5	10	2	1	3	1s22s2p2 2P3/2	19.1147	6.96E+09	
5	11	4	0	3	1s22p3 4So3/2	22.8945	5.60E+09	
5	12	2	2	3	1s22p3 2Do3/2	26.0003	1.37E+09	
5	13	2	2	5	1s22p3 2Do5/2	26.0006	1.37E+09	
5	14	2	1	1	1s22p3 2Po1/2	29.5377	4.36E+09	
5	15	2	1	3	1s22p3 2Po3/2	29.5389	4.36E+09	
5	16	4	1	1	1s2s22p2 4P1/2	401.4482	1.93E+10	1.05E+14
5	17	4	1	3	1s2s22p2 4P3/2	401.4612	1.93E+10	1.05E+14
5	18	4	1	5	1s2s22p2 4P5/2	401.4824	1.94E+10	1.06E+14
5	19	6	0	5	1s(2S)2s2p3(5So) 6So5/2	402.1174	2.40E+06	3.30E+08
5	20	2	2	3	1s2s22p2 2D3/2	405.9641	6.64E+11	1.65E+14
5	21	2	2	5	1s2s22p2 2D5/2	405.9649	6.62E+11	1.65E+14
5	22	2	1	1	1s2s22p2 2P1/2	406.3740	2.14E+12	6.54E+13
5	23	2	1	3	1s2s22p2 2P3/2	406.4003	2.14E+12	6.56E+13
5	24	2	0	1	1s2s22p2 2S1/2	408.2965	7.94E+11	1.43E+14
5	25	4	0	3	1s(2S)2s2p3(5So) 4So3/2	411.1883	2.68E+12	2.48E+13
5	26	4	2	3	1s(2S)2s2p3(3Do) 4Do3/2	412.1210	5.89E+11	1.03E+14
5	27	4	2	1	1s(2S)2s2p3(3Do) 4Do1/2	412.1210	5.89E+11	1.03E+14
5	28	4	2	5	1s(2S)2s2p3(3Do) 4Do5/2	412.1211	5.89E+11	1.03E+14
5	29	4	2	7	1s(2S)2s2p3(3Do) 4Do7/2	412.1213	5.89E+11	1.03E+14
5	30	4	1	1	1s(2S)2s2p3(3Po) 4Po1/2	414.8402	6.18E+11	7.72E+13
5	31	4	1	3	1s(2S)2s2p3(3Po) 4Po3/2	414.8403	6.18E+11	7.72E+13
5	32	4	1	5	1s(2S)2s2p3(3Po) 4Po5/2	414.8404	6.18E+11	7.71E+13
5	33	2	2	3	1s(2S)2s2p3(3Do) 2Do3/2	418.3452	1.84E+12	1.47E+14

Continued on Next Page...

Table A.1 – Continued

N	i	$2S+1$	L	$2J$	Configuration	Energy eV	Ar s^{-1}	Aa s^{-1}
5	34	2	2	5	1s(2S)2s2p3(3Do) 2Do5/2	418.3454	1.84E+12	1.47E+14
5	35	2	1	1	1s(2S)2s2p3(3Po) 2Po1/2	421.0667	1.89E+12	1.18E+14
5	36	2	1	3	1s(2S)2s2p3(3Po) 2Po3/2	421.0667	1.89E+12	1.19E+14
5	37	4	0	3	1s(2S)2s2p3(3So) 4So3/2	422.6562	5.75E+10	9.43E+13
5	38	2	2	5	1s(2S)2s2p3(1Do) 2Do5/2	423.4389	7.17E+11	1.69E+14
5	39	2	2	3	1s(2S)2s2p3(1Do) 2Do3/2	423.4389	7.17E+11	1.69E+14
5	40	2	1	1	1s(2S)2s2p3(1Po) 2Po1/2	426.1817	9.47E+11	3.48E+13
5	41	2	1	3	1s(2S)2s2p3(1Po) 2Po3/2	426.1880	7.63E+11	1.43E+14
5	42	2	0	1	1s(2S)2s2p3(3So) 2So1/2	426.2426	2.47E+12	1.31E+14
5	43	4	1	5	1s2p4 4P5/2	428.6799	5.57E+11	9.91E+13
5	44	4	1	3	1s2p4 4P3/2	428.6989	5.57E+11	9.91E+13
5	45	4	1	1	1s2p4 4P1/2	428.7103	5.57E+11	9.92E+13
5	46	2	2	3	1s2p4 2D3/2	432.5493	1.23E+12	1.56E+14
5	47	2	2	5	1s2p4 2D5/2	432.5497	1.23E+12	1.56E+14
5	48	2	1	3	1s2p4 2P3/2	433.2427	2.72E+12	1.00E+14
5	49	2	1	1	1s2p4 2P1/2	433.2654	2.72E+12	1.00E+14
5	50	2	0	1	1s2p4 2S1/2	438.5541	1.24E+12	1.04E+14
6	1	3	1	0	1s22s22p2 3P0	0.0000		
6	2	3	1	2	1s22s22p2 3P1	0.0057		
6	3	3	1	4	1s22s22p2 3P2	0.0170		
6	4	1	2	4	1s22s22p2 1D2	2.2194		
6	5	1	0	0	1s22s22p2 1S0	3.9320		
6	6	5	0	4	1s22s2p3 5So2	4.7434	1.12E+02	
6	7	3	2	2	1s22s2p3 3Do1	11.8077	6.14E+08	
6	8	3	2	4	1s22s2p3 3Do2	11.8078	6.13E+08	
6	9	3	2	6	1s22s2p3 3Do3	11.8079	6.11E+08	
6	10	3	1	0	1s22s2p3 3Po0	13.8804	1.89E+09	
6	11	3	1	2	1s22s2p3 3Po1	13.8805	1.89E+09	
6	12	3	1	4	1s22s2p3 3Po2	13.8806	1.89E+09	
6	13	1	2	4	1s22s2p3 1Do2	19.4376	4.58E+09	
6	14	3	0	2	1s22s2p3 3So1	20.3386	1.43E+10	
6	15	1	1	2	1s22s2p3 1Po1	21.8276	7.70E+09	
6	16	3	1	4	1s22p4 3P2	27.8399	1.53E+09	
6	17	3	1	2	1s22p4 3P1	27.8483	1.53E+09	
6	18	3	1	0	1s22p4 3P0	27.8525	1.53E+09	
6	19	1	2	4	1s22p4 1D2	30.2382	1.97E+09	
6	20	1	0	0	1s22p4 1S0	34.0719	2.83E+09	
6	21	5	0	4	1s2s22p3 5So2	395.4334	6.82E+06	1.05E+14
6	22	3	2	4	1s2s22p3 3Do2	400.5709	5.29E+11	1.74E+14
6	23	3	2	2	1s2s22p3 3Do1	400.5709	5.29E+11	1.74E+14

Continued on Next Page...

Table A.1 – Continued

N	i	$2S+1$	L	$2J$	Configuration	Energy eV	Ar s^{-1}	Aa s^{-1}
6	24	3	2	6	1s2s22p3 3Do3	400.5712	5.29E+11	1.74E+14
6	25	3	0	2	1s2s22p3 3So1	400.8401	2.48E+12	6.13E+13
6	26	3	1	4	1s2s22p3 3Po2	401.7812	5.99E+11	1.64E+14
6	27	3	1	2	1s2s22p3 3Po1	401.7821	5.99E+11	1.64E+14
6	28	3	1	0	1s2s22p3 3Po0	401.7822	5.98E+11	1.64E+14
6	29	1	2	4	1s2s22p3 1Do2	403.2759	1.78E+12	1.52E+14
6	30	1	1	2	1s2s22p3 1Po1	404.4775	1.86E+12	1.42E+14
6	31	5	1	6	1s(2S)2s2p4(4P) 5P3	405.8336	4.73E+11	8.28E+13
6	32	5	1	4	1s(2S)2s2p4(4P) 5P2	405.8495	4.73E+11	8.28E+13
6	33	5	1	2	1s(2S)2s2p4(4P) 5P1	405.8601	4.73E+11	8.28E+13
6	34	3	1	4	1s(2S)2s2p4(4P) 3P2	412.5561	2.29E+12	1.24E+14
6	35	3	1	2	1s(2S)2s2p4(4P) 3P1	412.5724	2.29E+12	1.24E+14
6	36	3	1	0	1s(2S)2s2p4(4P) 3P0	412.5806	2.29E+12	1.24E+14
6	37	3	2	2	1s(2S)2s2p4(2D) 3D1	413.7875	1.01E+12	1.34E+14
6	38	3	2	4	1s(2S)2s2p4(2D) 3D2	413.7877	1.01E+12	1.34E+14
6	39	3	2	6	1s(2S)2s2p4(2D) 3D3	413.7878	1.01E+12	1.34E+14
6	40	3	0	2	1s(2S)2s2p4(2S) 3S1	417.3594	1.07E+12	1.05E+14
6	41	1	2	4	1s(2S)2s2p4(2D) 1D2	418.8142	1.04E+12	2.28E+14
6	42	3	1	4	1s(2S)2s2p4(2P) 3P2	421.0736	4.17E+11	1.24E+14
6	43	3	1	2	1s(2S)2s2p4(2P) 3P1	421.0831	4.20E+11	1.25E+14
6	44	3	1	0	1s(2S)2s2p4(2P) 3P0	421.0877	4.21E+11	1.25E+14
6	45	1	0	0	1s(2S)2s2p4(2S) 1S0	421.8244	7.65E+11	1.46E+14
6	46	1	1	2	1s(2S)2s2p4(2P) 1P1	422.2153	1.79E+12	8.98E+13
6	47	3	1	4	1s2p5 3Po2	430.5776	6.47E+11	1.28E+14
6	48	3	1	2	1s2p5 3Po1	430.5958	6.47E+11	1.28E+14
6	49	3	1	0	1s2p5 3Po0	430.6049	6.47E+11	1.28E+14
6	50	1	1	2	1s2p5 1Po1	433.4178	2.09E+12	1.41E+14
7	1	4	0	3	1s22s22p3 4So3/2	0.0000		
7	2	2	2	3	1s22s22p3 2Do3/2	2.8185		
7	3	2	2	5	1s22s22p3 2Do5/2	2.8186		
7	4	2	1	3	1s22s22p3 2Po3/2	3.7260		
7	5	2	1	1	1s22s22p3 2Po1/2	3.7263		
7	6	4	1	5	1s22s2p4 4P5/2	11.1152	7.97E+08	
7	7	4	1	3	1s22s2p4 4P3/2	11.1223	8.00E+08	
7	8	4	1	1	1s22s2p4 4P1/2	11.1266	8.02E+08	
7	9	2	2	3	1s22s2p4 2D3/2	16.7879	2.76E+09	
7	10	2	2	5	1s22s2p4 2D5/2	16.7881	2.76E+09	
7	11	2	0	1	1s22s2p4 2S1/2	19.3527	6.19E+09	
7	12	2	1	3	1s22s2p4 2P3/2	21.7170	1.32E+10	
7	13	2	1	1	1s22s2p4 2P1/2	21.7252	1.32E+10	

Continued on Next Page...

Table A.1 – Continued

N	i	$2S+1$	L	$2J$	Configuration	Energy eV	Ar s^{-1}	Aa s^{-1}
7	14	2	1	3	1s22p5 2Po3/2	33.1533	5.58E+09	
7	15	2	1	1	1s22p5 2Po1/2	33.1626	5.62E+09	
7	16	4	1	5	1s2s22p4 4P5/2	397.0912	4.65E+11	1.61E+14
7	17	4	1	3	1s2s22p4 4P3/2	397.1065	4.65E+11	1.61E+14
7	18	4	1	1	1s2s22p4 4P1/2	397.1156	4.65E+11	1.61E+14
7	19	2	2	3	1s2s22p4 2D3/2	400.4302	1.14E+12	1.44E+14
7	20	2	2	5	1s2s22p4 2D5/2	400.4352	9.68E+11	1.90E+14
7	21	2	1	3	1s2s22p4 2P3/2	400.4639	1.96E+12	1.83E+14
7	22	2	1	1	1s2s22p4 2P1/2	400.4772	2.13E+12	1.36E+14
7	23	2	0	1	1s2s22p4 2S1/2	402.0570	1.07E+12	1.80E+14
7	24	4	1	5	1s(2S)2s2p5(3Po) 4Po5/2	409.4482	8.42E+11	1.20E+14
7	25	4	1	3	1s(2S)2s2p5(3Po) 4Po3/2	409.4627	8.42E+11	1.20E+14
7	26	4	1	1	1s(2S)2s2p5(3Po) 4Po1/2	409.4715	8.42E+11	1.20E+14
7	27	2	1	3	1s(2S)2s2p5(3Po) 2Po3/2	414.7056	7.97E+11	9.20E+13
7	28	2	1	1	1s(2S)2s2p5(3Po) 2Po1/2	414.7090	8.14E+11	9.41E+13
7	29	2	1	3	1s(2S)2s2p5(1Po) 2Po3/2	419.5631	1.02E+12	1.82E+14
7	30	2	1	1	1s(2S)2s2p5(1Po) 2Po1/2	419.5711	1.02E+12	1.82E+14
7	31	2	0	1	1s2p6 2S1/2	433.1776	1.07E+12	1.10E+14

Table A.2: Radiative K-transition data nitrogen ions

N	j	i	Wavelength 0.1 nm	A-coefficient s^{-1}	gf-value
1	3	1	24.7814	1.51E+12	2.77E−01
1	4	1	24.7760	1.51E+12	5.55E−01
2	4	1	29.1209	8.13E+07	3.10E−05
2	7	1	28.8028	2.12E+12	7.93E−01
3	4	2	30.9798	4.08E+10	1.17E−02
3	4	3	30.9822	8.08E+10	2.33E−02
3	5	1	30.0183	5.05E+06	1.36E−06
3	6	1	30.0170	1.27E+07	6.87E−06
3	8	1	29.4586	1.65E+12	4.29E−01
3	9	1	29.4571	1.65E+12	8.61E−01
3	10	2	29.9203	9.70E+06	2.61E−06
3	10	3	29.9226	2.36E+05	6.34E−08
3	11	2	29.9191	7.01E+04	3.77E−08

Continued on Next Page...

Table A.2 – Continued

N	j	i	Wavelength 0.1 nm	A-coefficient s^{-1}	gf-value
3	11	3	29.9213	1.58E+07	8.49E−06
3	12	3	29.9192	2.14E+07	1.72E−05
3	13	1	29.1289	1.62E+11	4.12E−02
3	14	1	29.1279	1.54E+11	7.83E−02
3	15	2	29.5695	7.16E+11	3.76E−01
3	15	3	29.5717	1.17E+11	6.12E−02
3	16	3	29.5717	8.32E+11	6.55E−01
3	17	2	29.4935	1.79E+12	4.68E−01
3	17	3	29.4957	8.89E+11	2.32E−01
3	18	2	29.4910	4.24E+11	2.21E−01
3	18	3	29.4932	2.26E+12	1.18E+00
3	19	2	29.0197	2.56E+11	6.46E−02
3	19	3	29.0218	5.28E+11	1.33E−01
4	11	7	31.9393	5.72E+10	8.75E−03
4	12	1	30.2331	4.74E+07	1.95E−05
4	12	6	31.9374	1.91E+10	8.79E−03
4	12	7	31.9381	1.43E+10	6.58E−03
4	12	8	31.9395	2.38E+10	1.09E−02
4	12	9	32.1303	7.46E+05	3.46E−07
4	12	10	32.6487	8.61E+04	4.13E−08
4	13	7	31.9356	1.44E+10	1.10E−02
4	13	8	31.9370	4.30E+10	3.29E−02
4	13	9	32.1277	6.38E+05	4.94E−07
4	14	2	30.7417	1.38E+06	5.89E−07
4	14	3	30.7424	4.03E+06	1.71E−06
4	14	4	30.7437	3.48E+05	1.48E−07
4	14	5	31.4289	1.87E+00	8.30E−13
4	15	3	30.7412	9.78E+02	6.92E−10
4	15	4	30.7425	3.94E+06	2.79E−06
4	15	5	31.4276	1.57E−01	1.17E−13
4	16	4	30.7407	3.76E+06	3.72E−06
4	17	1	29.9571	1.55E+12	6.27E−01
4	17	6	31.6296	4.67E+05	2.10E−07
4	17	7	31.6304	7.76E+05	3.49E−07
4	17	8	31.6317	1.44E+06	6.50E−07
4	17	9	31.8188	1.11E+11	5.06E−02
4	17	10	32.3271	8.10E+09	3.81E−03
4	18	3	30.0966	2.30E+12	3.13E−01
4	18	5	30.7542	1.60E+05	2.28E−08
4	19	2	30.0951	7.84E+11	3.19E−01

Continued on Next Page...

Table A.2 – Continued

N	j	i	Wavelength 0.1 nm	A-coefficient s^{-1}	gf-value
4	19	3	30.0957	5.67E+11	2.31E−01
4	19	4	30.0970	9.51E+11	3.87E−01
4	19	5	30.7533	3.97E+05	1.69E−07
4	20	3	30.0940	5.96E+11	4.05E−01
4	20	4	30.0953	1.71E+12	1.16E+00
4	20	5	30.7515	8.79E+05	6.22E−07
4	21	2	30.0419	3.89E+11	1.58E−01
4	21	3	30.0426	3.13E+11	1.27E−01
4	21	4	30.0439	2.40E+10	9.73E−03
4	21	5	30.6979	2.75E+06	1.17E−06
4	22	4	30.0439	7.26E+11	6.87E−01
4	23	3	30.0426	5.24E+11	3.54E−01
4	23	4	30.0439	2.02E+11	1.37E−01
4	23	5	30.6978	1.09E+06	7.69E−07
4	24	2	29.7098	8.63E+10	3.43E−02
4	24	3	29.7104	2.61E+11	1.04E−01
4	24	4	29.7117	4.39E+11	1.75E−01
4	24	5	30.3511	1.11E+07	4.60E−06
4	25	7	30.6000	1.13E+06	7.94E−07
4	25	8	30.6013	3.32E+06	2.33E−06
4	25	9	30.7764	7.11E−01	5.05E−13
4	26	3	29.6105	4.48E+06	2.94E−06
4	26	4	29.6118	3.47E+07	2.28E−05
4	26	5	30.2469	7.43E+11	5.09E−01
4	27	3	29.5127	8.81E+10	1.15E−02
4	27	5	30.1448	7.89E+07	1.07E−05
4	28	2	29.5112	2.82E+10	1.11E−02
4	28	3	29.5119	2.11E+10	8.28E−03
4	28	4	29.5131	3.83E+10	1.50E−02
4	28	5	30.1439	5.23E+07	2.14E−05
4	29	3	29.5102	2.13E+10	1.39E−02
4	29	4	29.5115	6.55E+10	4.28E−02
4	29	5	30.1423	8.09E+07	5.51E−05
4	30	2	29.3267	2.58E+06	9.98E−07
4	30	3	29.3273	2.93E+06	1.13E−06
4	30	4	29.3285	3.14E+05	1.22E−07
4	30	5	29.9514	2.35E+12	9.46E−01
4	31	3	29.2882	8.67E+04	1.11E−08
4	31	5	29.9106	8.40E+11	1.13E−01
4	32	1	28.6495	2.25E+05	8.32E−08

Continued on Next Page...

Table A.2 – Continued

N	j	i	Wavelength 0.1 nm	A-coefficient s^{-1}	gf-value
4	32	6	30.1755	3.87E+11	1.58E−01
4	32	7	30.1761	2.86E+11	1.17E−01
4	32	8	30.1774	1.87E+10	7.66E−03
4	32	9	30.3476	6.96E+06	2.88E−06
4	32	10	30.8096	2.33E+06	9.93E−07
4	33	7	30.1761	5.22E+11	3.56E−01
4	33	8	30.1773	1.70E+11	1.16E−01
4	33	9	30.3476	4.96E+06	3.43E−06
4	34	8	30.1773	6.92E+11	6.61E−01
4	34	9	30.3476	1.89E+07	1.82E−05
4	35	1	28.5726	1.74E+05	6.37E−08
4	35	6	30.0901	3.50E+11	1.43E−01
4	35	7	30.0908	1.05E+12	4.27E−01
4	35	8	30.0920	1.73E+12	7.06E−01
4	35	9	30.2613	1.11E+07	4.58E−06
4	35	10	30.7207	3.07E+06	1.30E−06
4	36	7	29.9243	4.49E+07	3.01E−05
4	36	8	29.9255	3.93E+08	2.64E−04
4	36	9	30.0929	2.27E+12	1.54E+00
4	37	7	29.8361	6.81E+11	9.08E−02
4	38	1	28.3428	2.09E+04	7.55E−09
4	38	6	29.8354	2.22E+11	8.89E−02
4	38	7	29.8360	1.68E+11	6.73E−02
4	38	8	29.8372	2.91E+11	1.16E−01
4	38	9	30.0036	4.83E+06	1.95E−06
4	38	10	30.4552	3.05E+06	1.27E−06
4	39	7	29.8358	1.67E+11	1.11E−01
4	39	8	29.8370	5.13E+11	3.43E−01
4	39	9	30.0034	8.34E+08	5.62E−04
4	40	1	28.1186	3.04E+09	1.08E−03
4	40	6	29.5870	9.94E+05	3.92E−07
4	40	7	29.5877	2.46E+06	9.68E−07
4	40	8	29.5889	4.15E+05	1.63E−07
4	40	9	29.7525	1.23E+12	4.89E−01
4	40	10	30.1965	1.02E+12	4.19E−01
5	16	1	30.8842	1.32E+07	3.78E−06
5	16	2	30.8859	4.52E+06	1.29E−06
5	16	11	32.7521	1.93E+10	6.19E−03
5	16	12	33.0230	5.64E+04	1.85E−08
5	16	14	33.3371	5.07E+04	1.69E−08

Continued on Next Page...

Table A.2 – Continued

N	j	i	Wavelength 0.1 nm	A-coefficient s^{-1}	gf-value
5	16	15	33.3372	2.10E+05	7.00E−08
5	17	1	30.8832	2.64E+03	1.51E−09
5	17	2	30.8849	8.86E+06	5.07E−06
5	17	11	32.7510	1.93E+10	1.24E−02
5	17	12	33.0219	1.06E+05	6.92E−08
5	17	13	33.0219	7.63E+04	4.99E−08
5	17	14	33.3359	4.65E−01	3.10E−13
5	17	15	33.3361	1.83E+04	1.22E−08
5	18	2	30.8832	9.74E+06	8.36E−06
5	18	11	32.7491	1.93E+10	1.87E−02
5	18	12	33.0200	1.98E+04	1.94E−08
5	18	13	33.0200	2.79E+05	2.74E−07
5	18	15	33.3341	1.82E+04	1.82E−08
5	19	4	31.3448	7.24E+05	6.40E−07
5	19	5	31.3458	1.68E+06	1.48E−06
5	19	6	31.8696	4.13E−02	3.77E−14
5	19	7	31.8696	5.84E−01	5.33E−13
5	19	10	32.3716	6.89E−02	6.50E−14
5	20	1	30.5407	5.51E+11	3.08E−01
5	20	2	30.5423	7.44E+10	4.16E−02
5	20	11	32.3660	4.14E+04	2.61E−08
5	20	12	32.6305	2.81E+10	1.79E−02
5	20	13	32.6306	4.32E+09	2.76E−03
5	20	14	32.9372	5.56E+09	3.61E−03
5	20	15	32.9373	7.66E+08	4.99E−04
5	21	2	30.5422	6.24E+11	5.24E−01
5	21	11	32.3659	2.44E+05	2.30E−07
5	21	12	32.6305	2.20E+09	2.11E−03
5	21	13	32.6305	3.02E+10	2.90E−02
5	21	15	32.9372	6.24E+09	6.10E−03
5	22	1	30.5099	1.38E+12	3.86E−01
5	22	2	30.5115	6.72E+11	1.87E−01
5	22	11	32.3314	1.33E+03	4.16E−10
5	22	12	32.5954	6.46E+10	2.06E−02
5	22	14	32.9013	1.47E+10	4.78E−03
5	22	15	32.9014	7.63E+09	2.48E−03
5	23	1	30.5079	3.11E+11	1.74E−01
5	23	2	30.5095	1.74E+12	9.73E−01
5	23	11	32.3292	3.02E+03	1.89E−09
5	23	12	32.5931	7.43E+09	4.73E−03

Continued on Next Page...

Table A.2 – Continued

N	j	i	Wavelength 0.1 nm	A-coefficient s^{-1}	gf-value
5	23	13	32.5931	5.70E+10	3.63E−02
5	23	14	32.8990	3.42E+09	2.22E−03
5	23	15	32.8991	1.91E+10	1.24E−02
5	24	1	30.3662	2.39E+11	6.59E−02
5	24	2	30.3678	5.17E+11	1.43E−01
5	24	11	32.1701	6.24E+04	1.94E−08
5	24	12	32.4315	4.59E+06	1.45E−06
5	24	14	32.7343	1.32E+10	4.25E−03
5	24	15	32.7344	2.54E+10	8.17E−03
5	25	3	30.6416	4.49E+11	2.53E−01
5	25	4	30.6421	8.95E+11	5.04E−01
5	25	5	30.6430	1.34E+12	7.52E−01
5	25	6	31.1435	1.61E+04	9.40E−09
5	25	7	31.1435	1.45E+05	8.45E−08
5	25	8	31.4381	7.52E+05	4.46E−07
5	25	9	31.6215	1.49E+04	8.91E−09
5	25	10	31.6227	7.60E+04	4.56E−08
5	26	3	30.5711	2.48E+11	1.39E−01
5	26	4	30.5716	3.12E+11	1.75E−01
5	26	5	30.5725	2.82E+10	1.58E−02
5	26	6	31.0707	8.38E+05	4.85E−07
5	26	7	31.0707	1.96E+06	1.14E−06
5	26	8	31.3639	5.07E+05	2.99E−07
5	26	9	31.5465	8.11E+04	4.84E−08
5	26	10	31.5476	1.20E+04	7.16E−09
5	27	3	30.5711	4.92E+11	1.38E−01
5	27	4	30.5716	9.64E+10	2.70E−02
5	27	6	31.0707	5.22E+06	1.51E−06
5	27	8	31.3639	1.03E+06	3.04E−07
5	27	9	31.5465	6.09E+04	1.82E−08
5	27	10	31.5476	2.94E+04	8.79E−09
5	28	4	30.5716	4.16E+11	3.49E−01
5	28	5	30.5725	1.72E+11	1.45E−01
5	28	6	31.0707	1.56E+05	1.36E−07
5	28	7	31.0707	4.42E+05	3.84E−07
5	28	10	31.5476	6.95E+04	6.22E−08
5	29	5	30.5725	5.88E+11	6.59E−01
5	29	7	31.0707	1.38E+06	1.60E−06
5	30	3	30.3675	1.01E+11	2.80E−02
5	30	4	30.3680	5.16E+11	1.43E−01

Continued on Next Page...

Table A.2 – Continued

N	j	i	Wavelength 0.1 nm	A-coefficient s^{-1}	gf-value
5	30	6	30.8604	1.94E+05	5.55E−08
5	30	8	31.1496	2.63E+05	7.64E−08
5	30	9	31.3297	3.64E+05	1.07E−07
5	30	10	31.3309	4.52E+05	1.33E−07
5	31	3	30.3675	2.52E+11	1.39E−01
5	31	4	30.3680	8.26E+10	4.57E−02
5	31	5	30.3689	2.82E+11	1.56E−01
5	31	6	30.8604	4.72E+06	2.70E−06
5	31	7	30.8604	1.71E+01	9.77E−12
5	31	8	31.1496	6.78E+05	3.94E−07
5	31	9	31.3297	1.80E+02	1.06E−10
5	31	10	31.3309	3.02E+04	1.77E−08
5	32	4	30.3680	1.81E+11	1.50E−01
5	32	5	30.3689	4.36E+11	3.61E−01
5	32	6	30.8604	1.71E+06	1.46E−06
5	32	7	30.8604	2.38E+07	2.03E−05
5	32	10	31.3308	1.97E+04	1.74E−08
5	33	3	30.1090	8.12E+05	4.42E−07
5	33	4	30.1095	1.54E+05	8.38E−08
5	33	5	30.1104	5.39E+04	2.93E−08
5	33	6	30.5935	1.60E+12	8.97E−01
5	33	7	30.5935	1.81E+11	1.02E−01
5	33	8	30.8777	1.76E+07	1.01E−05
5	33	9	31.0547	5.16E+10	2.99E−02
5	33	10	31.0558	1.00E+10	5.81E−03
5	34	4	30.1095	2.70E+06	2.20E−06
5	34	5	30.1104	4.34E+05	3.54E−07
5	34	6	30.5935	1.19E+11	1.00E−01
5	34	7	30.5935	1.66E+12	1.40E+00
5	34	10	31.0558	6.10E+10	5.30E−02
5	35	3	29.9113	5.95E+03	1.60E−09
5	35	4	29.9118	4.84E+03	1.30E−09
5	35	6	30.3894	1.06E+12	2.93E−01
5	35	8	30.6699	7.62E+11	2.15E−01
5	35	9	30.8444	4.84E+10	1.38E−02
5	35	10	30.8455	2.47E+10	7.05E−03
5	36	3	29.9113	1.14E+06	6.12E−07
5	36	4	29.9118	2.02E+06	1.08E−06
5	36	5	29.9127	3.53E+06	1.90E−06
5	36	6	30.3894	1.11E+11	6.15E−02

Continued on Next Page...

Table A.2 – Continued

N	j	i	Wavelength 0.1 nm	A-coefficient s^{-1}	gf-value
5	36	7	30.3894	9.46E+11	5.24E−01
5	36	8	30.6699	7.65E+11	4.32E−01
5	36	9	30.8444	1.20E+10	6.82E−03
5	36	10	30.8455	5.90E+10	3.37E−02
5	37	3	29.7971	7.82E+09	4.17E−03
5	37	4	29.7976	1.58E+10	8.41E−03
5	37	5	29.7984	2.42E+10	1.29E−02
5	37	6	30.2715	1.77E+06	9.71E−07
5	37	7	30.2715	1.65E+07	9.08E−06
5	37	8	30.5497	1.44E+07	8.05E−06
5	37	9	30.7229	2.97E+06	1.68E−06
5	37	10	30.7240	1.44E+07	8.15E−06
5	38	4	29.7416	1.62E+05	1.29E−07
5	38	5	29.7425	3.59E+05	2.86E−07
5	38	6	30.2137	1.10E+10	8.99E−03
5	38	7	30.2137	1.57E+11	1.29E−01
5	38	10	30.6646	5.46E+11	4.61E−01
5	39	3	29.7411	3.44E+04	1.83E−08
5	39	4	29.7416	8.20E+03	4.35E−09
5	39	5	29.7425	4.44E+04	2.36E−08
5	39	6	30.2137	1.49E+11	8.17E−02
5	39	7	30.2137	1.91E+10	1.05E−02
5	39	8	30.4909	2.00E+07	1.11E−05
5	39	9	30.6635	4.54E+11	2.56E−01
5	39	10	30.6645	9.06E+10	5.11E−02
5	40	3	29.5467	1.51E+05	3.95E−08
5	40	4	29.5472	8.57E+03	2.24E−09
5	40	6	30.0131	8.38E+10	2.26E−02
5	40	8	30.2866	7.16E+10	1.97E−02
5	40	9	30.4569	7.84E+11	2.18E−01
5	40	10	30.4579	2.08E+07	5.79E−06
5	41	3	29.5463	3.43E+05	1.79E−07
5	41	4	29.5468	7.61E+04	3.98E−08
5	41	5	29.5476	2.62E+05	1.37E−07
5	41	6	30.0127	9.16E+09	4.95E−03
5	41	7	30.0127	8.46E+10	4.57E−02
5	41	8	30.2862	7.63E+10	4.20E−02
5	41	9	30.4564	9.68E+10	5.38E−02
5	41	10	30.4575	4.88E+11	2.72E−01
5	42	3	29.5424	1.94E+04	5.08E−09

Continued on Next Page...

Table A.2 – Continued

N	j	i	Wavelength 0.1 nm	A-coefficient s^{-1}	gf-value
5	42	4	29.5429	7.83E+00	2.05E−12
5	42	6	30.0087	9.34E+09	2.52E−03
5	42	8	30.2821	7.40E+09	2.04E−03
5	42	9	30.4523	4.87E+11	1.36E−01
5	42	10	30.4534	1.96E+12	5.45E−01
5	43	2	28.9238	4.14E+04	3.11E−08
5	43	11	30.5541	5.53E+11	4.65E−01
5	43	12	30.7898	1.09E+06	9.27E−07
5	43	13	30.7898	1.51E+07	1.29E−05
5	43	15	31.0628	7.09E+05	6.15E−07
5	44	1	28.9210	7.25E+00	3.64E−12
5	44	2	28.9225	4.43E+04	2.22E−08
5	44	11	30.5527	5.53E+11	3.10E−01
5	44	12	30.7883	5.44E+06	3.09E−06
5	44	13	30.7884	3.12E+06	1.77E−06
5	44	14	31.0612	1.08E+04	6.27E−09
5	44	15	31.0613	3.80E+05	2.20E−07
5	45	1	28.9203	1.20E+02	3.00E−11
5	45	2	28.9217	3.78E+04	9.48E−09
5	45	11	30.5518	5.54E+11	1.55E−01
5	45	12	30.7875	2.26E+06	6.41E−07
5	45	14	31.0603	6.88E+05	1.99E−07
5	45	15	31.0604	2.98E+06	8.61E−07
5	46	1	28.6636	1.61E+08	7.93E−05
5	46	2	28.6650	4.50E+07	2.22E−05
5	46	11	30.2655	7.34E+05	4.04E−07
5	46	12	30.4967	8.47E+11	4.72E−01
5	46	13	30.4968	7.65E+10	4.27E−02
5	46	14	30.7644	2.43E+11	1.38E−01
5	46	15	30.7645	5.79E+10	3.29E−02
5	47	2	28.6650	2.06E+08	1.52E−04
5	47	11	30.2655	4.49E+06	3.70E−06
5	47	12	30.4967	6.02E+10	5.05E−02
5	47	13	30.4967	8.60E+11	7.19E−01
5	47	15	30.7645	3.04E+11	2.58E−01
5	48	1	28.6177	1.92E+08	9.44E−05
5	48	2	28.6191	9.32E+08	4.58E−04
5	48	11	30.2144	2.39E+05	1.31E−07
5	48	12	30.4448	1.56E+11	8.67E−02
5	48	13	30.4448	1.54E+12	8.55E−01

Continued on Next Page...

Table A.2 – Continued

N	j	i	Wavelength 0.1 nm	A-coefficient s^{-1}	gf-value
5	48	14	30.7116	1.79E+11	1.01E−01
5	48	15	30.7117	8.38E+11	4.74E−01
5	49	1	28.6162	7.40E+08	1.82E−04
5	49	2	28.6176	3.65E+08	8.95E−05
5	49	11	30.2127	8.86E+04	2.43E−08
5	49	12	30.4431	1.68E+12	4.68E−01
5	49	14	30.7099	6.84E+11	1.94E−01
5	49	15	30.7099	3.43E+11	9.68E−02
5	50	1	28.2711	2.34E+07	5.62E−06
5	50	2	28.2725	2.07E+08	4.95E−05
5	50	11	29.8283	5.98E+04	1.60E−08
5	50	12	30.0529	1.80E+06	4.86E−07
5	50	14	30.3128	4.09E+11	1.13E−01
5	50	15	30.3129	8.31E+11	2.29E−01
6	21	2	31.3545	1.71E+06	1.26E−06
6	21	3	31.3554	5.06E+06	3.73E−06
6	21	4	31.5310	4.37E−01	3.25E−13
6	21	16	33.7286	3.45E+04	2.94E−08
6	21	17	33.7294	1.12E+04	9.57E−09
6	21	19	33.9501	4.19E+00	3.62E−12
6	22	2	30.9523	3.98E+11	2.86E−01
6	22	3	30.9532	1.23E+11	8.81E−02
6	22	4	31.1243	1.89E+06	1.37E−06
6	22	16	33.2637	2.10E+09	1.74E−03
6	22	17	33.2645	5.88E+09	4.88E−03
6	22	19	33.4791	7.63E+04	6.41E−08
6	23	1	30.9519	2.95E+11	1.27E−01
6	23	2	30.9523	2.12E+11	9.14E−02
6	23	3	30.9532	1.34E+10	5.75E−03
6	23	4	31.1243	2.39E+07	1.04E−05
6	23	5	31.2587	4.22E+06	1.85E−06
6	23	16	33.2637	2.46E+08	1.22E−04
6	23	17	33.2645	3.37E+09	1.67E−03
6	23	18	33.2648	4.36E+09	2.17E−03
6	23	19	33.4791	5.97E+05	3.01E−07
6	23	20	33.8293	9.92E+04	5.11E−08
6	24	3	30.9532	5.21E+11	5.24E−01
6	24	4	31.1243	6.75E+06	6.85E−06
6	24	16	33.2637	7.99E+09	9.27E−03
6	24	19	33.4791	2.48E+05	2.92E−07

Continued on Next Page...

Table A.2 – Continued

N	j	i	Wavelength 0.1 nm	A-coefficient s^{-1}	gf-value
6	25	1	30.9311	2.76E+11	1.19E−01
6	25	2	30.9315	8.20E+11	3.53E−01
6	25	3	30.9324	1.33E+12	5.74E−01
6	25	4	31.1033	8.82E+05	3.84E−07
6	25	5	31.2375	3.85E+06	1.69E−06
6	25	16	33.2397	2.56E+10	1.27E−02
6	25	17	33.2405	1.51E+10	7.50E−03
6	25	18	33.2408	4.96E+09	2.47E−03
6	25	19	33.4548	1.70E+06	8.55E−07
6	25	20	33.8045	8.46E+04	4.36E−08
6	26	2	30.8591	1.40E+11	1.00E−01
6	26	3	30.8599	4.50E+11	3.21E−01
6	26	4	31.0300	1.24E+08	8.99E−05
6	26	16	33.1561	6.20E+09	5.11E−03
6	26	17	33.1568	2.22E+09	1.83E−03
6	26	19	33.3701	6.06E+06	5.06E−06
6	27	1	30.8586	1.85E+11	7.93E−02
6	27	2	30.8590	1.42E+11	6.10E−02
6	27	3	30.8599	2.63E+11	1.13E−01
6	27	4	31.0300	3.70E+06	1.60E−06
6	27	5	31.1635	3.00E+06	1.31E−06
6	27	16	33.1560	3.23E+09	1.60E−03
6	27	17	33.1567	2.19E+09	1.08E−03
6	27	18	33.1571	2.99E+09	1.48E−03
6	27	19	33.3700	1.92E+05	9.64E−08
6	27	20	33.7179	1.35E+04	6.90E−09
6	28	2	30.8590	5.90E+11	8.41E−02
6	28	17	33.1567	8.40E+09	1.38E−03
6	29	2	30.7447	1.55E+07	1.10E−05
6	29	3	30.7456	4.45E+06	3.16E−06
6	29	4	30.9144	1.74E+12	1.24E+00
6	29	16	33.0241	5.93E+04	4.85E−08
6	29	17	33.0248	2.74E+05	2.24E−07
6	29	19	33.2364	3.99E+10	3.30E−02
6	30	1	30.6529	3.36E+06	1.42E−06
6	30	2	30.6534	4.55E+06	1.92E−06
6	30	3	30.6542	6.22E+06	2.63E−06
6	30	4	30.8220	1.10E+12	4.69E−01
6	30	5	30.9538	7.28E+11	3.13E−01
6	30	16	32.9187	1.59E+05	7.76E−08

Continued on Next Page...

Table A.2 – Continued

N	j	i	Wavelength 0.1 nm	A-coefficient s^{-1}	gf-value
6	30	17	32.9194	1.17E+05	5.70E−08
6	30	18	32.9198	2.19E+05	1.07E−07
6	30	19	33.1297	2.79E+10	1.38E−02
6	30	20	33.4726	9.02E+09	4.55E−03
6	31	6	30.9118	4.72E+11	4.73E−01
6	31	8	31.4660	3.08E+05	3.20E−07
6	31	9	31.4660	2.45E+06	2.55E−06
6	31	12	31.6324	2.44E+03	2.56E−09
6	31	13	32.0873	3.12E−01	3.37E−13
6	32	6	30.9106	4.72E+11	3.38E−01
6	32	7	31.4647	1.99E+05	1.48E−07
6	32	8	31.4647	1.37E+06	1.02E−06
6	32	9	31.4647	6.42E+05	4.76E−07
6	32	11	31.6311	3.28E+03	2.46E−09
6	32	12	31.6311	2.16E+04	1.62E−08
6	32	13	32.0860	1.10E−01	8.49E−14
6	32	14	32.1610	2.89E+04	2.24E−08
6	32	15	32.2857	5.73E−01	4.48E−13
6	33	6	30.9098	4.72E+11	2.03E−01
6	33	7	31.4639	4.84E+05	2.15E−07
6	33	8	31.4639	4.19E+05	1.87E−07
6	33	10	31.6303	1.51E+05	6.81E−08
6	33	11	31.6303	5.14E+05	2.31E−07
6	33	12	31.6303	1.18E+06	5.28E−07
6	33	13	32.0851	3.40E−02	1.57E−14
6	33	14	32.1601	1.61E+04	7.48E−09
6	33	15	32.2848	4.23E−02	1.98E−14
6	34	6	30.4022	1.04E+05	7.18E−08
6	34	7	30.9382	1.55E+10	1.11E−02
6	34	8	30.9382	2.26E+11	1.63E−01
6	34	9	30.9382	1.21E+12	8.71E−01
6	34	11	31.0990	1.99E+11	1.44E−01
6	34	12	31.0990	6.05E+11	4.39E−01
6	34	13	31.5386	1.89E+05	1.41E−07
6	34	14	31.6111	2.46E+10	1.85E−02
6	34	15	31.7315	5.75E+04	4.34E−08
6	35	6	30.4010	5.90E+04	2.45E−08
6	35	7	30.9369	3.70E+11	1.59E−01
6	35	8	30.9369	1.08E+12	4.65E−01
6	35	10	31.0977	2.68E+11	1.17E−01

Continued on Next Page...

Table A.2 – Continued

N	j	i	Wavelength 0.1 nm	A-coefficient s^{-1}	gf-value
6	35	11	31.0977	2.03E+11	8.83E−02
6	35	12	31.0977	3.41E+11	1.48E−01
6	35	13	31.5373	3.10E+04	1.39E−08
6	35	14	31.6098	2.48E+10	1.11E−02
6	35	15	31.7302	9.89E+05	4.48E−07
6	36	7	30.9363	1.44E+12	2.07E−01
6	36	11	31.0971	8.15E+11	1.18E−01
6	36	14	31.6091	2.48E+10	3.72E−03
6	36	15	31.7296	3.73E+04	5.64E−09
6	37	6	30.3107	1.34E+04	5.55E−09
6	37	7	30.8434	5.74E+11	2.45E−01
6	37	8	30.8434	1.98E+11	8.45E−02
6	37	10	31.0032	1.37E+11	5.93E−02
6	37	11	31.0032	9.80E+10	4.24E−02
6	37	12	31.0033	5.91E+09	2.56E−03
6	37	13	31.4401	2.00E+06	8.89E−07
6	37	14	31.5121	1.66E+06	7.41E−07
6	37	15	31.6318	8.13E+04	3.66E−08
6	38	6	30.3107	1.19E+05	8.20E−08
6	38	7	30.8434	1.14E+11	8.11E−02
6	38	8	30.8434	5.31E+11	3.78E−01
6	38	9	30.8434	1.25E+11	8.93E−02
6	38	11	31.0032	1.86E+11	1.34E−01
6	38	12	31.0032	5.63E+10	4.06E−02
6	38	13	31.4401	1.47E+05	1.09E−07
6	38	14	31.5121	2.91E+06	2.17E−06
6	38	15	31.6318	1.08E+05	8.13E−08
6	39	6	30.3107	4.66E+05	4.50E−07
6	39	8	30.8434	8.41E+10	8.39E−02
6	39	9	30.8434	6.84E+11	6.82E−01
6	39	12	31.0032	2.44E+11	2.47E−01
6	39	13	31.4401	5.20E+05	5.40E−07
6	40	6	30.0483	1.45E+05	5.89E−08
6	40	7	30.5717	9.43E+05	3.96E−07
6	40	8	30.5717	2.86E+06	1.20E−06
6	40	10	30.7288	1.18E+11	5.00E−02
6	40	11	30.7288	3.54E+11	1.50E−01
6	40	12	30.7288	5.92E+11	2.52E−01
6	40	13	31.1579	1.56E+06	6.82E−07
6	40	14	31.2286	8.23E+06	3.61E−06

Continued on Next Page...

Table A.2 – Continued

N	j	i	Wavelength 0.1 nm	A-coefficient s^{-1}	gf-value
6	40	15	31.3462	2.97E+06	1.32E−06
6	41	6	29.9428	3.52E+01	2.37E−11
6	41	7	30.4625	1.07E+04	7.41E−09
6	41	8	30.4625	2.51E+06	1.75E−06
6	41	9	30.4625	1.44E+07	1.00E−05
6	41	11	30.6184	5.22E+06	3.66E−06
6	41	12	30.6184	6.56E+06	4.61E−06
6	41	13	31.0444	8.32E+11	6.01E−01
6	41	14	31.1146	9.88E+07	7.18E−05
6	41	15	31.2313	2.04E+11	1.49E−01
6	42	6	29.7802	1.64E+05	1.09E−07
6	42	7	30.2943	3.31E+08	2.28E−04
6	42	8	30.2943	5.03E+09	3.46E−03
6	42	9	30.2943	2.87E+10	1.97E−02
6	42	11	30.4485	2.97E+09	2.06E−03
6	42	12	30.4485	8.84E+09	6.15E−03
6	42	13	30.8698	1.71E+07	1.22E−05
6	42	14	30.9392	3.64E+11	2.61E−01
6	42	15	31.0546	3.83E+07	2.77E−05
6	43	6	29.7796	9.12E+04	3.64E−08
6	43	7	30.2936	8.38E+09	3.46E−03
6	43	8	30.2936	2.54E+10	1.05E−02
6	43	10	30.4478	3.93E+09	1.64E−03
6	43	11	30.4478	2.83E+09	1.18E−03
6	43	12	30.4478	5.46E+09	2.28E−03
6	43	13	30.8691	7.40E+07	3.17E−05
6	43	14	30.9385	3.67E+11	1.58E−01
6	43	15	31.0538	3.73E+06	1.62E−06
6	44	7	30.2932	3.37E+10	4.63E−03
6	44	11	30.4474	1.24E+10	1.73E−03
6	44	14	30.9381	3.68E+11	5.28E−02
6	44	15	31.0535	1.65E+08	2.39E−05
6	45	7	30.2388	2.65E+06	3.63E−07
6	45	11	30.3925	2.03E+06	2.81E−07
6	45	14	30.8813	4.14E+07	5.93E−06
6	45	15	30.9963	7.59E+11	1.09E−01
6	46	6	29.6988	4.35E−04	1.73E−16
6	46	7	30.2100	1.37E+06	5.61E−07
6	46	8	30.2100	2.70E+06	1.11E−06
6	46	10	30.3634	9.44E+04	3.92E−08

Continued on Next Page...

Table A.2 – Continued

N	j	i	Wavelength 0.1 nm	A-coefficient s^{-1}	gf-value
6	46	11	30.3634	2.57E+05	1.06E−07
6	46	12	30.3634	1.84E+06	7.64E−07
6	46	13	30.7823	1.24E+12	5.28E−01
6	46	14	30.8513	4.42E+05	1.89E−07
6	46	15	30.9660	5.38E+11	2.32E−01
6	47	2	28.7952	8.08E+07	5.02E−05
6	47	3	28.7960	2.51E+08	1.56E−04
6	47	4	28.9440	2.22E+04	1.40E−08
6	47	16	30.7853	4.83E+11	3.44E−01
6	47	17	30.7860	1.60E+11	1.14E−01
6	47	19	30.9698	1.48E+06	1.07E−06
6	48	1	28.7936	1.16E+08	4.32E−05
6	48	2	28.7940	9.51E+07	3.55E−05
6	48	3	28.7948	1.19E+08	4.44E−05
6	48	4	28.9428	7.00E+04	2.64E−08
6	48	5	29.0590	1.20E+03	4.54E−10
6	48	16	30.7840	2.66E+11	1.13E−01
6	48	17	30.7846	1.63E+11	6.93E−02
6	48	18	30.7849	2.15E+11	9.14E−02
6	48	19	30.9684	5.61E+07	2.42E−05
6	48	20	31.2678	1.30E+06	5.73E−07
6	49	2	28.7934	3.27E+08	4.06E−05
6	49	17	30.7839	6.43E+11	9.14E−02
6	50	1	28.6062	7.87E+03	2.90E−09
6	50	2	28.6065	1.52E+03	5.60E−10
6	50	3	28.6073	5.79E+03	2.13E−09
6	50	4	28.7534	8.50E+08	3.16E−04
6	50	5	28.8681	8.33E+08	3.12E−04
6	50	16	30.5698	1.08E+07	4.55E−06
6	50	17	30.5704	1.77E+04	7.43E−09
6	50	18	30.5707	2.33E+04	9.79E−09
6	50	19	30.7516	1.78E+12	7.55E−01
6	50	20	31.0468	3.10E+11	1.34E−01
7	16	1	31.2231	4.65E+11	4.08E−01
7	16	2	31.4463	7.46E+05	6.64E−07
7	16	3	31.4463	1.03E+07	9.20E−06
7	16	4	31.5189	2.64E+04	2.36E−08
7	16	14	34.0674	7.34E+04	7.67E−08
7	17	1	31.2219	4.65E+11	2.72E−01
7	17	2	31.4451	4.22E+06	2.50E−06

Continued on Next Page...

Table A.2 – Continued

N	j	i	Wavelength 0.1 nm	A-coefficient s^{-1}	gf-value
7	17	3	31.4451	3.36E+06	1.99E−06
7	17	4	31.5176	4.56E+04	2.72E−08
7	17	5	31.5176	8.94E+02	5.32E−10
7	17	14	34.0660	9.32E+04	6.49E−08
7	17	15	34.0668	2.14E+02	1.49E−10
7	18	1	31.2212	4.65E+11	1.36E−01
7	18	2	31.4444	2.13E+06	6.31E−07
7	18	4	31.5169	6.08E+06	1.81E−06
7	18	5	31.5169	2.50E+06	7.46E−07
7	18	14	34.0651	2.19E+04	7.60E−09
7	18	15	34.0660	1.05E+05	3.65E−08
7	19	1	30.9627	1.49E+05	8.59E−08
7	19	2	31.1822	8.16E+11	4.75E−01
7	19	3	31.1822	3.00E+10	1.75E−02
7	19	4	31.2536	2.15E+11	1.26E−01
7	19	5	31.2536	6.83E+10	4.00E−02
7	19	14	33.7577	6.47E+09	4.43E−03
7	19	15	33.7585	1.94E+09	1.33E−03
7	20	1	30.9624	2.32E+06	2.00E−06
7	20	2	31.1818	4.73E+10	4.14E−02
7	20	3	31.1818	6.94E+11	6.07E−01
7	20	4	31.2532	2.20E+11	1.94E−01
7	20	14	33.7572	6.21E+09	6.37E−03
7	21	1	30.9601	4.89E+05	2.81E−07
7	21	2	31.1796	1.42E+09	8.30E−04
7	21	3	31.1796	1.28E+12	7.48E−01
7	21	4	31.2509	4.17E+11	2.44E−01
7	21	5	31.2509	2.35E+11	1.37E−01
7	21	14	33.7546	1.22E+10	8.36E−03
7	21	15	33.7554	6.87E+09	4.70E−03
7	22	1	30.9591	1.08E+05	3.10E−08
7	22	2	31.1785	1.36E+12	3.98E−01
7	22	4	31.2499	2.47E+11	7.24E−02
7	22	5	31.2499	4.92E+11	1.44E−01
7	22	14	33.7534	7.18E+09	2.45E−03
7	22	15	33.7542	1.42E+10	4.85E−03
7	23	1	30.8375	7.30E+05	2.08E−07
7	23	2	31.0552	2.55E+06	7.38E−07
7	23	4	31.1259	7.14E+11	2.07E−01
7	23	5	31.1259	3.45E+11	1.00E−01

Continued on Next Page...

Table A.2 – Continued

N	j	i	Wavelength 0.1 nm	A-coefficient s^{-1}	gf-value
7	23	14	33.6088	5.28E+09	1.79E−03
7	23	15	33.6097	2.85E+09	9.66E−04
7	24	6	31.1258	5.87E+11	5.12E−01
7	24	7	31.1263	2.52E+11	2.19E−01
7	24	9	31.5754	2.55E+04	2.29E−08
7	24	10	31.5754	3.55E+05	3.18E−07
7	24	12	31.9768	2.91E+04	2.68E−08
7	25	6	31.1246	3.78E+11	2.19E−01
7	25	7	31.1252	1.12E+11	6.50E−02
7	25	8	31.1255	3.50E+11	2.03E−01
7	25	9	31.5743	6.01E+05	3.59E−07
7	25	10	31.5743	2.34E+06	1.40E−06
7	25	11	31.7819	9.59E+04	5.81E−08
7	25	12	31.9756	5.46E+04	3.35E−08
7	25	13	31.9763	8.69E+02	5.32E−10
7	26	7	31.1245	7.00E+11	2.03E−01
7	26	8	31.1248	1.40E+11	4.06E−02
7	26	9	31.5736	1.15E+06	3.44E−07
7	26	11	31.7811	3.93E+04	1.19E−08
7	26	12	31.9749	3.80E+04	1.16E−08
7	26	13	31.9756	9.69E+04	2.97E−08
7	27	6	30.7203	1.21E+05	6.85E−08
7	27	7	30.7208	2.19E+05	1.24E−07
7	27	8	30.7212	1.60E+06	9.06E−07
7	27	9	31.1583	5.64E+10	3.29E−02
7	27	10	31.1583	5.09E+11	2.96E−01
7	27	11	31.3604	1.89E+11	1.12E−01
7	27	12	31.5491	3.49E+10	2.08E−02
7	27	13	31.5497	6.73E+09	4.02E−03
7	28	7	30.7206	2.26E+05	6.40E−08
7	28	8	30.7209	6.74E+05	1.91E−07
7	28	9	31.1580	5.78E+11	1.68E−01
7	28	11	31.3601	1.92E+11	5.66E−02
7	28	12	31.5488	1.42E+10	4.24E−03
7	28	13	31.5494	2.82E+10	8.41E−03
7	29	6	30.3550	5.50E+03	3.04E−09
7	29	7	30.3555	1.23E+05	6.79E−08
7	29	8	30.3558	1.56E+05	8.61E−08
7	29	9	30.7825	6.57E+09	3.73E−03
7	29	10	30.7825	6.03E+10	3.43E−02

Continued on Next Page...

Table A.2 – Continued

N	j	i	Wavelength 0.1 nm	A-coefficient s^{-1}	gf-value
7	29	11	30.9798	2.00E+10	1.15E−02
7	29	12	31.1639	7.62E+11	4.45E−01
7	29	13	31.1645	1.53E+11	8.89E−02
7	30	7	30.3549	3.26E+04	8.99E−09
7	30	8	30.3552	1.12E+04	3.09E−09
7	30	9	30.7819	6.52E+10	1.85E−02
7	30	11	30.9791	2.05E+10	5.90E−03
7	30	12	31.1632	3.05E+11	8.89E−02
7	30	13	31.1639	6.10E+11	1.78E−01
7	31	1	28.6220	2.39E+03	5.87E−10
7	31	2	28.8095	6.60E+04	1.64E−08
7	31	4	28.8704	7.54E+07	1.88E−05
7	31	5	28.8704	2.54E+07	6.35E−06
7	31	14	30.9942	7.17E+11	2.07E−01
7	31	15	30.9949	3.48E+11	1.00E−01

Bibliography

Arav, N., et al. 2007, ApJ, 658, 829

Asplund, M., Grevesse, N., & Sauval, A. J. 2005, in Astronomical Society of the Pacific Conference Series, Vol. 336, Cosmic Abundances as Records of Stellar Evolution and Nucleosynthesis, ed. T. G. Barnes, III & F. N. Bash, 25–+

Auer, L. H., & Mihalas, D. 1970, MNRAS, 149, 65

Badnell, N. R. 1986, J. Phys. B: At. Mol. Opt. Phys., 19, 3827

—. 1997, J. Phys. B: At. Mol. Opt. Phys., 30, 1

Ballantyne, D. R., Ross, R. R., & Fabian, A. C. 2001, MNRAS, 327, 10

Bambynek, W., Crasemann, B., Fink, R. W., Freund, H.-U., Mark, H., Swift, C. D., Price, R. E., & Rao, P. V. 1972, Reviews of Modern Physics, 44, 716

Bar-Shalom, A., Klapisch, M., & Oreg, J. 1988, Phys. Rev. A, 38, 1773

—. 2001, Journal of Quantitative Spectroscopy and Radiative Transfer, 71, 169

Basko, M. M. 1978, ApJ, 223, 268

Bautista, M. A., & Kallman, T. R. 2001, ApJS, 134, 139

Bautista, M. A., Mendoza, C., Kallman, T. R., & Palmeri, P. 2003, A&A, 403, 339

—. 2004, A&A, 418, 1171

Behar, E., Jacobs, V. L., Oreg, J., Bar-Shalom, A., & Haan, S. L. 2000, Phys. Rev. A, 62, 030501

—. 2004, Phys. Rev. A, 69, 022704

Behar, E., & Netzer, H. 2002, ApJ, 570, 165

Behar, E., Rasmussen, A. P., Blustin, A. J., Sako, M., Kahn, S. M., Kaastra, J. S., Branduardi-Raymont, G., & Steenbrugge, K. C. 2003, ApJ, 598, 232

Behar, E., Sako, M., & Kahn, S. M. 2001, ApJ, 563, 497

Beiersdorfer, P., López-Urrutia, J. R. C., Springer, P., Utter, S. B., & Wong, K. L. 1999, Review of Scientific Instruments, 70, 276

Berrington, K. A., Burke, P. G., Butler, K., Seaton, M. J., Storey, P. J., Taylor, K. T., & Yan, Y. 1987, J. Phys. B: At. Mol. Opt. Phys., 20, 6379

Berry, H. G., Brooks, R. L., Cheng, K. T., Hardis, J. E., & Ray, W. 1982, Phys. Scr, 25, 391

Bhattacharyya, S., & Strohmayer, T. E. 2007, ApJ, 664, L103

Blackman, E. G. 1999, MNRAS, 306, L25

Bombaci, I. 1996, A&A, 305, 871

Bowyer, C. S., Lampton, M., Mack, J., & de Mendonca, F. 1970, ApJ, 161, L1+

Breit, G. 1932, Physical Review, 39, 616

Brenneman, L. W., & Reynolds, C. S. 2006, ApJ, 652, 1028

Brinkman, A. C., Kaastra, J. S., van der Meer, R. L. J., Kinkhabwala, A., Behar, E., Kahn, S. M., Paerels, F. B. S., & Sako, M. 2002, A&A, 396, 761

Buff, J., & McCray, R. 1974, ApJ, 189, 147

Cackett, E. M., Altamirano, D., Patruno, A., Miller, J. M., Reynolds, M., Linares, M., & Wijnands, R. 2009, ApJ, 694, L21

Cackett, E. M., et al. 2008, ApJ, 674, 415

Chandrasekhar, S. 1931, ApJ, 74, 81

—. 1960, Radiative transfer (New York: Dover)

Chen, M. H. 1986, Atomic Data and Nuclear Data Tables, 34, 301

Chen, M. H., & Crasemann, B. 1987, Atomic Data and Nuclear Data Tables, 37, 419

—. 1988, Atomic Data and Nuclear Data Tables, 38, 381

Chen, M. H., Reed, K. J., McWilliams, D. M., Guo, D. S., Barlow, L., Lee, M., & Walker, V. 1997, Atomic Data and Nuclear Data Tables, 65, 289

Chung, K. T. 1990, Phys. Rev. A, 42, 645

Condon, E. U., & Shortley, G. H. 1951, The theory of Atomic Spectra (Cambridge University Press, London)

Cowan, R. D. 1981, The theory of atomic structure and spectra (Berkeley, CA: Univ. of California Press)

Cunto, W., Mendoza, C., Ochsenbein, F., & Zeippen, C. J. 1993, A&A, 275, L5+

Czerny, B., & Zycki, P. T. 1994, ApJ, 431, L5

Davis, B. F., & Chung, K. T. 1989, Phys. Rev. A, 39, 3942

Done, C., Mulchaey, J. S., Mushotzky, R. F., & Arnaud, K. A. 1992, ApJ, 395, 275

Dumont, A.-M., Czerny, B., Collin, S., & Zycki, P. T. 2002, A&A, 387, 63

Einstein, A. 1905a, Annalen der Physik, 322, 132

—. 1905b, Annalen der Physik, 322, 891

—. 1915, Sitzungsberichte der Königlich Preußischen Akademie der Wissenschaften (Berlin), Seite 844-847., 844

Eissner, W., Jones, M., & Nussbaumer, H. 1974, Computer Physics Communications, 8, 270

Elvis, M., Maccacaro, T., Wilson, A. S., Ward, M. J., Penston, M. V., Fosbury, R. A. E., & Perola, G. C. 1978, MNRAS, 183, 129

Fabian, A. C., Iwasawa, K., Reynolds, C. S., & Young, A. J. 2000, PASP, 112, 1145

Fabian, A. C., Rees, M. J., Stella, L., & White, N. E. 1989, MNRAS, 238, 729

Favata, F., Neiner, C., Testa, P., Hussain, G., & Sanz-Forcada, J. 2009, A&A, 495, 217

García, J., Mendoza, C., Bautista, M. A., Gorczyca, T. W., Kallman, T. R., & Palmeri, P. 2005, ApJS, 158, 68

Genzel, R., & Eckart, A. 1998, Academie des Science Paris Comptes Rendus Serie B Sciences Physiques, 326, 69

George, I. M., & Fabian, A. C. 1991, MNRAS, 249, 352

Ghez, A. M., et al. 2008, ApJ, 689, 1044

Ghosh, K. K., Soundararajaperumal, S., Kalai Selvi, M., & Sivarani, T. 1992, A&A, 255, 119

Giacconi, R., Gursky, H., Paolini, F. R., & Rossi, B. B. 1962, Physical Review Letters, 9, 439

Giacconi, R., Murray, S., Gursky, H., Kellogg, E., Schreier, E., Matilsky, T., Koch, D., & Tananbaum, H. 1974, ApJS, 27, 37

Gorczyca, T., & McLaughlin, B. 2005, APS Meeting Abstracts, D6037+

Gorczyca, T. W., & Badnell, N. R. 1996, J. Phys. B: At. Mol. Opt. Phys., 29, L283

Gorczyca, T. W., & McLaughlin, B. M. 2000, J. Phys. B: At. Mol. Opt. Phys., 33, L859

Gottwald, M., Parmar, A. N., Reynolds, A. P., White, N. E., Peacock, A., & Taylor, B. G. 1995, A&AS, 109, 9

Green, A. R., McHardy, I. M., & Lehto, H. J. 1993, MNRAS, 265, 664

Grevesse, N., Noels, A., & Sauval, A. J. 1996, in Astronomical Society of the Pacific Conference Series, Vol. 99, Cosmic Abundances, ed. S. S. Holt & G. Sonneborn, 117–+

Guainazzi, M., Matsuoka, M., Piro, L., Mihara, T., & Yamauchi, M. 1994, ApJ, 436, L35

Guilbert, P. W., & Rees, M. J. 1988, MNRAS, 233, 475

Halpern, J. P. 1984, ApJ, 281, 90

Hapke, B. 1981, J. Geophys. Res., 86, 3039

Hardis, J. E., Berry, H. G., Curtis, L. J., & Livingston, A. E. 1984, Phys. Scr, 30, 189

Hata, J., & Grant, I. P. 1983, J. Phys. B: At. Mol. Opt. Phys., 16, L125

Hiroi, T. 1994, Icarus, 109, 313

Holt, S. S., Mushotzky, R. F., Boldt, E. A., Serlemitsos, P. J., Becker, R. H., Szymkowiak, A. E., & White, N. E. 1980, ApJ, 241, L13

Hsu, J.-J., Chung, K. T., & Huang, K.-N. 1991, Phys. Rev. A, 44, 5485

Hummer, D. G., Berrington, K. A., Eissner, W., Pradhan, A. K., Saraph, H. E., & Tully, J. A. 1993, A&A, 279, 298

Illarionov, A., Kallman, T., McCray, R., & Ross, R. 1979, ApJ, 228, 279

Iwasawa, K., Fabian, A. C., Young, A. J., Inoue, H., & Matsumoto, C. 1999, MNRAS, 306, L19

Iwasawa, K., & Taniguchi, Y. 1993, ApJ, 413, L15

Kaastra, J. S., de Vries, C. P., Costantini, E., & den Herder, J. W. A. 2009, A&A, 497, 291

Kaastra, J. S., & Mewe, R. 1993, A&AS, 97, 443

Kallman, T., & Bautista, M. 2001, ApJS, 133, 221

Kallman, T. R., Palmeri, P., Bautista, M. A., Mendoza, C., & Krolik, J. H. 2004, ApJS, 155, 675

Kaplan, S. A. 1949, Zhurnal Eksperimental noi i Teoreticheskoi Fiziki, 19, 951

Klapisch, M., & Busquet, M. 2009, High Ener. Dens. Phys., 5, 105

Klapisch, M., Schwob, J. L., Fraenkel, B. S., & Oreg, J. 1977, Journal of the Optical Society of America (1917-1983), 67, 148

Kompaneets, A. S. 1957, Sov. Phys.-JETP, 4, 730

Kormendy, J., & Richstone, D. 1995, ARA&A, 33, 581

Krolik, J. H., Madau, P., & Zycki, P. T. 1994, ApJ, 420, L57

Krolik, J. H., McKee, C. F., & Tarter, C. B. 1981, ApJ, 249, 422

Landi, E., & Phillips, K. J. H. 2006, ApJS, 166, 421

Laor, A. 1991, ApJ, 376, 90

Leighly, K. M., Pounds, K. A., & Turner, T. J. 1989, in ESA Special Publication, Vol. 296, Two Topics in X-Ray Astronomy, Volume 1: X Ray Binaries. Volume 2: AGN and the X Ray Background, ed. J. Hunt & B. Battrick, 961–967

Leutenegger, M. A., Kahn, S. M., & Ramsay, G. 2003, ApJ, 585, 1015

Lightman, A. P., Lamb, D. Q., & Rybicki, G. B. 1981, ApJ, 248, 738

Lightman, A. P., & Rybicki, G. B. 1980, ApJ, 236, 928

Lightman, A. P., & White, T. R. 1988, ApJ, 335, 57

Lin, H., Hsue, C.-S., & Chung, K. T. 2002, Phys. Rev. A, 65, 032706

Lin, S.-H., Hsue, C.-S., & Chung, K. T. 2001, Phys. Rev. A, 64, 012709

Lynden-Bell, D. 1969, Nature, 223, 690

Magdziarz, P., & Zdziarski, A. A. 1995, MNRAS, 273, 837

Markowitz, A., et al. 2007, ApJ, 665, 209

Matsuoka, M., Piro, L., Yamauchi, M., & Murakami, T. 1990, ApJ, 361, 440

Matt, G., Fabian, A. C., & Ross, R. R. 1993, MNRAS, 262, 179

—. 1996, MNRAS, 278, 1111

Matt, G., Perola, G. C., & Piro, L. 1991, A&A, 247, 25

McClintock, J. E., & Remillard, R. A. 2006, Black hole binaries (Cambridge University Press, London), 157–213

Mendoza, C., Kallman, T. R., Bautista, M. A., & Palmeri, P. 2004, A&A, 414, 377

Mihalas, D. 1978, Stellar atmospheres (2nd ed.; San Francisco, CA: Freeman)

Mihara, T., Matsuoka, M., Mushotzky, R. F., Kunieda, H., Otani, C., Miyamoto, S., & Yamauchi, M. 1994, PASJ, 46, L137

Miyata, E., Masai, K., & Hughes, J. P. 2008, PASJ, 60, 521

Miyoshi, S., Hayakawa, S., Kunieda, H., Nagase, F., & Tawara, Y. 1986, Ap&SS, 119, 185

Mushotzky, R. F. 1976, PhD thesis, California Univ., San Diego.

—. 1984, Advances in Space Research, 3, 157

Mushotzky, R. F., Holt, S. S., & Serlemitsos, P. J. 1978, ApJ, 225, L115

Nandra, K., George, I. M., Mushotzky, R. F., Turner, T. J., & Yaqoob, T. 1997, ApJ, 477, 602

Nandra, K., & Pounds, K. A. 1992, Nature, 359, 215

—. 1994, MNRAS, 268, 405

Nandra, K., et al. 1993, MNRAS, 260, 504

Nayakshin, S., & Kallman, T. R. 2001, ApJ, 546, 406

Nayakshin, S., Kazanas, D., & Kallman, T. R. 2000, ApJ, 537, 833

Ness, J.-U., et al. 2003, ApJ, 594, L127

Noble, S. C., Krolik, J. H., & Hawley, J. F. 2010, ApJ, 711, 959

Novikov, I. D., & Thorne, K. S. 1973, Black holes (Black holes, by C. DeWitt and B.S. DeWitt. New York: Gordon and Breach, 1973.)

Oreg, J., Goldstein, W. H., Klapisch, M., & Bar-Shalom, A. 1991, Phys. Rev. A, 44, 1750

Page, K. L., O'Brien, P. T., Reeves, J. N., & Turner, M. J. L. 2004, MNRAS, 347, 316

Palmeri, P., Mendoza, C., Kallman, T. R., & Bautista, M. A. 2002, ApJ, 577, L119

—. 2003a, A&A, 403, 1175

Palmeri, P., Mendoza, C., Kallman, T. R., Bautista, M. A., & Meléndez, M. 2003b, A&A, 410, 359

Palmeri, P., Quinet, P., Mendoza, C., Bautista, M. A., García, J., & Kallman, T. R. 2008a, ApJS, 177, 408

Palmeri, P., Quinet, P., Mendoza, C., Bautista, M. A., García, J., Witthoeft, M. C., & Kallman, T. R. 2008b, ApJS, 179, 542

Pounds, K. A., Nandra, K., Fink, H. H., & Makino, F. 1994, MNRAS, 267, 193

Pounds, K. A., Nandra, K., Stewart, G. C., George, I. M., & Fabian, A. C. 1990, Nature, 344, 132

Pounds, K. A., Nandra, K., Stewart, G. C., & Leighly, K. 1989, MNRAS, 240, 769

Poutanen, J., Nagendra, K. N., & Svensson, R. 1996, MNRAS, 283, 892

Pozdniakov, L. A., Sobol, I. M., & Sunyaev, R. A. 1979, A&A, 75, 214

Pradhan, A. K. 2000, ApJ, 545, L165

Ptak, A., Yaqoob, T., Serlemitsos, P. J., Mushotzky, R., & Otani, C. 1994, ApJ, 436, L31

Ralchenko, Y., Kramida, A. E., Reader, J., & NIST ADS Team. 2008, NIST Atomic Spectra Database, version 3.1.5 (Gaithersburg: NIST), http://physics.nist.gov/asd3

Ramírez, J. M., Komossa, S., Burwitz, V., & Mathur, S. 2008, ApJ, 681, 965

Reeves, J. N., et al. 2007, PASJ, 59, 301

Reilman, R. F., & Manson, S. T. 1979, ApJS, 40, 815

Reis, R. C., Fabian, A. C., & Young, A. J. 2009, MNRAS, 399, L1

Robicheaux, F., Gorczyca, T. W., Pindzola, M. S., & Badnell, N. R. 1995, Phys. Rev. A, 52, 1319

Ross, R. R., & Fabian, A. C. 1993, MNRAS, 261, 74

—. 2005, MNRAS, 358, 211

—. 2007, MNRAS, 381, 1697

Ross, R. R., Fabian, A. C., & Brandt, W. N. 1996, MNRAS, 278, 1082

Ross, R. R., Weaver, R., & McCray, R. 1978, ApJ, 219, 292

Rozanska, A., & Czerny, B. 1996, Acta Astron., 46, 233

Rutten, R. J. 2003, in Astronomical Society of the Pacific Conference Series, Vol. 288, Stellar Atmosphere Modeling, ed. I. Hubeny, D. Mihalas, & K. Werner, 99–+

Rybicki, G. B., & Lightman, A. P. 1979, Radiative processes in astrophysics (New York, Wiley-Interscience, 1979. 393 p.)

Sako, M., et al. 2001, A&A, 365, L168

Salpeter, E. E. 1964, ApJ, 140, 796

Scott, N. S., & Burke, P. G. 1980, J. Phys. B: At. Mol. Opt. Phys., 13, 4299

Scott, N. S., & Taylor, K. T. 1982, Computer Physics Communications, 25, 347

Seaton, M. 1987, J. Phys. B: At. Mol. Opt. Phys., 20, 6363

Shakura, N. I., & Sunyaev, R. A. 1973, A&A, 24, 337

Shapiro, S. L., Lightman, A. P., & Eardley, D. M. 1976, ApJ, 204, 187

Shapiro, S. L., & Teukolsky, S. A. 1986, Black Holes, White Dwarfs and Neutron Stars: The Physics of Compact Objects (Wiley-VCH, 1986, pp. 672)

Shiu, W. C., Hsue, C.-S., & Chung, K. T. 2001, Phys. Rev. A, 64, 022714

Steenbrugge, K. C., et al. 2005, A&A, 434, 569

Summers, H. P. 2004, The ADAS User Manual, version 2.6, http://adas.phys.strath.ac.uk

Tanaka, Y., Inoue, H., & Holt, S. S. 1994, PASJ, 46, L37

Tanaka, Y., et al. 1995, Nature, 375, 659

Tarter, C. B., Tucker, W. H., & Salpeter, E. E. 1969, ApJ, 156, 943

Thorne, K. S. 1994, Black holes and time warps: Einstein's outrageous legacy, ed. Thorne, K. S.

Tucker, W., Kellogg, E., Gursky, H., Giacconi, R., & Tananbaun, H. 1973, ApJ, 180, 715

Turner, T. J., George, I. M., & Mushotzky, R. F. 1993a, ApJ, 412, 72

Turner, T. J., Nandra, K., George, I. M., Fabian, A. C., & Pounds, K. A. 1993b, ApJ, 419, 127

Turner, T. J., & Pounds, K. A. 1989, MNRAS, 240, 833

Verner, D. A., & Yakovlev, D. G. 1995, A&AS, 109, 125

Wang, F., & Gou, B. 2006, Atomic Data and Nuclear Data Tables, 92, 176

Watanabe, S., et al. 2003, ApJ, 597, L37

Weaver, K. A., et al. 1994, ApJ, 423, 621

Wilkes, B. J., & Elvis, M. 1987, ApJ, 323, 243

Witthoeft, M. C., Bautista, M. A., Mendoza, C., Kallman, T. R., Palmeri, P., & Quinet, P. 2009, ApJS, 182, 127

Yang, H. Y., & Chung, K. T. 1995, Phys. Rev. A, 51, 3621

Yao, Y., Schulz, N. S., Gu, M. F., Nowak, M. A., & Canizares, C. R. 2009, ApJ, 696, 1418

Yaqoob, T., Serlemitsos, P., Mushotzky, R., Madejski, G., Turner, T. J., & Kunieda, H. 1994, PASJ, 46, L173

Yaqoob, T., et al. 2007, PASJ, 59, 283

Zhang, M., Cong Gou, B., & Cui, L. L. 2005, J. Phys. B: At. Mol. Opt. Phys., 38, 3567

Zycki, P. T., Krolik, J. H., Zdziarski, A. A., & Kallman, T. R. 1994, ApJ, 437, 597